EVALUATION OF COATING TO IMPROVE THE 0XIDATION BEHAVIOR OF METALLIC INTERCONNECTORS OF HIGH TEMPERATURE SOLID OXIDE ELECTROLYZERS IN HUMIDIFIED ATMOSPHERE

NANTICHA YAOWAMAN

A THESIS SUBMITTED IN PARTIAL FULFILLMENT
OF THE REQUIREMENT FOR THE DEGREE OF
MASTER OF ENGINEERING IN CHEMICAL ENGINEERING
FACULTY OF ENGINEERING
KING MONGKUT'S INSTITUTE OF TECHNOLOGY LADKRABANG
2012
KMITL-2012-EN-M-220-036

หัวข้อวิทยานิพนธ์	การประเมินพฤติกรรมด้านการเกิดออกซิเดชันของโลหะที่มีการเคลือบผิวเพื่อประยุกต์ใช้กับแผ่นกั้นเซลล์ในเซลล์อิเล็กโทรไลต์ชนิดออกไซด์แข็งในสภาวะที่มีความร้อนสูงและมีไอน้ำร่วม
นักศึกษา	นางสาว นันทิชา เยาวมาลย์
รหัสประจำตัว	53611610
ปริญญา	วิศวกรรมศาสตรมหาบัณฑิต
สาขาวิชา	วิศวกรรมเคมี
พ.ศ.	2555
อาจารย์ที่ปรึกษาวิทยานิพนธ์	ดร.วลัยรัตน์ จันทรอัมพร
อาจารย์ที่ปรึกษาวิทยานิพนธ์ร่วม	ผศ.ดร.สมฤกษ์ จันทรอัมพร

บทคัดย่อ

เนื่องจากการปฏิบัติงานของเครื่องแยกน้ำด้วยไฟฟ้า (electrolyzers) ชนิดออกไซด์แข็งเกิดขึ้นที่อุณหภูมิสูง จึงอาจส่งผลให้แผ่นกั้นเซลล์ประเภทโลหะเกิดการออกซิไดซ์ ด้วยคำนึงถึงผลดังกล่าว แผ่นกั้นเซลล์จึงถูกออกแบบมาเพื่อให้ทนต่อการเกิดออกซิเดชันในสภาวะการใช้งานจริง ในงานวิจัยนี้จึงได้ศึกษาการเกิดออกซิเดชันของโลหะ FeCoNi ที่มีการเคลือบผิวด้วยสารเคลือบที่มีโครงสร้าง spinel หรือ perovskite ด้วยเทคนิคการเคลือบผิวแบบ slurry application (SA method) หรือ physical vapor deposition (PVD method) ในสภาวะของขั้วแอโนด โดยศึกษาสภาวะจำลองที่อุณหภูมิ 800 $^{\circ}$C ในบรรยากาศของออกซิเจนที่มีความชื้น 5% ที่อัตราการไหล 10 L/h ผลการศึกษาพบว่า จลนพลศาสตร์การเกิดออกซิเดชันของชิ้นงานมีลักษณะเป็นพาราโบลิคกับเวลา ออกซิเดชันของโลหะ FeCoNi ทำให้เกิดออกไซด์ของ $CoFe_2O_4$ Fe_2O_3 และ $NiFe_2O_4$ ปกคลุมผิว ทั้งยังพบว่า การเคลือบผิวชิ้นงานด้วยวิธี SA สามารถลดการเกิดออกซิเดชันภายในได้ดีกว่าการเคลือบผิวชิ้นงานด้วยวิธี PVD อย่างไรก็ตามสำหรับชิ้นงานเคลือบยังพบชั้นเคลือบปะปนอยู่ในชั้นของออกไซด์ แสดงว่าออกซิเจนสามารถแพร่ผ่านชั้นเคลือบมายังโลหะได้ ดังนั้น การเคลือบผิวชิ้นงานในการทดลองนี้สามารถลดอัตราการเกิดออกซิเดชันของโลหะ FeCoNi ได้ แต่ไม่สามารถป้องกันการเกิดออกซิเดชันในสภาวะอุณหภูมิสูงและมีความชื้นได้

Thesis	Evaluation of coating to improve the oxidation behavior of metallic interconnectors of high temperature solid oxide electrolyzers in humidified atmosphere.
Student	Miss Nanticha Yaowaman
Student ID.	53611610
Degree	Master of Engineering
Program	Chemical Engineering
Year	2012
Thesis Advisor	Dr. Walairat Chandra-ambhorn
Thesis Co-advisor	Asst. Prof. Somrerk Chandra-ambhorn

ABSTRACT

Solid oxide electrolytic cells are operated at high temperatures under humidified atmosphere which lead to oxidation of interconnector part. To avoid this problem, interconnectors have to be first improved in way of lowering the oxidation in the operating atmosphere. In this study perovskite coatings and spinel coatings by physical vapor deposition (PVD method) or slurry application (SA method) were used to protect the oxidation of FeCoNi alloy in anodic atmosphere of SOEC. The samples were oxidized at 800 $^{\circ}C$ in O_2-5%H_2O at a total flow rate of 10 L/h. The results showed that the oxidation kinetics of samples was as a parabolic function of time. The oxidation of FeCoNi alloy led to three scale layers formed as $CoFe_2O_4$ layer, Fe_3O_4 layer, and $NiFe_2O_4$ layer, respectively. The coating by SA method seemed to provide better reducing internal oxidation of FeCoNi alloy than the coating by PVD method. However, there was presence of trace of coating in the scale layer which means that oxygen can diffuse through the coatings. Therefore, the coatings were able to reduce the oxidation rate of alloy but not able to protect FeCoNi alloy from oxidation at high temperature under humidified atmosphere.

Acknowledgements

This thesis could not be completed without the constructive advice and full support of many persons whom I would like to express my appreciation.

I would like to take this opportunity to express my deepest gratitude to Dr. Walairat Chandra-ambhorn and Asst.Prof. Somrerk Chandra-ambhorn. My research would not have been possible without their helpfulness.

I wish to express my deep thankfulness Prof. Alain Galerie, Prof. Yves Wouster and other workers, special for Valerie Parry, at the SIMaP Laboratory, Grenoble Institute of Technology, Grenoble, France. It is a pleasure to collaborate with them.

I would like to express thank to ArcelorMittal IMPHY for supporting the samples.

I am extremely grateful to Franco-Thai scholarship (PHC n° 2057XB). This work would not have been possible without their financial support.

I gratefully thank Anusara Srisrual and other people at Grenoble, France for their kindness during my stay in Grenoble. My time was enjoyable when they became a part of my life. I am grateful for spending time with them.

I am very grateful to school of chemical engineering, department of engineering, King's Mongkut Institute of Technology Ladkrabang, Bangkok, Thailand.

I would like to thank my friends at KMIT'L, special for friends who research at the same laboratory, for the wonderful friendship they offered me.

Furthermore, I also give special thanks to my family for always giving me greatest love, understanding and encouragement.

Finally, I would like to thank everybody who was important to the successful realization of thesis, as well as expressing my apology that I could not mention personally one by one.

Nanticha Yaowaman

Table of Contents

Table of Contents (cont.)

List of Tables

Tables **Page**

List of Figures

Figures Page

List of Figures (cont.)

Figures Page

List of Figures (cont.)

Figures **Page**

List of Figures (cont.)

Figure **Page**

List of Figures (cont.)

Figure **Page**

List of Figures (cont.)

Figure **Page**

Chapter1
Introduction

1.1 Statement and significance of the problems

In recent years, there have been increasing interests in hydrogen energy to use as an alternative energy. Hydrogen is used in variety applications such as fuel for vehicles, heating and producing the electricity. It is also used as a raw material for many chemical processes such as ammonia and methanol synthesis. It is well known that hydrogen is green energy carrier since the combustion reaction of hydrogen does not pollute the environment. Nowadays, hydrogen is produced by two main production technologies. The first one is thermal processes from fossil source and the other is electrolytic processes from renewable sources and nuclear. Primary process for producing hydrogen is steam methane reforming. The perspective for long term, fossil fuel conversion processes are not sustainable since they consume nonrenewable resources. Moreover, the reaction would emit greenhouse gases to the environment. Hence, hydrogen production by electrolytic processes from renewable sources using high temperature nuclear process heat is an alternative way which is interesting [1-2]. Recently, there are interests in producing hydrogen from water splitting via electrolytic process using an electrolyser [3-5]. Solid oxide electrolytic cell (SOEC) is a high temperature electrolytic device used to convert electricity and steam into hydrogen using unused heat from nuclear plants or waste heat from industrial processes [5]. One of advantages of hydrogen production by electrolytic cell is sustainability since water, raw material, is renewable source. Moreover the operation releases no green house gases [3,6]. However, one important disadvantage of application is that SOECs have to operate at high temperatures (700–1,000 $^{\circ}$C), alloy components, such as interconnectors, can be oxidized and lead to shorter lifetime (expected time is 40,000 h) [2]. Recently, traditional interconnect has been made from ceramic which is operated at 1000 $^{\circ}$C [2]. At lower operating temperatures (e.g., 650-850 $^{\circ}$C), metals can be used as interconnect instead of ceramic [7]. Metals are more flexible and inexpensive comparing with ceramic. Moreover, thermal conductivity and electrical conductivity of metal are greater than those of ceramic. Nevertheless, the first criterion for evaluating the material applying

as interconnect is the resistance to high temperature oxidation [7-8]. The candidates also have to remain high electrical conductivity and low area specific resistance (ASR). Generally the accepted maximum of ASR for interconnector is 0.1 Ω cm^2 [2, 7]. Moreover, to avoid the damage of cell components due to thermal cycles, the coefficient of thermal expansion (CTE) of the interconnect must close to that of electrolyte (i.e., ~10×10^{-6} $^{\circ}C^{-1}$ from 25 to 1,000 ℃) [7]. Stainless steel is widely applied for using as interconnector. The superalloys and austenitic stainless steels are not suitable due to their high CTE (i.e., 15-18 $\times10^{-6}$ $^{\circ}C^{-1}$ from 25 to 1,000 $^{\circ}C$) [7]. Ferritic stainless steels are the candidate due to their comparable CTEs with electrolyte, high electrical conductivity and low cost. Nonetheless, the problem of using ferritic stainless steels is that there is chromium evaporation from chromia passive film. At SOEC operating condition, chromia would react with oxygen molecules under dry atmosphere or with oxygen and water vapor under wet atmosphere and form volatile chromium species [8-11]. The volatile Cr would dissociate and deposit on the interface between electrode and electrolyte. The Cr deposite would poison the electrode and decrease the cell performance [8]. In order to solve this problem, coating, surface treatment and bulk composition modification and development have been considered.

Currently, the most promising material expected to use as interconnects is Crofer22 APU ferritic stainless steel. However this alloy also has chromium evaporation problem. Considering in CTE, interconnects have to well match with other cell components. Fe–Co–Ni base alloys is a low thermal expansion coefficient alloy that has been developed for using in clearance control area and as metal-glass seal for aircraft gas turbine engines. With its special property, FeCoNi alloy can probably be used as an interconnector in SOEC. Unfortunately, the low CTE Fe–Co–Ni alloys generally exhibit poor oxidation resistance at temperatures higher than 600 °C [2]. For improving the oxidation property, coating on alloys is also performed.

The objective of this research is to evaluate the coatings on FeCoNi alloy in high temperature electrolysis condition for applying as an interconnector in SOEC. In this research, the behaviors of uncoated and coated samples in the oxidation at high temperature electrolysis were investigated. Moreover the hardness of the coatings was also studied.

1.2. Objective

The objective of this project is to study the oxidation behavior of uncoated and coated FeCoNi alloys in high temperature electrolysis condition. Moreover the hardness of coating was also investigated.

1.3 Scope of the study

1. Metallic material in this work is FeCoNi alloy which was developed by ArcelorMittal IMPHY. The samples consist of uncoated and five coated samples:

- $La_{0.8}Sr_{0.2}MnO_3$ coated by slurry application method
- $La(Ni_{0.6}Fe_{0.4})O_3$ coated by slurry application method
- $La(Ni_{0.6}Fe_{0.4})O_3$ coated by physical vapor deposition method
- Co_3O_4 coated by physical vapor deposition method
- $MnCo_2O_4$ coated by physical vapor deposition method.

2. The experiment in this work was carried out at 800 $^{\circ}C$ in O_2-5%H_2O at a total flow rate of 10 L/h using thermobalance or horizontal furnace.

3. To analyze the samples, X-ray diffractrometer (XRD) was used to identify atomic structure of the scale occurring on the sample surface, scanning electron microscope and energy dispersive spectrometer (SEM/EDS) were used to analyze the chemical distribution.

4. The hardness of the coatings was measured by Vickers hardness method.

1.4 Research methodology

1. Identify the significant problems, objectives, scopes, and limitations of the study.
2. Study the theoretical background and literature review.

Design of the experiments.

3. Test the oxidation of the samples for studying the kinetics oxidation.
4. Test the oxidation of the samples for studying the morphology by XRD and SEM/EDS.
5. Test the hardness of the coatings by Vickers hardness method.
6. Conclude the results and write a report.

1.5 Outcomes of the thesis

This work attempts to evaluate the coated FeCoNi alloys for applying to use as an interconnector in solid oxide electrolytic cell.

1.6 Limitation of the study

This work is one part of the ICARE project which was performed in SIMaP group, Grenoble-INP, France. The experiment was carried out at SIMaP laboratory, Grenoble-INP, France for 5 months. The experimental time was limited because the researcher had to complete the experiment in 5 months. Furthermore the samples were not allowed to take back to Thailand, therefore some data were unable to reanalyze. The other limitation of this research is that APERAM (ex-ArcelorMittal Stainless) does not authorize any publishing of the composition of alloy.

Chapter 2

Theory and Literature Reviews

2.1 Theory

2.1.1 Solid oxide electrolytic cell

Recently, there have been increasing amount of literature on solid oxide electrolytic cell (SOEC). SOEC is a high temperature electrolytic device used to produce hydrogen via water splitting. SOEC has great potential for hydrogen production without any greenhouse gas emissions [6]. The cell consists of three different main parts i.e. electrolyte, electrodes and interconnector, as shows in Fig.2.1.

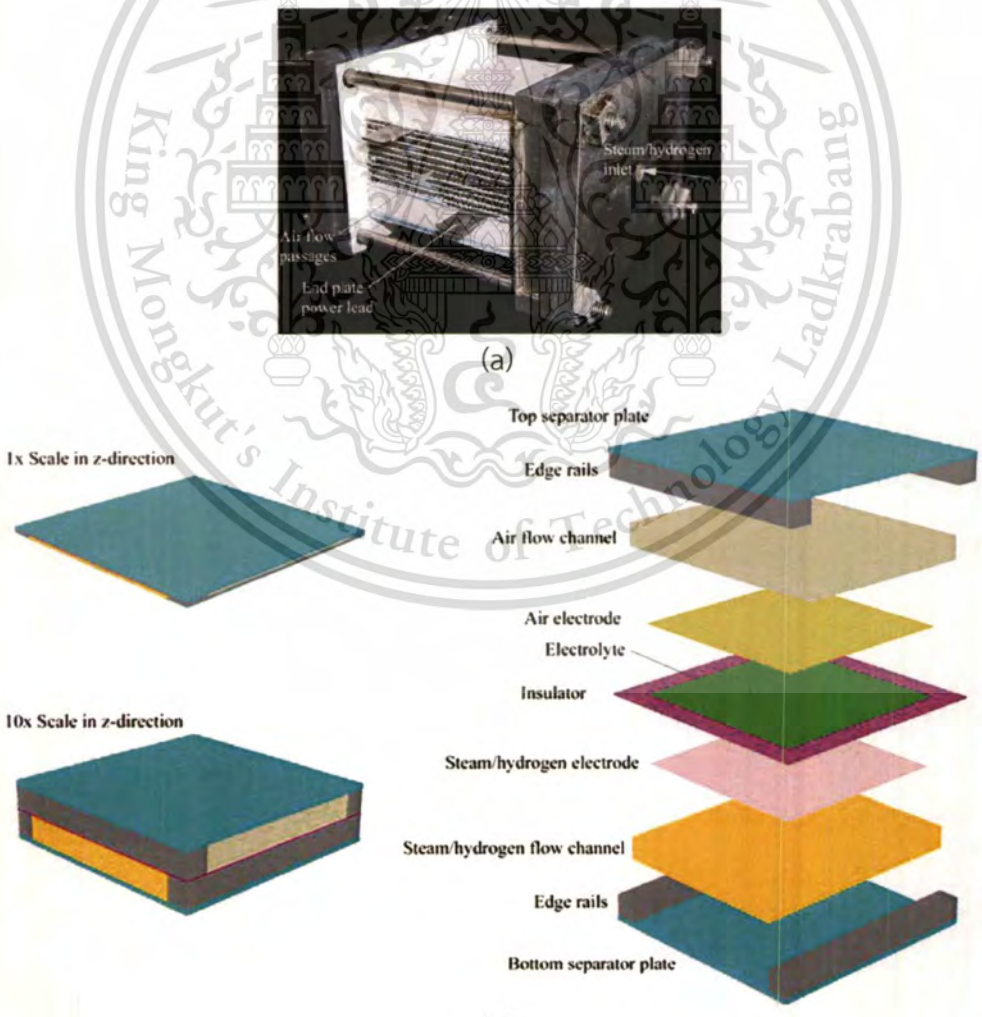

Figure 2.1: The detail of SOEC (a) stack (b) single-cell [3].

The reaction which occurred in electrolytic cell is the reverse of the reaction occurring in the fuel cell. The electrochemical reactions occurring within the cell are shown in Fig.2.2. Electrons are forced to the negative electrode (cathode) by an external voltage supply. Steam is fed to the cathode (steam electrode) while an electrical energy is applied to the SOEC in order to dissociate the molecules of water to form hydrogen gas and oxygen ions, O^{2-}, at the triple-phase boundary, as shows in Fig.2.3. Then the hydrogen gas diffuses through cathode to the gas stream and gets collected while the oxygen ions are transported through the electrolyte to the porous anode (air electrode), where they are oxidized to oxygen gas and thus release electrons [5]. The electrochemical reactions occurring are:

Anode reaction (+): $2O^{2-} \longrightarrow O_2 + 4e^-$ (2.1)

Cathode reaction (-): $2H_2O + 4e^- \longrightarrow 2H_2 + 2O^{2-}$ (2.2)

Overall reaction: $2H_2O \longrightarrow 2H_2 + O_2$ (2.3)

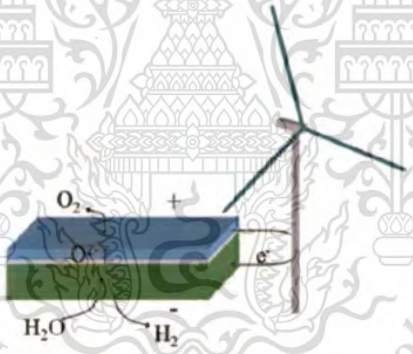

Figure 2.2: Working principle of a solid oxide electrolytic cell [5].

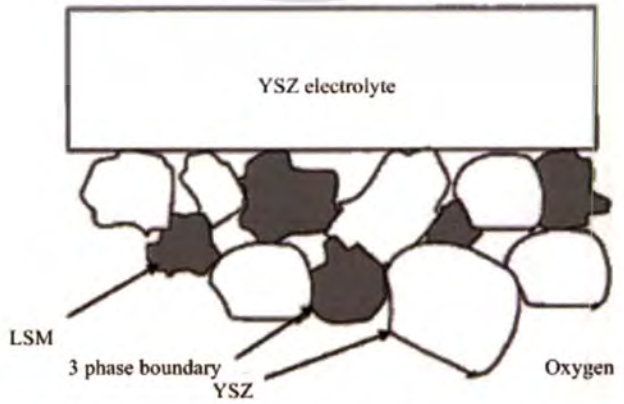

Figure 2.3: Concept of extended three-phase boundary at anode/electrolyte interface [12].

The cost of electrolysis is due to electricity demand. The total energy demand (ΔH) for SOEC hydrogen production is expressed by

$$\Delta H = \Delta G + T\Delta S \quad (2.4)$$

where ΔG = the electrical energy demand

$T\Delta S$ = the thermal energy demand.

Thermodynamics of steam electrolysis for hydrogen production are shown in Fig.2.4. In case of increasing the operating temperature, the electrical energy demand will decrease whereas the thermal energy demand will increase. However, the total energy demand does not change with temperature significantly [5].

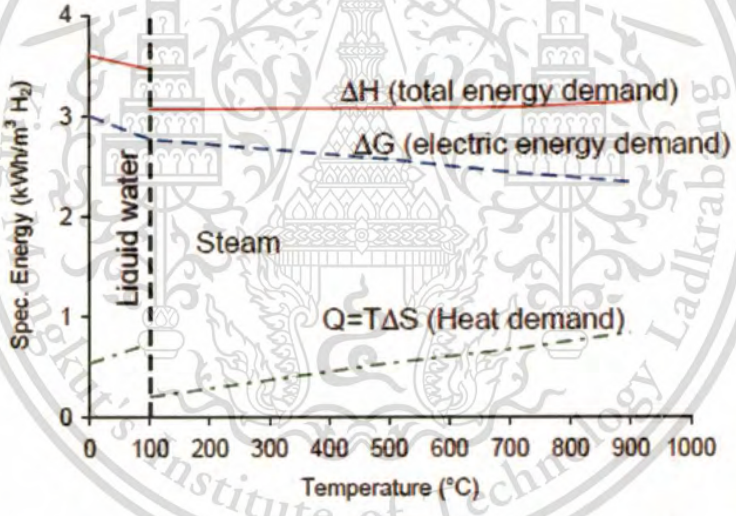

Figure 2.4: Thermodynamics of steam electrolysis for hydrogen production [5].

Due to high temperature operation (700-1,000 °C), the components of SOEC have to tolerate to high temperature. The electrodes must also conduct the electrons and oxide ions, and must be porous in order to get the gases into the reaction sites and to have large boundary area where the three species (gas molecules, oxide ions and electrons) can react. Moreover, coefficient of thermal expansion (CTE) of electrodes must close to that of the electrolyte. The electrolyte must be gastight and electron insulating while interconnector has to be chemical stable in reducing or oxidizing environments and gas impermeability. Hence, to prove

all required properties as above, electrolyte is typically made of yttria stabilized zirconia (YSZ), anode or O_2 electrode is typically made of YSZ and lanthanum strontium manganese (LSM), and cathode or negative electrode is generally made of YSZ and Ni [1, 21]. Interconnector is usually made from ceramic which was operated at 1000 ^{o}C. Recent progress in reducing the SOEC operating temperature from 1,000 °C to about 600–800 °C is using other interconnector materials, i.e. metallic alloys.

2.1.2 Interconnectors

Interconnector is one component in high temperature SOEC which must be electrical connection between cells and must separate gas within the cell stack. The materials used as interconnectors must be compatible with other cell components as well as stable in both oxidizing and reducing atmospheres. The constraints of cost and ease of fabrication also limit the possible material choices. Typical materials applied as interconnector are ceramics and metallics. The interconnector which is made from perovskite oxide ceramics based on rare earth chromites are operated at 900-1,000 ^{o}C. For lower temperature operation (600-800 ^{o}C), the metallic alloys are preferably applied as interconnectors. The properties required for interconnector design are [10, 12-14]:

- High electronic conductivity with low ionic conductivity
- Thermal expansion match to other cell components
- Chemical stability with regard to other cell components
- High mechanical strength
- High thermal conductivity

The first three properties required are important and eliminating most candidate material. For temperature operation above 800 ^{o}C, rare earth chromites satisfy most of the requirements, but have the problems in fabrication and high cost. Metallic materials are easier to fabricate and have lower cost in comparison with ceramics. These characteristics make this material as a promising candidate for applying as interconnectors.

2.2 Literature reviews

2.2.1 Oxidation of the uncoated Fe-Co-Ni alloy

Fe–Co–Ni alloy is a low thermal expansion coefficient alloy which can probably be used as an interconnector in SOEC. For ternary Fe–Ni–Co alloys, Kim et al. [15] studied the oxidation behavior of Fe-30%Ni-12.5%Co alloy in the range of temperatures of 1,000-1,200 °C in air for 1-100 h. The chemical composition of samples is shown in Table.2.1.

Table 2.1 Chemical composition of sample in Kim et al.'s studied [15].

Fe	Ni	Co	Mn	Al	Si	P	S	C
Bal.	30.48	12.59	0.001	0.027	0.021	0.017	0.001	0.02

They found that the weight gain per area (ΔM/A) rapidly increased with oxidation temperature, and increased as a parabolic function of time as shows in Fig.2.5. The activation energy derived from the weight gain per area with time for the whole scale was 19.84 kcal.

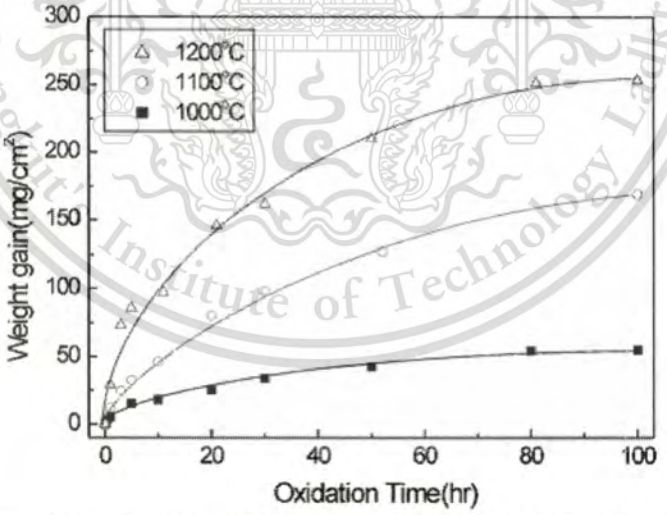

Figure 2.5: The weight gain per area versus oxidation time of Fe-30%Ni-12.5%Co alloy oxidized in air [15].

The cross section image of sample after oxidation at 1,100 °C in air is shown in Fig.2.6. They found that the oxide layers consisted of external oxidation layer and internal oxidation layer. The EDS and XRD results showed that the major outermost

scale consisted of a mixture of $CoFe_2O_4$ containing a small quantity of Fe_2O_3 or the sequence of $CoFe_2O_4$ and Fe_2O_3 at all temperatures of 1,000-1,200 °C.

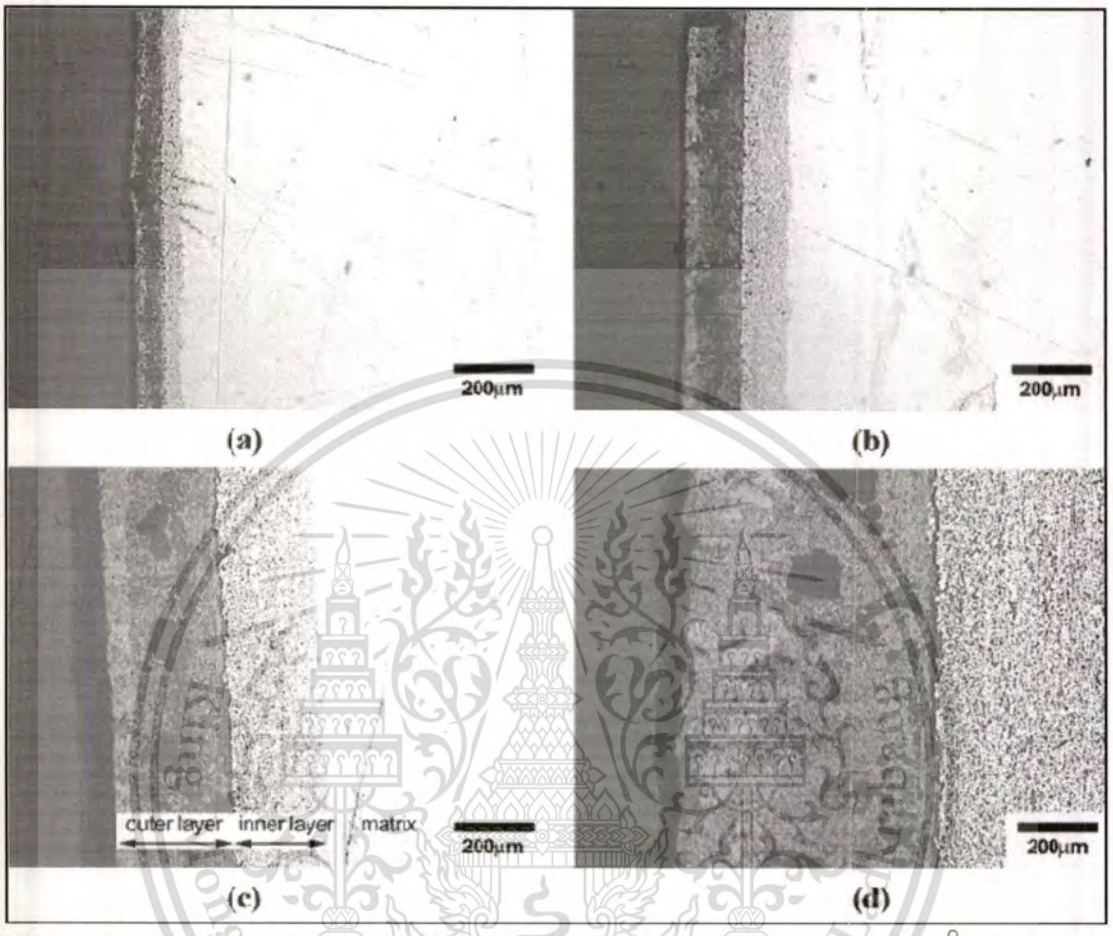

Figure 2.6: Micrographs of Fe-30%Ni-12.5%Co alloy oxidized at 1,100 °C in air for (a) 1 hr (b) 3 hr (c) 10 hr and (d) 50 hr [15].

Chapman et al. [16] studied the influence of cobalt addition on the high temperature oxidation behavior of Ni–Fe alloys at 800 °C in air. They found that on the alloy which had ratio of Ni:Fe as 1:1 and 10 wt.%Co, the weight gain per area increased by oxidation time as parabolic function, as shows in Fig.2.7.

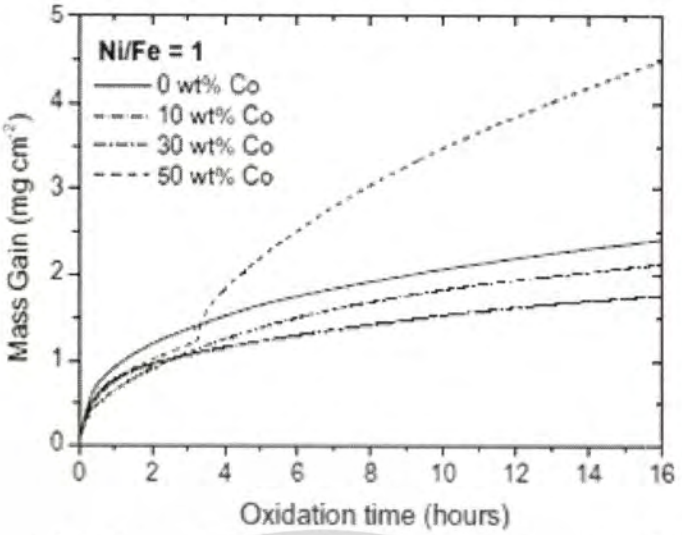

Figure 2.7: The weight gain per area versus oxidation time of Ni–Fe–Co alloys oxidized in air at 800 °C using thermobalance [16].

Moreover, the scale composition which was formed after oxidation at 800 °C in air was also investigated using XRD, SEM and EDS. They found that the alloys with 10 wt.% Co and ratio of Ni:Fe as 1:1 formed iron-rich scales. The most composition of scale was $Ni_xFe_{3-x}O_4$. The growth of hematite (Fe_2O_3) was also observed at the atmosphere interface. Because Co had strong outwards diffusion, Co diffused to the atmosphere interface and then formed $Co_xFe_{3-x}O_4$ at the outer scale. It was confirmed by XRD peaks of $Co_xFe_{3-x}O_4$ which significantly grew after oxidation, as seen in Fig.2.8.

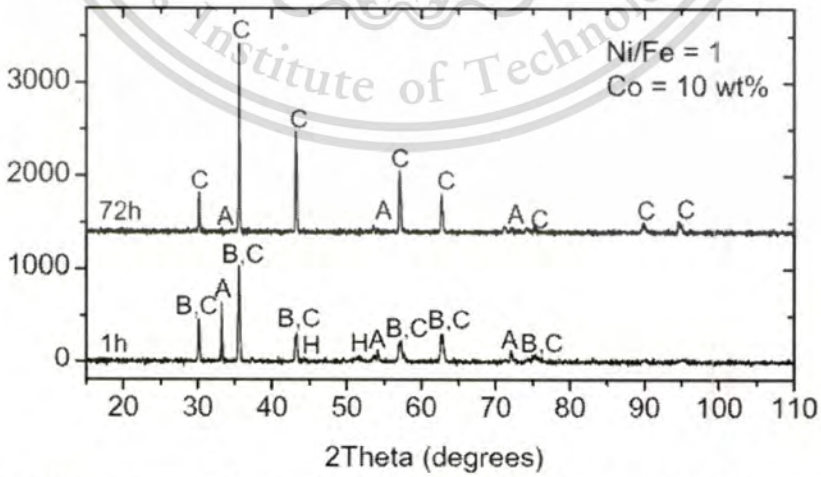

Figure 2.8: XRD pattern of scales forming on Ni–Fe–Co alloys after oxidation at 800 °C in air for 1 and 72 h. (A) Fe_2O_3, (B) $Ni_xFe_{3-x}O_4$, (C) $Co_xFe_{3-x}O_4$, (H) $FeNi_3$ [16].

Cross section image and EDX line scans which were performed on oxidized Ni–Fe–Co alloys of the scale after oxidation for 72 h at 800 °C in air are shown in Fig.2.9. It was found that the scale occurring consisted of three layers: $Ni_xFe_{3-x}O_4$, Fe_2O_3 and $Co_xFe_{3-x}O_4$, respectively.

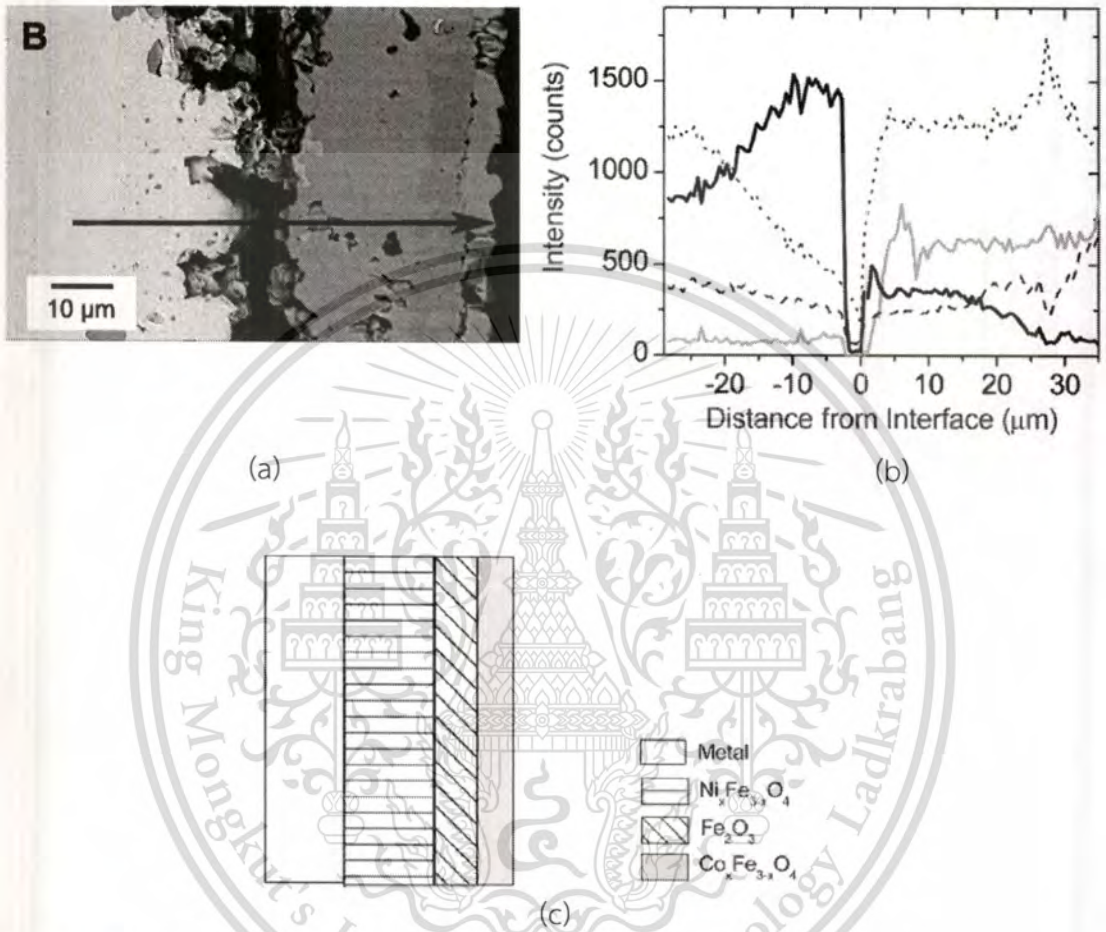

Figure 2.9: Cross section image (a), EDX line scans (b) and schematic diagram (c) performed on oxidized Ni–Fe–Co alloys (Ni:Fe = 1:1 with 10 wt.% Co) after 72 h at 800 °C in air [16].

Zhu et al. [17] studied the isothermal oxidation behavior of Al or Cr addition on low thermal expansion FeCoNi alloy in air at 800 °C comparing with Crofer 22 APU for evaluating as an interconnector for reducing temperature operation in SOFC. The compositions of samples are shown in Table.2.2.

Table 2.2 The compositions of the alloys in Zhu et al.'s studied (wt. %) [17].

	Fe	Co	Ni	Cr	Nb	Ti	Si	Al	B
Three-Phase	Bal	18	42	-	3.0	1.5	-	6.0	-
EXP 4005	Bal	31	33	-	3.0	0.6	-	5.3	-
Thermo-Span	Bal	29	24.5	5.5	4.8	0.85	0.35	0.45	0.004
HRA 929C	Bal	22.5	29.5	2.0	4.0	1.25	0.3	0.55	0.0045

They found that the oxidation kinetics rate of these alloys at 800 °C in air was significantly higher than that of Crofer 22 APU, as seen in Fig.2.10.

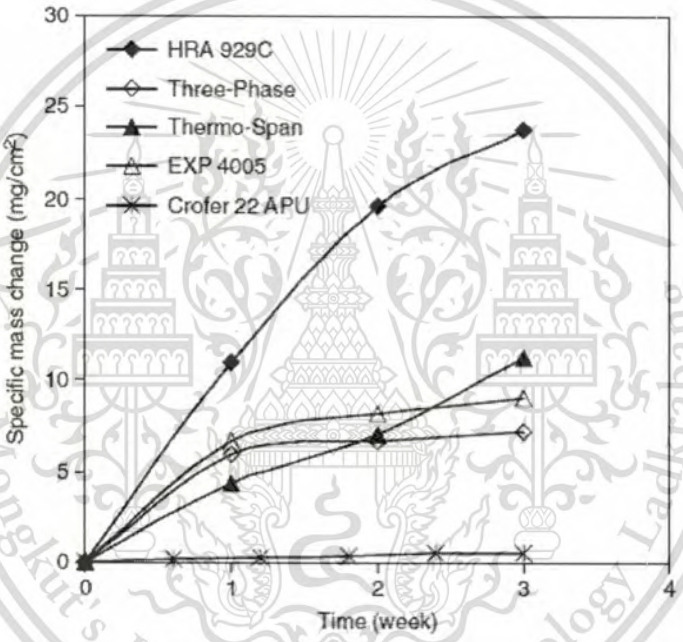

Figure 2.10: The weight gain per area versus time of samples oxidized at 800 °C in air [17].

The results showed that the oxidation kinetics rates of Cr-addition alloys were higher than those of Al-addition alloys. For Cr-addition alloys, the mass gain increased continuously with oxidation time. It could be indicated that there were not protective oxide scale forming on these alloys. For Al-addition alloys, the mass gain increased only slightly with oxidation time after the first week, this meaned that a protective oxide layer must formed between the substrate and the surface oxide(s) during the initial oxidation. According to the alloy compositions and XRD results,

the protective oxide layer formed on these two alloys should be Al_2O_3. Cross section images of these samples were shown in Fig.2.11.

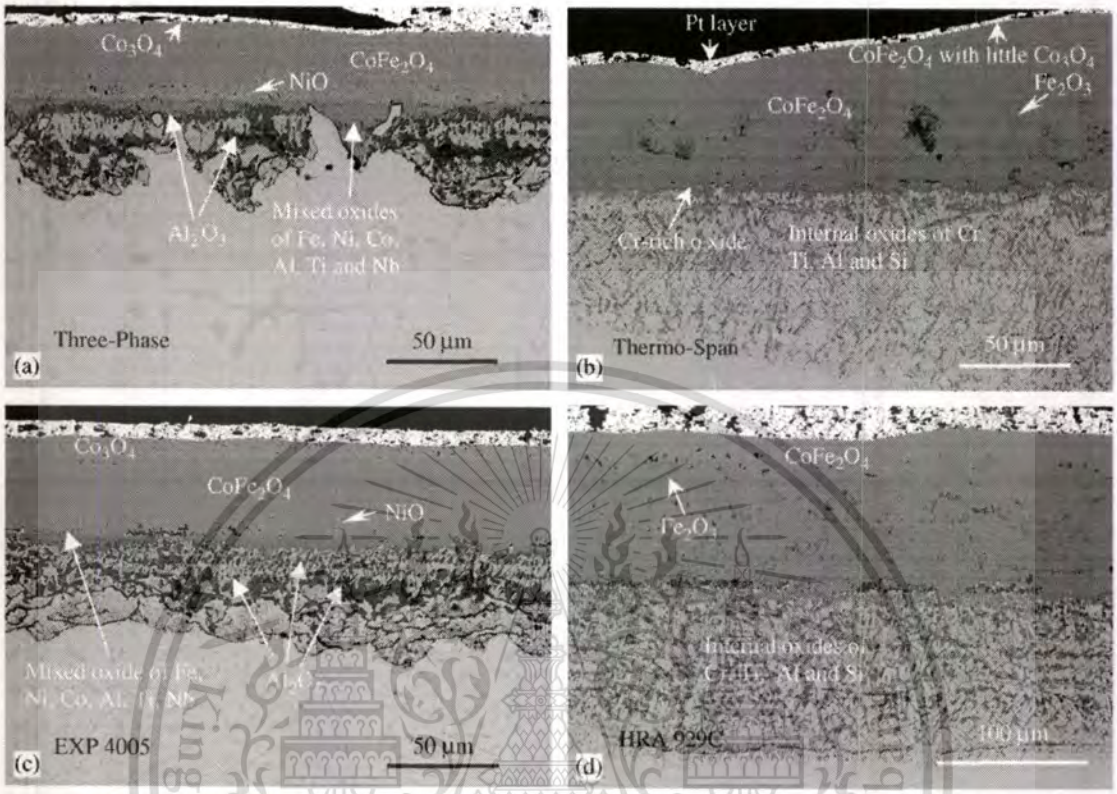

Figure 2.11: Cross-section images of the four alloy samples after oxidation for three weeks at 800 °C in air. (a) Three-Phase (b) Thermo-Span (c) EXP 4005 (d) HRA 929C [17]

They observed that for the Al-addition FeCoNi alloy, the scales of Co_3O_4, $CoFe_2O_3$ and NiO were formed. The Al_2O_3-rich layer formed on Three-Phase (6.0 wt.% Al-FeCoNi alloys) (Fig.2.11a) was more continuous than that of EXP 4005 (5.3wt.% Al-FeCoNi alloys) (Fig.2.11c). This meaned that Three-Phase (6.0 wt.% Al-FeCoNi alloys) (Fig.2.11a) exhibited better oxidation resistance than EXP 4005 (5.3 wt.% Al-FeCoNi alloys) (Fig.2.11c). For Cr-addition FeCoNi alloy, the scale of $CoFe_2O_4$ and Fe_2O_3 were formed, whereas Co_3O_4 layer was only formed on Thermo-Span (5.5 wt.% Cr-FeCoNi alloys) (Fig.2.11b). The oxidation resistance of Thermo-Span (5.5 wt.% Cr-FeCoNi alloys) (Fig.2.11b) was more than that of HRA 929C (2.0 wt.% Cr-FeCoNi alloys) (Fig.2.11d) due to the formation of a Cr-rich oxide layer at the interface between the oxide scale and substrate of Thermo-Span (5.5 wt.% Cr-FeCoNi alloys) (Fig.2.11b).

2.2.2 Perovskite and spinel coatings

For improving the oxidation resistance of alloys, coatings on alloys are performed. In this research, the perovskite coating (LSM and LNF) and spinel coating (Co_3O_4 and $MnCo_2O_4$) were studied. Shaigan et al. [7] demonstrated that the coating had been considered as a solution of the poor oxidation problem at high temperatures and oxide scale properties. Various materials had been used to decrease the oxidation rate, improve the adhesion of oxide scale and metal, increase the oxide scale conductivity and inhibit the Cr evaporation. The materials which were used as coating were reactive element oxides, conductive perovskites, conductive spinels, etc. The coating methods include sol-gel technique, physical vapor deposition technique, electrodepositing technique, screen printing and slurry coating technique, etc.

The addition of some amount of reactive element oxide (e.g., La, etc) could improve the adhesion between oxide scale and metal. Moreover, the coating containing reactive element oxide had an effective in reducing the high temperature oxidation rate, therefore oxide scale thickness reduced and thus the ASR of interconnector decreased. However, these coatings were not effective in inhibiting the Cr evaporation. The most popular techniques which were applied with reactive element oxide were sol-gel and chemical vapor deposition.

Other material, rare earth perovskite coatings, general formula as ABO_3 where A is a large trivalent rare earth cation (e.g., La or Y), and B is usually a trivalent transition metal cation (e.g., Cr, Ni, Fe, Co, Cu or Mn), as shows in Fig.2.12. The advantages of being the perovskite coatings are electronically conductive, exhibiting compatible CTE. Application of these coatings should decrease the oxidation rate, improve scale adhesion and reduce the ASR. However, perovskites are not suitable for protective purposes as they could conduct oxygen ions. The most commonly used perovskites for electronically conductive coating purposes are lanthanum strontium manganites (LSM; $La_{1-x}Sr_xMnO_3$), lanthanum strontium cobaltites (LSC: $La_{1-x}Sr_xCoO_3$), etc. Perovskite coating may be applied on stainless steel substrates by a variety technique including radio-frequency (rf) magnetron sputtering, sol–gel and pulsed laser deposition [7].

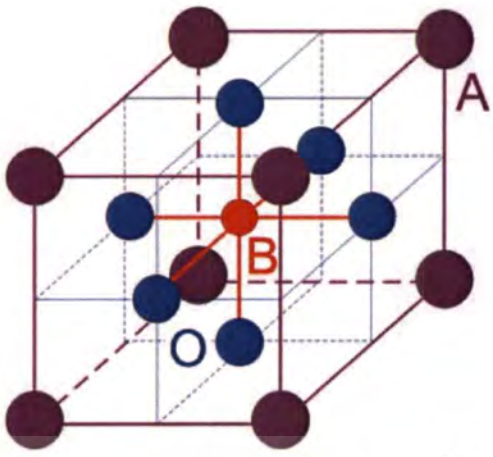

Figure 2.12: The schematic representation of the perovskite lattice structure (ABO_3) [18].

For spinel coatings, spinel has the general formula of AB_2O_4 where A and B are divalent, trivalent or quadrivalent cations in octahedral and tetrahedral sites and oxygen anions are on the face centre cubic (FCC) lattice sites, e.g. $MnCo_2O_4$, Co_3O_4, etc., as shows in Fig.2.13. Spinels have good electronic conductor. Moreover, their CTEs well match with the ferritic stainless substrate and other cell components. It is well known that spinel coatings have performance in absorption of Cr species which migrated from the chromia scale. In the past, coating methods for spinel coating were spraying or screen printing and plasma spraying. Recently, coating by electrodepositon method and heat treatment has been interested as a technique for spinel coating.

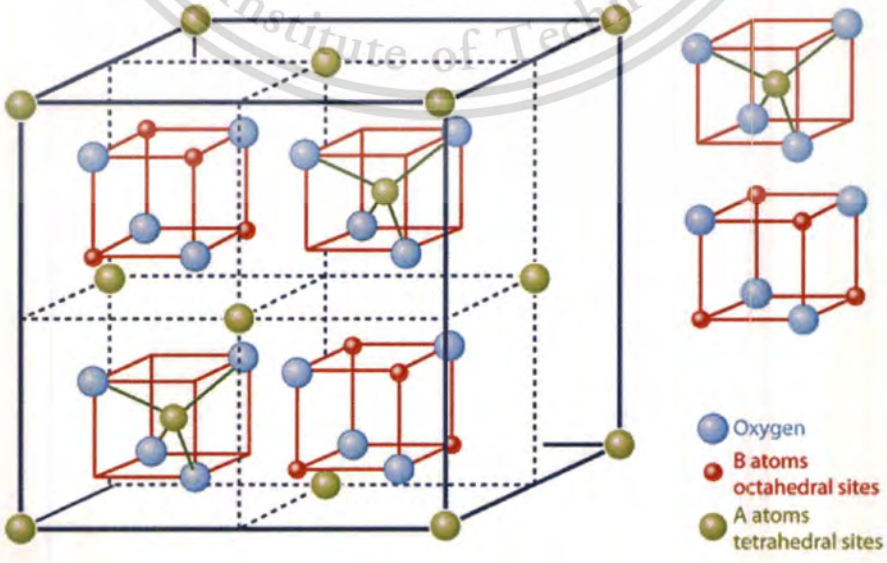

Figure 2.13: The schematic representation of the cubic spinel structure (AB_2O_4) [19].

Palcut et al. [20] studied the oxidation behavior of Crofer 22 H, Crofer 22 APU, E-Brite and AL 29-4C. The samples were coated by $La_{0.85}Sr_{0.15}MnO_{3-\delta}$ (LSM) by plasma spraying method. The experiment was carried out at 850 °C at a total flow rate of 6 L/h of two different atmospheres as pure O_2 and air-1%H_2O. SEM images of sample after coated are shown in Fig.2.14. They found that the thickness of coating was 25-30 μm. The coating was dense, but cracked.

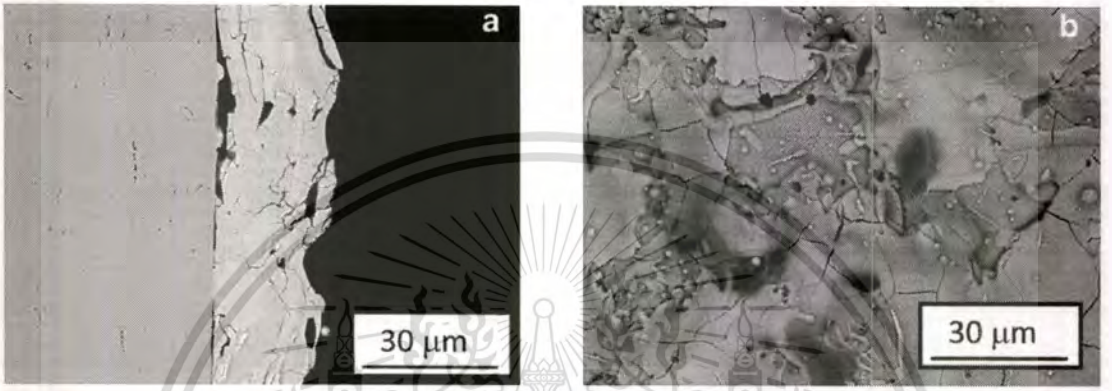

(a) (b)

Figure 2.14: SEM images of the coated sample after deposited the LSM coating by plasma spraying method. (a) cross section (b) surface [20].

The XRD patterns of LSM coated sample before and after oxidation at 850 °C for 3 h and for 100 h are shown in Fig.2.15. They found that the perovskite structure formed after heat treatment. Moreover the La_2O_3 peaks were also found. They expected that this phase had formed during spraying. SEM image of the surface of this sample after oxidation showed that there were relatively small of La_2O_3 phase located at the surface sample as isolated islands, as seen in Fig.2.16. This phase probably did not influence to coating properties.

The SEM cross section images, Fig.2.17, showed that after oxidation the morphology of coating did not change, but there was oxide with a thickness of 2-3 μm forming between steel and the coating. The EDS results indicated that the oxide scale formed probably was duplex scale which consisted of inner layer of chromium oxide (Cr_2O_3) and outer layer of manganese chromium oxide $(Mn,Cr)_3O_4$.

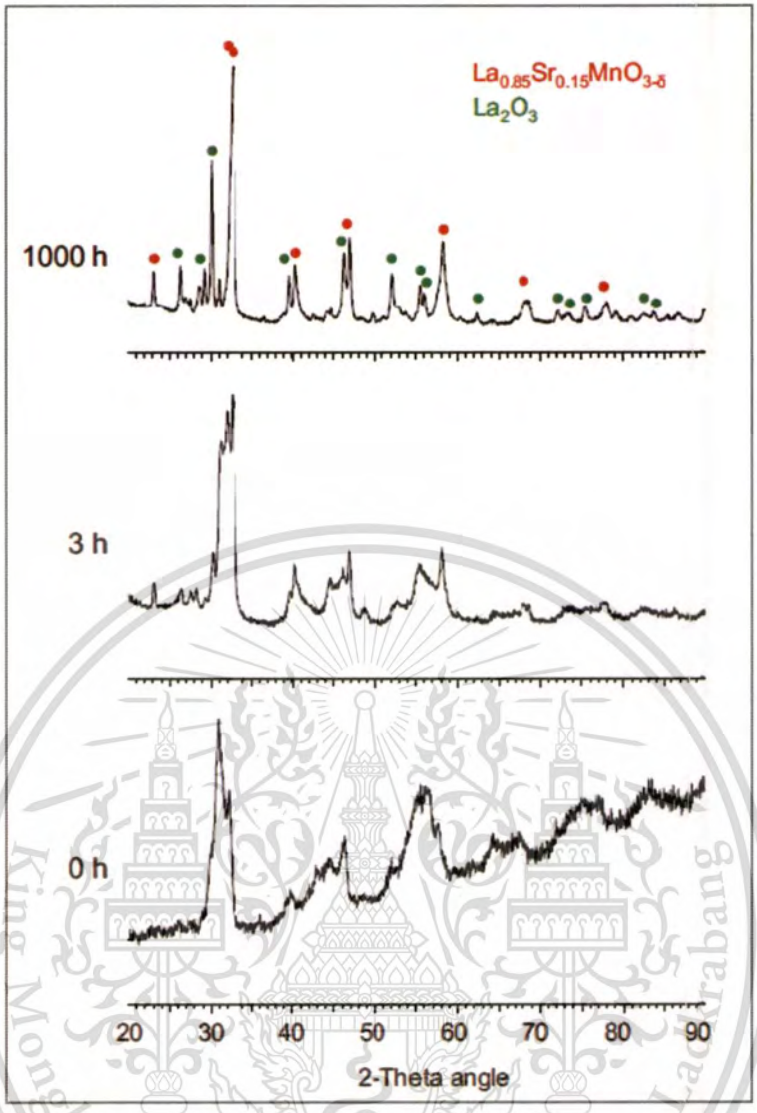

Figure 2.15: XRD patterns of the coating before and after the oxidation for 3 h and 1000 h at 850 °C [20].

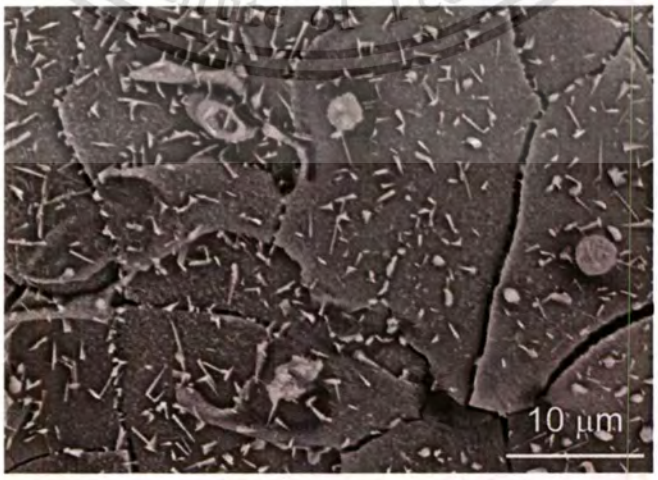

Figure 2.16: Morphology of needle-like La_2O_3 particles on the surface after the oxidation experiment [20].

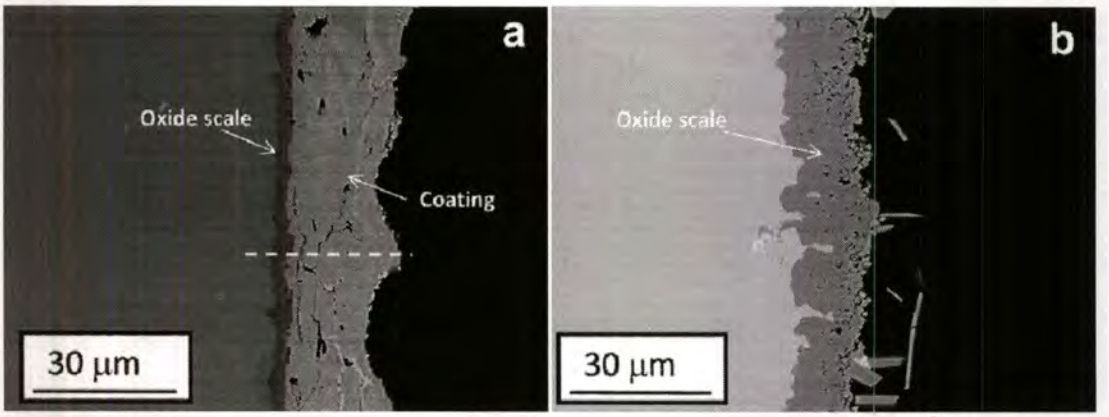

Figure 2.17: Cross section images of samples after oxidation at 850 °C for 1000 h in O_2 (a) LSM coated sample (b) uncoated Crofer 22 APU [20].

Moreover, the oxidation kinetics was also studied. The weight gains per area of samples which was oxidized in O_2 or in air+1%H_2O at 850 °C increased as a parabolic function of time. The parabolic rate constant for this experiment are shown in Table.2.3.

Table 2.3 Parabolic rate constant of samples oxidized at 850 °C [20].

Steel	10^{14} k_p (g^2 cm^{-4} s^{-1})				$k_{p(coated)}/k_{p(uncoated)}$	
	Uncoated		$La_{0.85}Sr_{0.15}MnO_3$ coating			
	Air+1%H_2O	O_2	Air+1%H_2O	O_2	Air+1%H_2O	O_2
Crofer 22 APU	18.9	18.9	16.1	19.0	0.85	0.10
Crofer 22 H	30.7	50.3	15.1	32.0	0.49	0.64
E-Brite	25.0	35.4	11.8	28.7	0.47	0.81
AL 29-4C	29.0	39.4	7.84	18.6	0.27	0.47

The results showed that the LSM coating was oxygen transport barrier. LSM coating could reduce the oxygen partial pressure at the interface between the coating and chromium scale. This had significant in reducing the oxidation rate. However, the LSM coating was not able to eliminate the outward chromium diffusion completely. This coating probably did not influence to the reaction mechanism. The perovskite coating had higher electronic conductivity comparing with spinel coating. Moreover, it was compatible with other cell components.

Chen and Jiang [21] investigated the polarization and delaminating behavior of LSM oxygen electrode under SOEC operating conditions. The experiment was carried out under anodic current passage of 500 mA cm^{-2} and 800 ^{o}C. The delaminating or failure of LSM oxygen electrode was observed after the current passage treatment for 48 h. The micrographs of sample are shown in Figs.2.18 and 2.19.

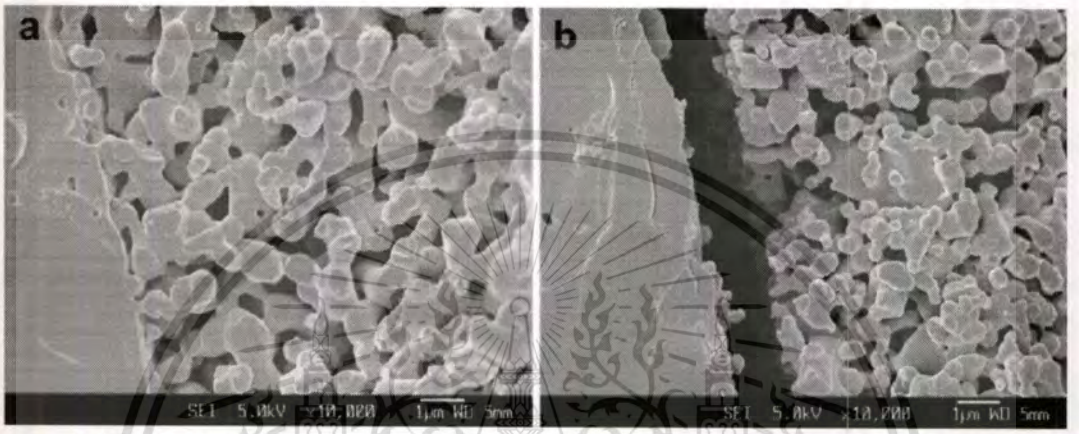

Figure 2.18: Cross-section images of LSM oxygen electrode/YSZ electrolyte interface (a) before (b) after anodic polarization at 500 mA cm^{-2} and 800 ^{o}C for 48 h [21].

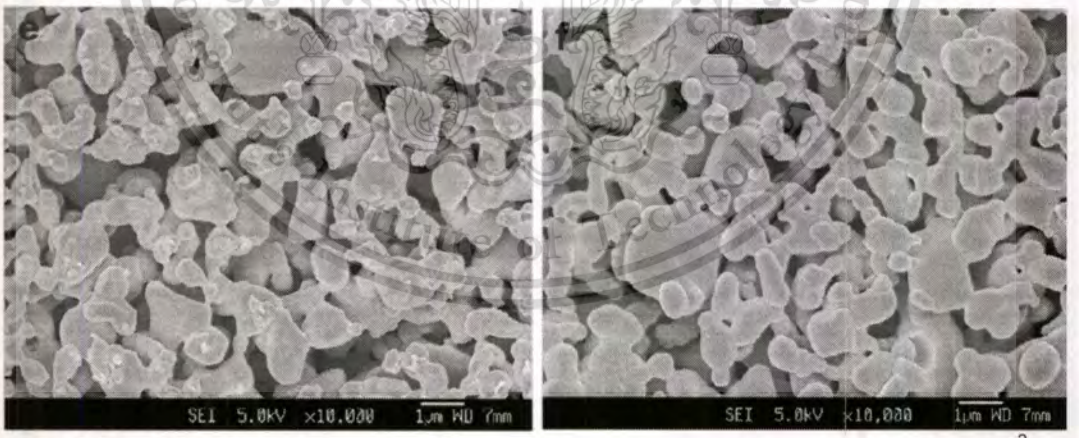

Figure 2.19: SEM of sample after the anodic current passage at 500 mA cm^{-2} and 800 ^{o}C for 48 h: (e) inner surface of LSM oxygen electrode in contact with YSZ electrolyte (f) surface of LSM oxygen electrode exposed to the air side [21].

The interface between electrode and electrolyte at different stages of polarization were characterized by SEM. The results indicated that the delaminating

of LSM oxygen electrode from electrolyte occurred due to the formation of nanoparticles which affected disintegration of the LSM particles at the electrode/electrolyte interface. The formation of nanoparticles within LSM particles occurred due to the migration of oxygen ions from the YSZ electrolyte into LSM grain bulk. Therefore, manganese ions were oxidized, and formed manganese cation vacancies. Hence LSM lattice was shrinkage. The shrinkage of LSM lattice would lead to the local tensile strains within the LSM particles and subsequent formation of microcracks and nanoparticles at the interface. The schematic illustrations of delaminating behavior of the LSM oxygen electrode/YSZ electrolyte interface under SOEC operation conditions are shown in Fig.2.20.

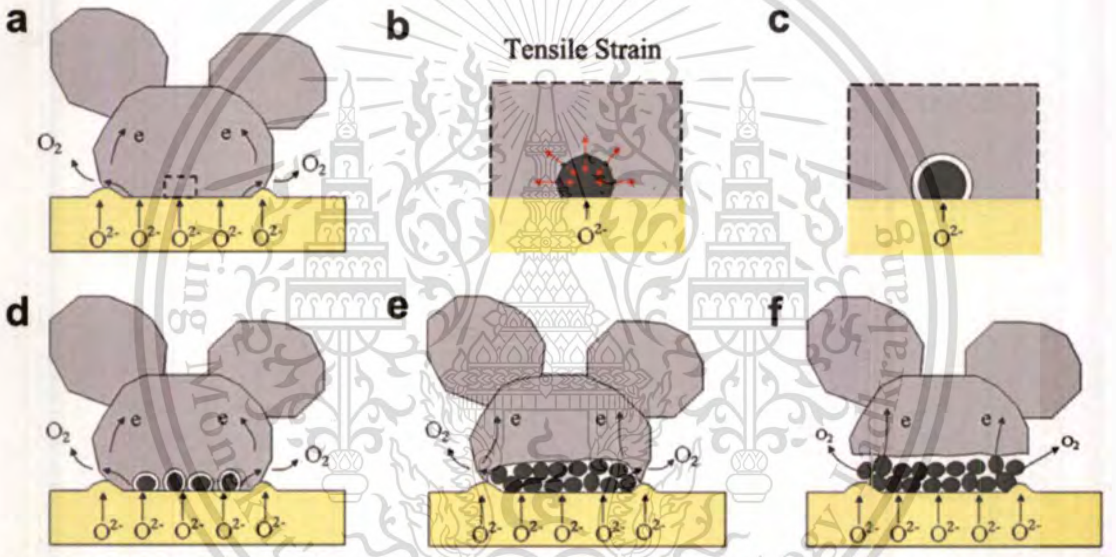

Figure 2.20: Schematic illustrations of the microstructural change of the LSM oxygen electrode/YSZ electrolyte interface under SOEC operation conditions: (a) oxygen migrate from YSZ electrolyte (yellow area) to LSM grain (gray area) at the interface, (b) local tensile strains within the LSM particles due to the shrinkage of the LSM lattice, (c) local tensile strains contributed to microcrack formation, (d) formation of the individual nanoparticles (black spot), (e) propagation and continuous formation of nanoparticles whereas the LSM grain bonded with the YSZ electrolyte through bridges along edge of the convex contact ring, (f) formation of complete nanoparticle layers lead to delaminate of the LSM oxygen electrode and YSZ electrolyte under high internal oxygen partial pressure at the interface [21].

Chiba et al. [22] investigated the composition dependence of the characteristics in the $LaNi_{1-x}Fe_xO_3$ (x = 0.0-1.0) system. They demonstrated that perovskite type oxides (ABO_3) containing Co ions in B sites had much higher conductivity than that of $La_{1-x}Sr_xMnO_3$ (LSM) which was most commonly used as cathode material. However, the thermal expansion coefficients of these materials (22.0×10^{-6} K^{-1}) were larger than that of $La_{0.8}Sr_{0.2}MnO_3$ (12.0×10^{-6} K^{-1}). They found that $LaNi_{1-x}Fe_xO_3$ had both high electronic conductivity and thermal expansion coefficient which were close to those of the zirconia electrolyte. Therefore, they thoroughly investigated the composition dependence of the characteristics in the $LaNi_{1-x}Fe_xO_3$ (x = 0.0–1.0) system. The samples were prepared by a solid state reaction. The electronic conductivity at 800 °C of $LaNi_{1-x}Fe_xO_3$ is shown in Fig.2.21.

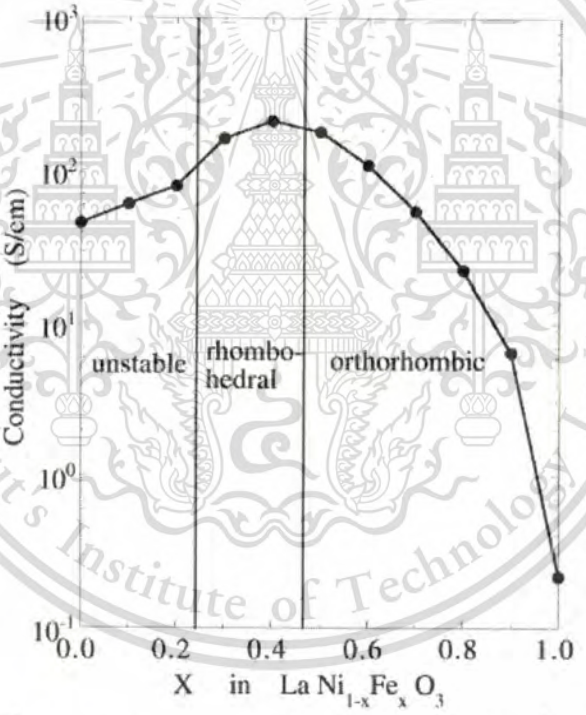

Figure 2.21: Composition dependence of electronic conductivity at 800°C of $LaNi_{1-x}Fe_xO_3$ (x=0.0, 0.1, 0.2, 0.3, 0.4, 0.5, 0.6, 0.7, 0.8, 0.9, 1.0) [22].

They found that when x in $LaNi_{1-x}Fe_xO_4$ was greater than 0.4, the samples were in the orthorhombic phase. When x was 0.4, they were in the rhombohedral phase. When x was between 0.3 and 0.2, they were basically in the rhombohedral phase, but also contained the orthorhombic phase. When x was smaller than 0.2, the samples were a mixture of the orthorhombic and tetragonal phases. When x in

$LaNi_{1-x}Fe_xO_4$ was 0.4, this system had its highest electronic conductivity of 580 S/cm, at 800 °C. This value was more than three times higher than that of $La_{0.8}Sr_{0.2}MnO_3$. The average thermal expansion coefficient of $LaNi_{0.6}Fe_{0.4}O_3$ from 30 to 1,000 °C was relatively low ($11.4x10^{-6}$ K^{-1}) and closer to the CTE of $0.92ZrO_2$–$0.08Y_2O_3$ (YSZ), $10.0x10^{-6}$ K^{-1}, than that of $La_{0.8}Sr_{0.2}MnO_3$ ($12.0x10^{-6}$ K^{-1}).

Petric and Ling [23] studied the thermal and electrical properties of spinel such as Mn, Co, etc. They found that spinels containing Fe had the closest CTE values with ferritic stainless steels ($11x10^{-6}$ $°C^{-1}$). $MnCo_2O_4$ spinel had highest conductivities (60 S cm^{-1} at 800 °C). The authors said that $Mn_xCo_{3-x}O_4$ and Co_3O_4 were suitable to be the candidates of interconnector coatings. Some CTEs and conductivities of spinels at 800 °C are shown in Table 2.4.

Table 2.4 CTE and conductivity of some spinel at 800 °C [23].

Spinel	$NiFe_2O_4$	$CoFe_2O_4$	Co_3O_4	$MnCo_2O_4$
Electrical conductivity (S cm^{-1})	0.26	0.93	6.7	60
CTE ($x10^{-6}$ $°C^{-1}$).	10.8	12.1	9.3	9.7

Burriel et al. [24] studied the Co_3O_4 spinel coating on Fe–22Cr metallic which was expected to use as interconnectors in intermediate temperature SOFC. Cobalt oxide was prepared by pulsed injection metal organic chemical vapor deposition (PI-MOCVD). The structure, morphology and growth rate of the spinel layers which was deposited on substrate were studied in function of deposition temperature. The spinel was deposited at pressure 1.33 kPa and a total gas flow rate of 8.83 cm^3/s of O_2 (reactive gas) + 10 cm^3/s of Ar (carrier gas) at 500 °C. The samples were analyzed by XRD, SEM and EDS.

The Co_3O_4 spinel coating which was deposited on Fe–22Cr metallic at 500 °C had a thickness of 2 μm. SEM images are shown in Fig.2.22. They found that the film which had grain size of approximately 1 μm were highly dense. XRD pattern indicated that there was the polycrystalline of Co_3O_4, as shows in Fig.2.23. Moreover, some amount of CoO phase was also found.

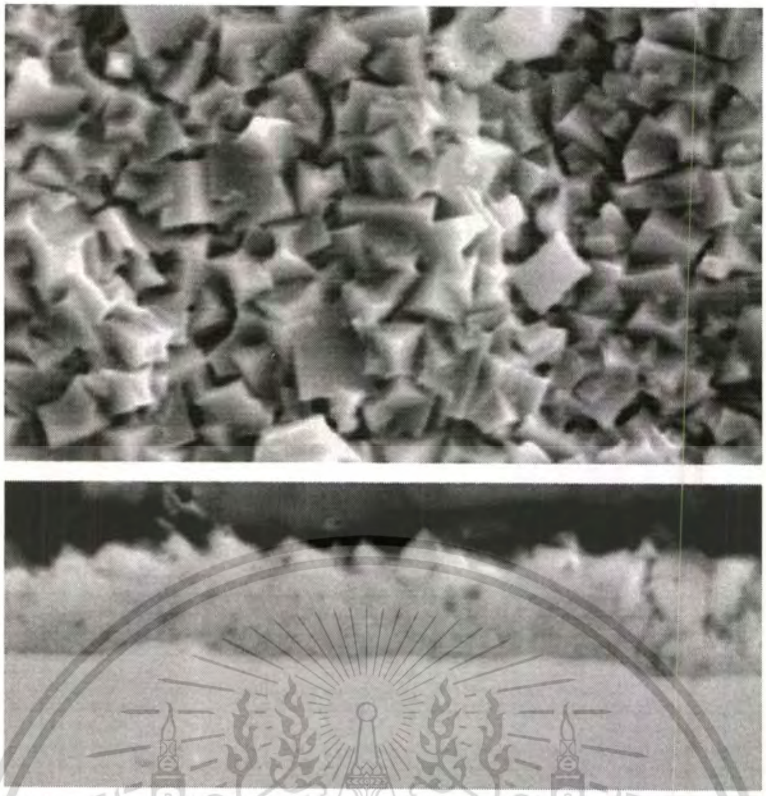

Figure 2.22: SEM micrographs of (a) the surface and (b) cross-section of Co_3O_4 layers deposited on Fe–22Cr substrates at 500 °C [24].

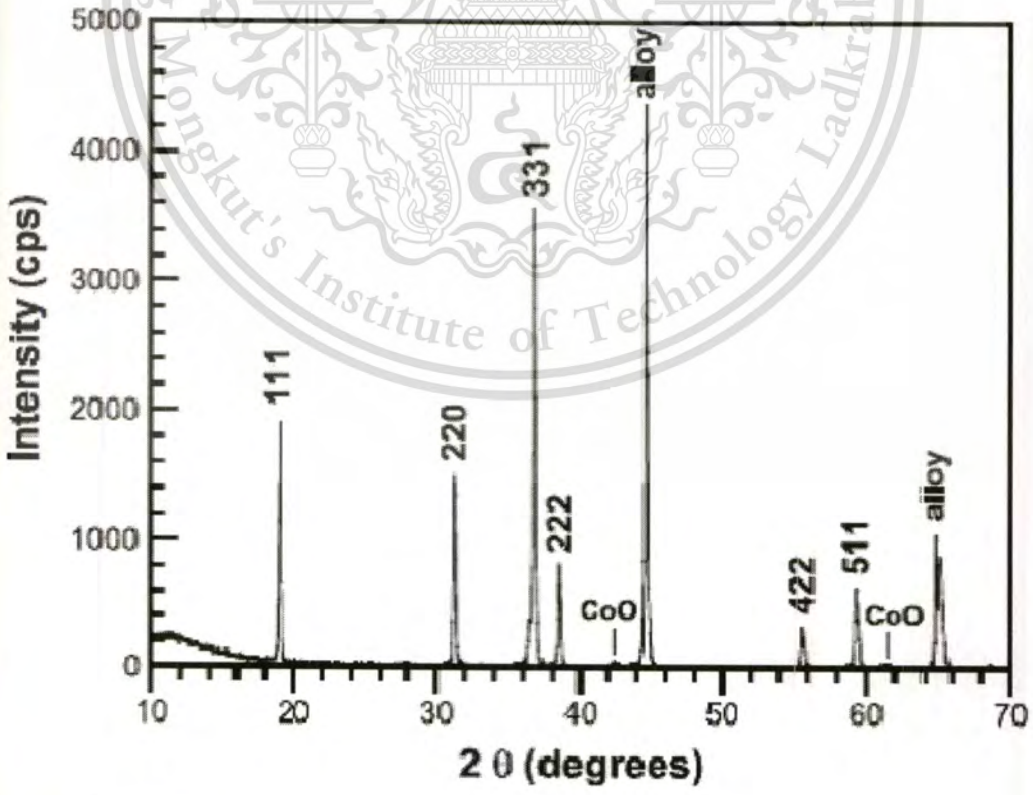

Figure 2.23: XRD pattern of Co_3O_4 layers deposited on Fe–22Cr substrates by PI-MOCVD at 500 °C [24].

Wei et al. [25] studied the oxidation resistance and electrical properties of the Mn–Co oxide coating on AISI 430 substrates for solid oxide fuel cell interconnector application. The Mn-Co-O coatings were coated on substrate by electrodeposition method. SEM images of sample before pretreated are shown in Fig.2.24. SEM images indicated that the morphology of Mn–Co oxide coating surface before pretreated was rough but without crack.

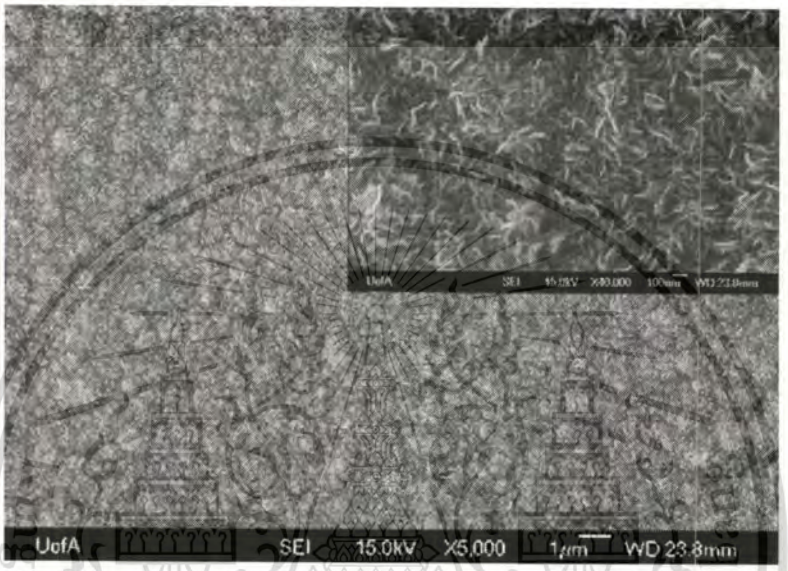

Figure 2.24: SEM image of Mn–Co oxide coatings on AISI 430 substrates before pretreated [25].

Mn–Co coated samples were pretreated at 800 °C for 10 h before oxidation in air or in 5% H_2–95% N_2. The morphologies of sample after pretreated in air are shown in Fig.2.25, and the morphologies of sample after pretreated in an atmosphere of 5%H_2-95%N_2 are shown in Fig.2.26.

SEM image on air-pretreated Mn–Co oxide coating on AISI430 shows that there were several crystals of micron-scale oxide scattering on the surface. Cross section image shows that the thickness of oxide scale was ~5.0 μm. XRD pattern shows that there were two phases of Cr_2O_3 and $(Cr,Mn,Co)_3O_4$ existing in the oxide coating which was pretreated in air. According to BSE images and EDX line scan results, chromium was distributed within the entire oxide layer. Therefore, Mn–Co oxide coating which was pretreated at 800 °C in air for 10 h was not able to protect the Cr outward diffusion in oxidation for AISI 430 substrates.

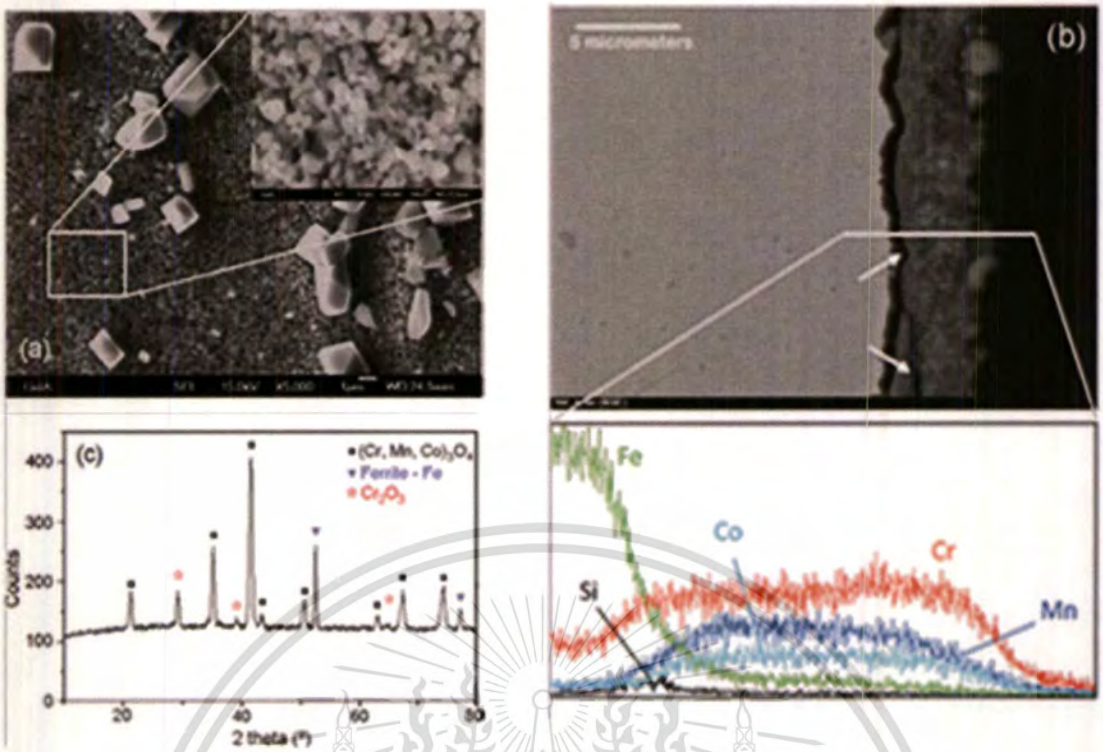

Figure 2.25: Morphology, chemistry and crystal structure of the Mn–Co oxide coating sample after pretreated in air. (a) SEM image on surface (b) cross-section image and EDX line scan (c) XRD pattern [25].

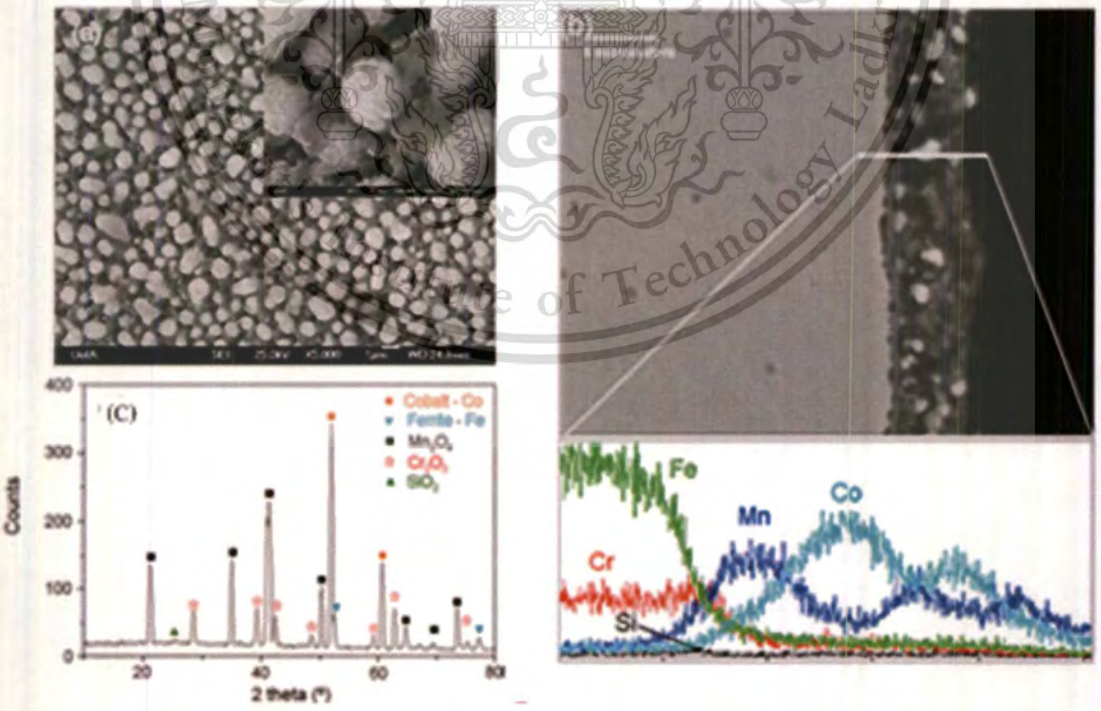

Figure 2.26: Morphology, chemistry and crystal structure of the Mn–Co oxide coating sample after pretreated in 5% H_2–95% N_2. (a) SEM image on surface (b) cross-section image and EDX line scan (c) XRD pattern [25].

Mn–Co oxide coating pretreated at 800 °C for 10 h in an atmosphere of 5% H_2–95% N_2 could be found as white micron-scale particles embedded in a grey matrix. EDX line scan shows that the white particles and grey matrix were Co-rich and Mn-rich, respectively. The XRD pattern shows that there were Co, Mn_3O_4, Cr_2O_3 and SiO_2 phases on the Mn-Co oxide coating which was annealed in the 5%H_2–95%N_2 atmosphere.

After pretreated, the samples were oxidized for 500 h in air at 800 °C. The morphologies of samples after oxidation are shown in Figs.2.27 and 2.28. They found that the air pretreated Mn–Co oxide coating sample had chromia and Mn-Co spinel phases existing in the coatings. For the 5%H_2–95%N_2 pretreated Mn–Co oxide coating sample, chromium from the AISI 430 stainless steel substrate was observed in the Mn–Co oxide coating layer, but Cr content in the 5%H_2–95%N_2 pretreated sample was much lower than that in the air-pretreated sample, and Cr was not detected on the coating surface. Therefore, the 5%H_2–95%N_2 pretreated Mn–Co oxide coating sample could reduce Cr outward diffusion when compared with the air pretreated oxide coating sample. However, Cr from the AISI 430 stainless steel substrates could still diffuse into the Mn–Co spinel coating layer during long-term oxidation.

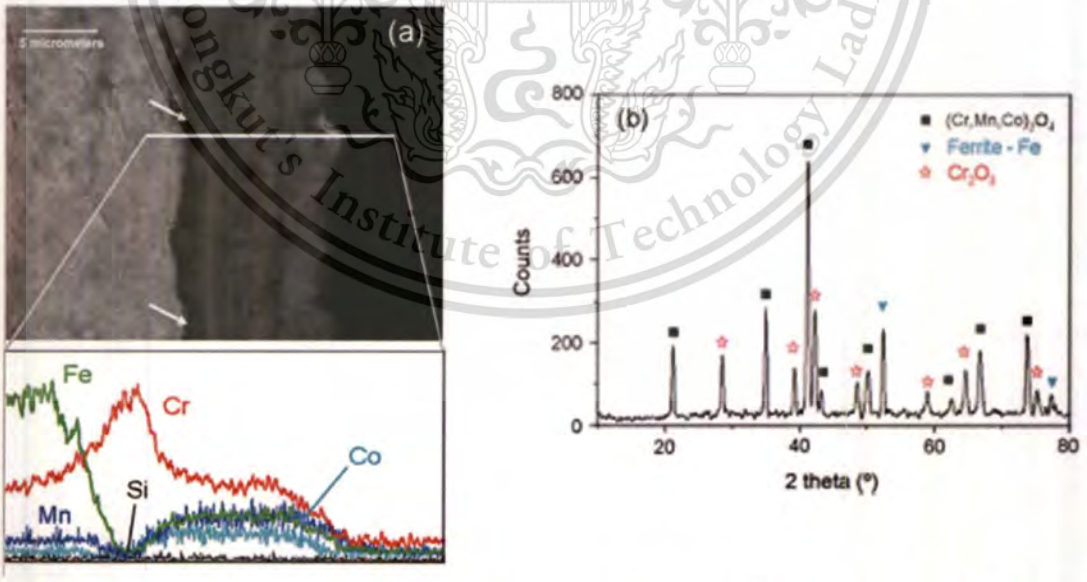

Figure 2.27: Morphology, chemistry and crystal structure of the air-pretreated Mn–Co oxide coating samples after oxidation for 500 h in air at 800 °C. (a) Cross-section image and EDX line scan (b) XRD patterns [25].

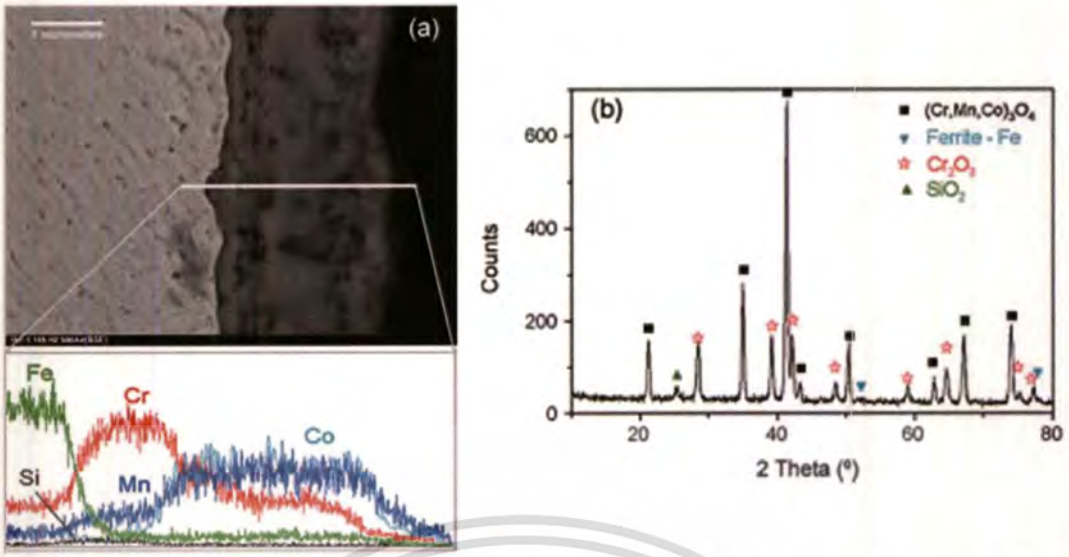

Figure 2.28: Morphology, chemistry and crystal structure of the 5%H_2–95%N_2 pretreated Mn–Co oxide coating samples after oxidation for 500 h in air at 800 °C. (a) cross-section image and EDX line scan and (b) XRD patterns [25]

Persson et al. [13] studied the oxidation behavior of six different coatings on Crofer 22 APU compared to the uncoated sample. The slurry of coatings which consisted of Al_2O_3, ZrO_2, LSC, LSM, Co_3O_4 and $MnCo_2O_4$ were coated on both sides of sample using a hand held spray-gun. The experiment was carried out at 900 °C in 1%H_2O-99%air at a flow rate of approximately 72 × 10^{-3} m^3/h. The samples were oxidized in 250-h cycles at 900 °C. The heating and cooling ramps were set to 120 °C/h. The total accumulated oxidation time was 4000 h. In oxidation time, the six different coating samples were removed from the furnace after 500, 1000, 2000 and 4000 h of oxidation. After that the samples were analyzed by focused ion beam (FIB)/transmission electron microscope (TEM). The weight gains per area of samples after oxidation are shown in Fig.2.29. They found that most of coatings were able to reduce the oxidation rate of Crofer 22APU as seen from the weight gains per area for each sample which was lower than that of uncoated sample except the $MnCo_2O_4$ coated sample. The slope of weight gain per area versus time of uncoated sample and the samples coated with LSM, Co_3O_4, and $MnCo_2O_4$ were linear up to 1000 h of oxidation. After that, the weight gains per area of the uncoated and $MnCo_2O_4$ coated samples were enormous while the weight gains per area of the LSM and Co_3O_4 coated samples continue linear up to 4000 h of oxidation. In order to compare with

this research, only LSM, Co_3O_4 and $MnCo_2O_4$ coating samples which have the coating thickness of 15 μm are considered. The parabolic rate constant and the scale thickness of samples after 500 h oxidation measured on BSE images are shown in Table.2.5.

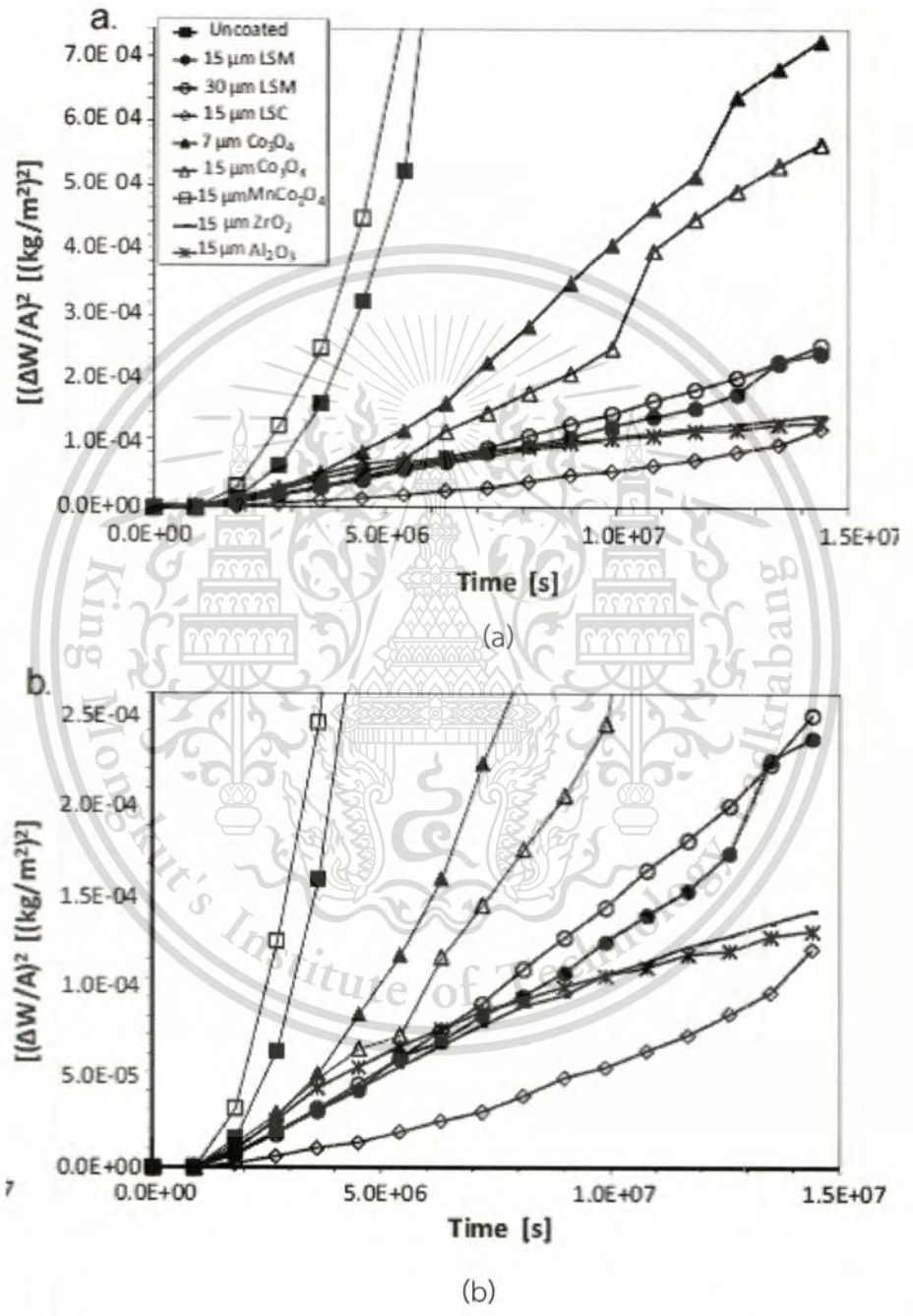

Figure 2.29: The weight gain per area versus time of uncoated and coated Crofer 22APU samples in the long-term, cyclic oxidation experiment carried out at 900 °C in air containing 1% water vapor. (a) overview (b) enlargement of Fig.2.29a for relatively small weight increase [13].

Table 2.5 Parabolic rate constant and the scale thickness of samples after oxidation at 900 °C in air containing 1% water vapor for 500 h [13].

Samples	k_p ($kg^2\ m^{-4}\ s^{-1}$)	time (h)	Scale thickness (μm)
Uncoated	$(8.2\pm2.5)\times10^{-11}$	1000	9.8 ± 3.2[a]
LSM coating	$(1.4\pm0.2)\times 10^{-11}$	4000	4.7 ± 1.6[a]
Co_3O_4 coating	$(1.7\pm0.6)\times 10^{-11}$ 4.4×10^{-11}	2750 3000–4000	5.6 ± 1.6 (10.6 ± 2.0)[b]
$MnCo_2O_4$ coating	$(9.4\pm1.5)\times10^{-11}$	1250	8.5 ± 1.0 (15.5 ± 1.4)[b]

[a] Total Newly formed Oxide Scale Cr_2O_3 scale

[b] Cr_2O_3 scale (Newly formed oxide + the sintered/reacted coating)

The cross section images of each sample are shown in Fig.2.30.

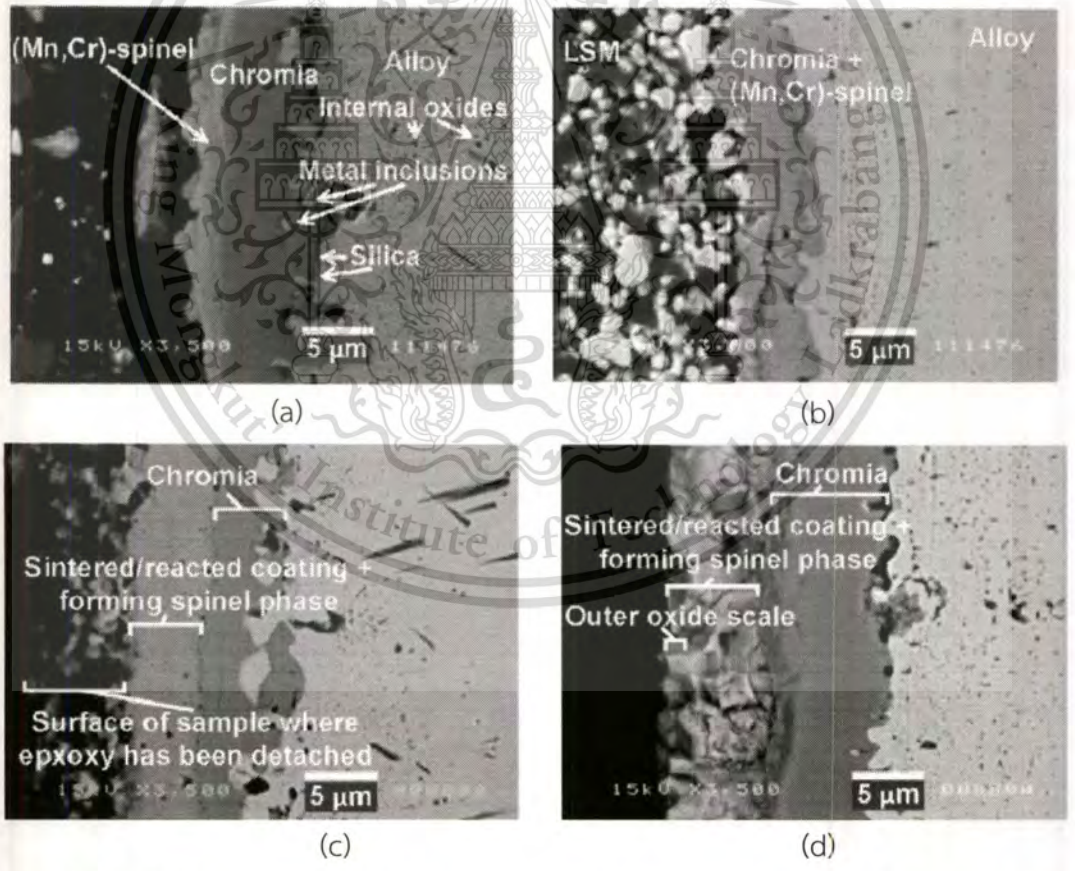

Figure 2.30: SEM images of the scales in the cross-sections of the samples. (a) uncoated Crofer22 (b) LSM coated on Crofer22 (c) Co_3O_4 coated on Crofer22 (d) $MnCo_2O_4$ coated on Crofer22 [13].

They found that after oxidation, the oxide scale forming on uncoated Crofer (Fig.2.30a) was found as two layers where the outer (Mn,Cr)-spinel phase layer was gray and brighter than the inner Cr_2O_3 phase layer. Metallic inclusions (light spots) were observed in the oxide scale. Internal oxides (black spots) consisted of TiO_2 and Al_2O_3 and were observed on all the coated samples. On LSM coated sample (Fig.2.30b), the oxide scale was thinner and had fewer metal inclusions than on the uncoated samples. The bright LSM particles appeared on oxide scale and were not incorporated into the oxide scale. On the Co_3O_4 coated samples after oxidation (Fig.2.30c), the oxide scale consisted of a Cr_2O_3 layer (darker layer on the SEM images) and a spinel phase layer (the lighter grey layer). The spinel phase layer consisted of the sintered/reacted Co_3O_4 coating. From cross section image of the $MnCo_2O_4$ coated samples in Fig.2.30d, it was found that the scale showed similar layers of a Cr_2O_3 layer and a spinel phase as found on the Co_3O_4 coated samples. Moreover, the $MnCo_2O_4$ coated samples also had the thickest oxide scale compared with all oxidized samples. The schematics of diffusion during the oxidation and oxide layer are shown in Fig.2.31.

They also demonstrated that on the uncoated Crofer alloy, the counter diffusion of Cr-cations and O-anions resulted in the formation of chromia scale. The presence and growth of (Cr, Mn)-spinel on uncoated samples could be explained by diffusion of Mn species through the chromia layer that Mn diffused faster than Cr, as shows in Fig.2.29a. For LSM coated alloy, Fig.2.29b, the coating was porous. The LSM coating which contained Mn>10%, at atmospheric pressure at 900 °C would existed as Mn_2O_3 particles. The $(La_{0.85}Sr_{0.15})MnO_3$ perovskite was stable under these conditions. At the LSM coating/$(Mn,Cr)_3O_4$ interface, the oxide scale also reacted with the LSM coating. The possible reactions were presented as

$$6(Mn_2O_3) + 12(MnCr_2O_4) \longrightarrow 16(Mn_{1.5}Cr_{1.5}O_4) + O_2(0.21\ atm) \qquad \Delta G = -163.8\ kJ \tag{2.5}$$

$$40(La_{0.85}Sr_{0.15})MnO_3 + 40MnCr_2O_4 + 3O_2(0.21\ atm) \longrightarrow 34LaCrO_3 + 6SrCrO_4 + 40CrMn_2O_4 \qquad \Delta G = 436.3\ kJ \tag{2.6}$$

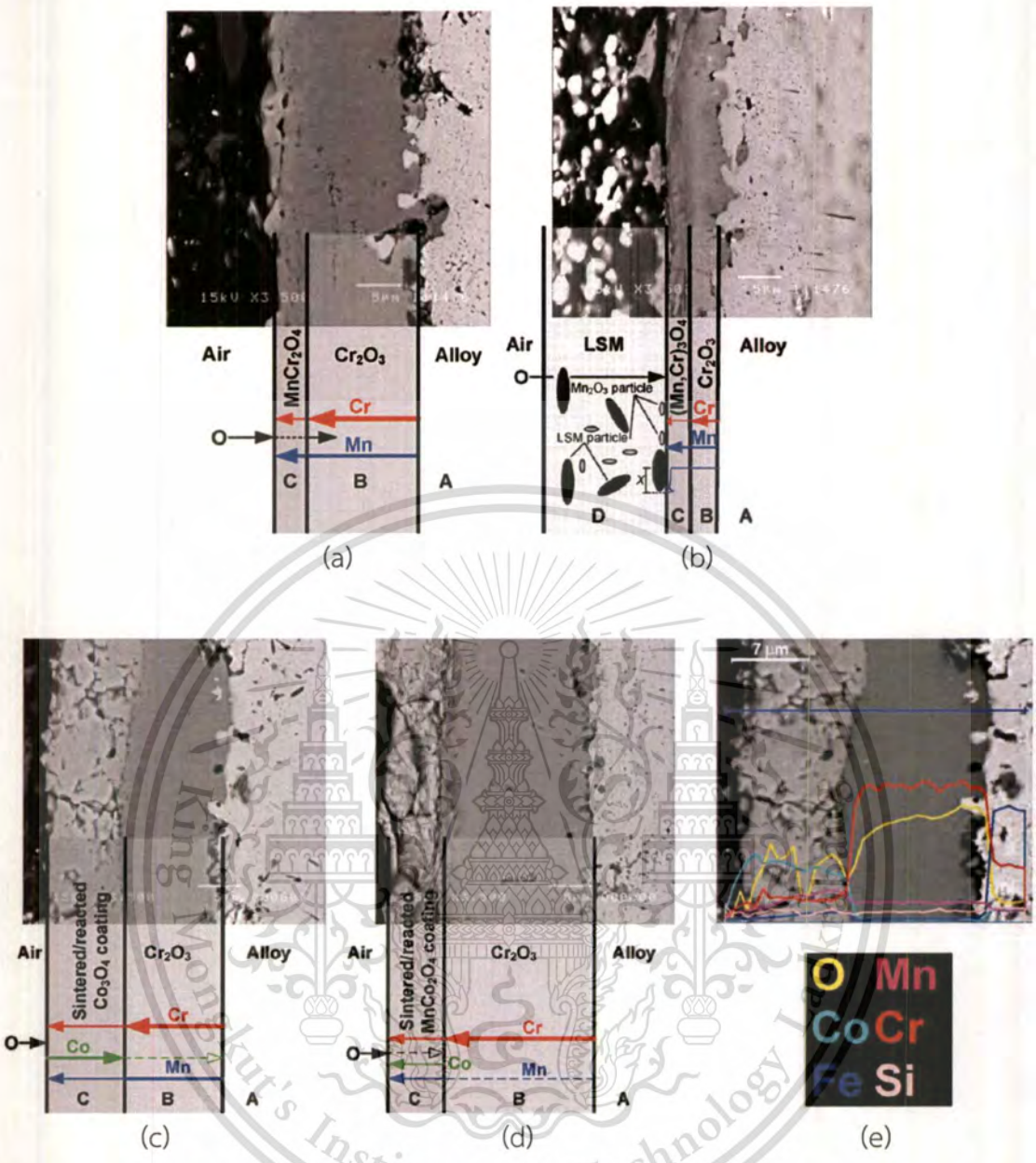

Figure 2.31: Diffusion model of ions during oxidation at 900 °C in air containing 1% water vapor on SEM images of samples oxidized for 2,000 h. (a) uncoated Crofer (b) LSM coated Crofer (c) Co_3O_4 coated Crofer (d) $MnCo_2O_4$ coated Crofer (e) line scan across the oxide scale and sintered/reacted Co_3O_4 coating [13].

According to the Co_3O_4 coated samples, as seen in Fig.2.29c, the coating was able to reduce the oxidation rate of Crofer 22 compared to the uncoated sample. The spinel coating could react with outwardly diffusing Cr- and Mn-cations. In spinel layer, the scale consisted of the formed spinel and the sintered/reacted residues of the Co_3O_4 coating. EDS analysis, Fig.2.29e, showed concentration profile that

Co cations might inward diffusion into the chromia phase. For the $MnCo_2O_4$ coated sample, parabolic oxidation rate behaved like the uncoated sample. The scale forming consisted of sintered/reacted coating and chromia scale as same as scale occurring on Co_3O_4 coating sample. The diffusion of ions on oxidation of the $MnCo_2O_4$ coated sample is presented in Fig.2.29d.

Chapter 3
Experimental

3.1 Sample preparation

Metallic material studied in this project is FeCoNi alloy developed by ArcelorMittal IMPHY. The samples were coated by two methods, the first one is cathodic sputtering (physical vapor deposition: PVD coating) and the other is slurry application (SA coating). The chemical compositions of the coatings are shown in Table 3.1. Five types of coated samples are shown in Table 3.2.

Table 3.1 The chemical compositions of the coatings.

The chemical compositions of the coatings.	Structure
$La_{0.8}Sr_{0.2}MnO_3$ (lanthanum-strontium manganite, LSM)	Perovskite
$La(Ni_{0.6}Fe_{0.4})O_3$ (lanthanum nickelate-ferrate, LNF)	Perovskite
Co_3O_4 (tri-cobalt tetroxide)	Spinel
$MnCo_2O_4$ (manganese cobaltite)	Spinel

Table 3.2 The coated samples in this study.

	LSM	LNF	Co_3O_4	$MnCo_2O_4$
SA method	✓	✓	-	-
PVD method	-	✓	✓	✓

3.2 Experimental setup

In this research, the samples were studied in four parts. The first part was studied about oxidation kinetic using a thermobalance. The second part was studied about morphology of samples after oxidation for long time in a horizontal furnace. The third part was studied the scale forming various time. The last part was studied on the hardness of coating by Vickers hardness test.

3.2.1 Oxidation kinetics test

The size of samples for studying oxidation kinetic using the thermobalance is approximately 10x10x1 mm^3. Before putting the samples into the furnace, exact size and weight of samples were measured. Then the uncoated samples were cleaned by acetone and ethanol using an ultrasonic cleaner while the coated samples were cleaned by nitrogen gas spray.

The samples were placed in the thermobalance (electronic balance B.70-Ugine Eyraud thermoscale) which was a vertical furnace as shown in Fig. 3.1. After that the experiment was carried out in O_2-5%H_2O at 800 ^{o}C (anodic atmosphere of HTE) at a total flow rate of 10 L/h. The weight gain per area was recorded every 5 minutes for 90 h. The samples were cooled down in the thermobalance after finishing experiment.

Figure 3.1: Electronic balance B.70-Ugine Eyraud thermoscale.

3.2.2 Morphology test

Samples with the size of 20x20x1 mm^3 were placed in a horizontal furnace for studying morphologies. Before putting the samples into the furnace, accurate size and weight of the samples were measured, and then the uncoated samples were cleaned by acetone and ethanol using an ultrasonic cleaner while the coated samples were cleaned by nitrogen gas spray.

The oxidation experimental setup is shown in Fig. 3.2. Both coated and uncoated samples were placed into a horizontal furnace which O_2-5%H_2O flew through at 800 ^{o}C at a total flow rate of 10 L/h for 500 h. After finishing the experiment, the oxidized samples were removed from the furnace and weight gains of the samples were measured.

Figure 3.2: Oxidation experimental set.

After finishing the experiments, the surface and cross section images were obtained from scanning electron microscope (SEM). Elemental analysis of the surfaces and cross sections of the samples were measured by energy dispersive spectroscopy (EDS). The EDS data provide only elemental distribution, thus phase composition cannot be definitively determined. However, it is possible to use X-ray diffraction technique (XRD) to identify atomic structure of the scale occurring on the sample surface. The surface was scanned by XRD over the range of 20-60 degree 2θ, with resolution 0.1 degree 2θ and scan speed 1.0 degree/min. Peaks obtained from XRD results were compared with Joint Committee on Power Diffraction Standards (JCPDS) to identify the phases presented.

3.2.3 Scale forming test

The scale forming is tested on uncoated FeCoNi samples. After oxidation in O_2-5%H_2O at 800 ^{o}C in thermobalance or in horizontal furnace, samples were analyzed to find the atomic structure of scale by XRD. The scale forming was tested in various oxidation times of 1 min, 5 min, 15 min, 1 h, 16 h, 72 h, 96 h, 455 h and 500 h.

3.2.4 The hardness of the coating samples test

Vickers hardness test was used to study the hardness of coating on the coated samples. In order to do the Vickers hardness test, the coated samples were indented with a diamond indenter, in the form of a right pyramid with a square base and an angle of 136 degree between opposite faces subjected to various loads of 5, 10, 20, 50, 100, 150, 187.5 and 250 kgf. The full load was applied for 10 seconds. The two diagonals of the indentation left in the surface of the sample after removal of the load were measured using SEM. Mean diagonal length and load were used to calculate the Vickers hardness in SI unit.

Chapter 4

Results and Discussion

In this chapter, results and discussion are reported in four sections. The first one is oxidation kinetics of samples, the second one is the morphology of samples after oxidation for long time, the scale forming of uncoated FeCoNi alloy after oxidation at various times is studied in the third part, and the last part focuses on the hardness of coating without oxidation.

4.1 Oxidation kinetics

The samples in this study are uncoated-FeCoNi, LNF-SA-FeCoNi and LNF-PVD-FeCoNi. The results of samples which were oxidized in O_2-5%H_2O at 800 °C using thermobalance were presented via the relation between weight gain per unit area of the samples and time for oxidation period up to 90 h, as in Fig.4.1.

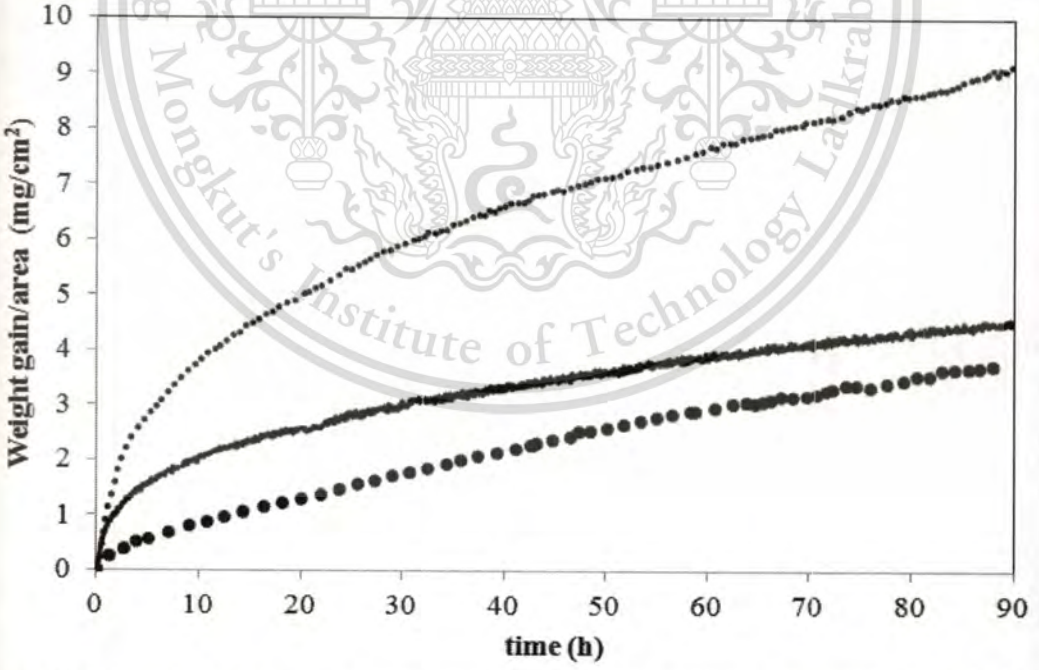

Figure 4.1: Weight gains per area versus times of samples oxidized at 800 °C in O_2-5%H_2O at a total flow rate of 10 L/h. (····Uncoated-FeCoNi, —LNF-SA-FeCoNi, ••••LNF-PVD-FeCoNi sample)

Experimental results showed that all oxidation rates in terms of weight gain per unit area with time obey parabolic rate law as in Equation 4.1.

$$w^2 = k_p \times t \quad (4.1)$$

Where w = weight gain per unit area (mg/cm^2),

t = time of oxidation (h),

k_p = parabolic rate constant ($mg^2/cm^4/h$).

From the graph in Fig.4.1 the parabolic rate constant is able to calculate as shown in Table 4.1

Table 4.1 Parabolic rate constant of the samples oxidized at 800 °C in O_2-5%H_2O at a total flow rate of 10 L/h.

FeCoNi alloy	Parabolic rate constant, k_p ($mg^2/cm^4/h$)	R^2
Uncoated	0.85	0.9933
LNF-SA	0.21	0.9904
LNF-PVD	0.17	0.9861

It can be seen that the parabolic rate constants of coated samples are around 4 times lower than that of the uncoated one. This means that coating can reduced oxidation rate of FeCoNi. Comparing the parabolic rate constant of LNF-SA with LNF-PVD samples, it can be observed that the parabolic rate constant of PVD sample was slightly lower than SA sample. This means that PVD coating should better reduce oxidation of FeCoNi than SA coating.

After the oxidation in the furnace for 500 h for uncoated sample and for 455 h for coated samples in O_2-5%H_2O at 800 °C at a total flow rate of 10 L/h, the weight gain of the samples were measured. The weight gains per area from experiment and from calculation are presented in Table 4.2

From Table 4.2, the weight gains per area obtain from the experiment and calculation are in the same order of magnitude. The weight gain per area of uncoated sample obtained from the experiment is around 13 % lower than that from the calculation. In the case of coated samples, the weight gains per area of

coated sample obtained from experiment are about 50% more than that from calculation.

Table 4.2 Weight gain per area of the samples after oxidation for 500 h (uncoated sample) and for 455 h (coated sample) at 800 °C in O_2-5%H_2O at a total flow rate of 10 L/h.

Sample	Weight gain/area (mg/cm^2)	
	Experiment	Calculation
Uncoated-FeCoNi(500 h)	17.91	20.62
LNF-SA-FeCoNi (455 h)	13.94	9.77
LNF-PVD-FeCoNi (455 h)	13.81	8.79

4.2 Morphology

In this section, the morphology of uncoated and five coated samples after oxidation at 800 °C in O_2-5%H_2O at a total flow rate of 10 L/h for long time in the horizontal furnace was mentioned. After oxidation, the samples were analyzed. The high magnification images of samples were obtained from SEM. The elemental distribution on surface and cross section were obtained from EDS analysis. XRD was used to find the atomic structure of the scale.

4.2.1 Uncoated FeCoNi

After oxidation for 500 h at 800 °C in O_2-5%H_2O at a total flow rate of 10 L/h, the mean weight gain of uncoated sample was 17.91 mg/cm^2. The oxidized sample was analyzed by SEM/EDS and XRD. Fig. 4.2 shows SEM images of the uncoated sample. It can be seen from the SEM images that there are three different morphologies appearing on the surface. The three different morphologies which are found on the surface are big grains, small grains and plates. The elemental analysis by EDS was carried out on the surface. The EDS results indicated that Fe, Co and O distributed on overall surface.

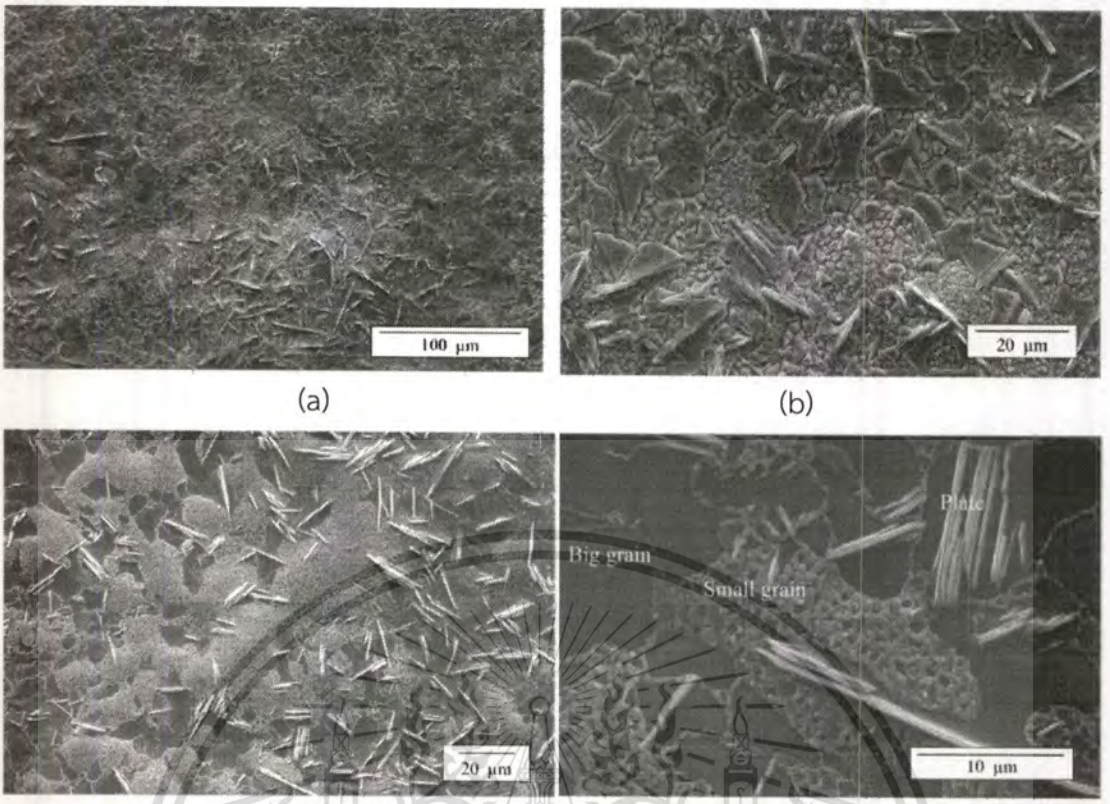

Figure 4.2: SEM images of the surface of uncoated sample after oxidation at 800 °C in O_2-5%H_2O at a total flow rate of 10 L/h for 500 h.

Before the oxidation of uncoated FeCoNi alloy, there are only 2 peaks of cubic of FeCoNi alloy appearing on the XRD pattern. After the oxidation for 500 h at 800 °C in O_2-5%H_2O at a total flow rate of 10 L/h, other peaks appeared in the XRD pattern while the alloy substrate peaks disappeared in the XRD pattern, as in Fig.4.3. The XRD results were compared with JCPD standards to identify atomic structure of the scale. It can be found that these new peaks were probably the peaks of $CoFe_2O_4$ cubic. XRD result can also indicate that big grains, small grains and plates on the SEM images in Fig.4.2 were the same phase of cubic of $CoFe_2O_4$.

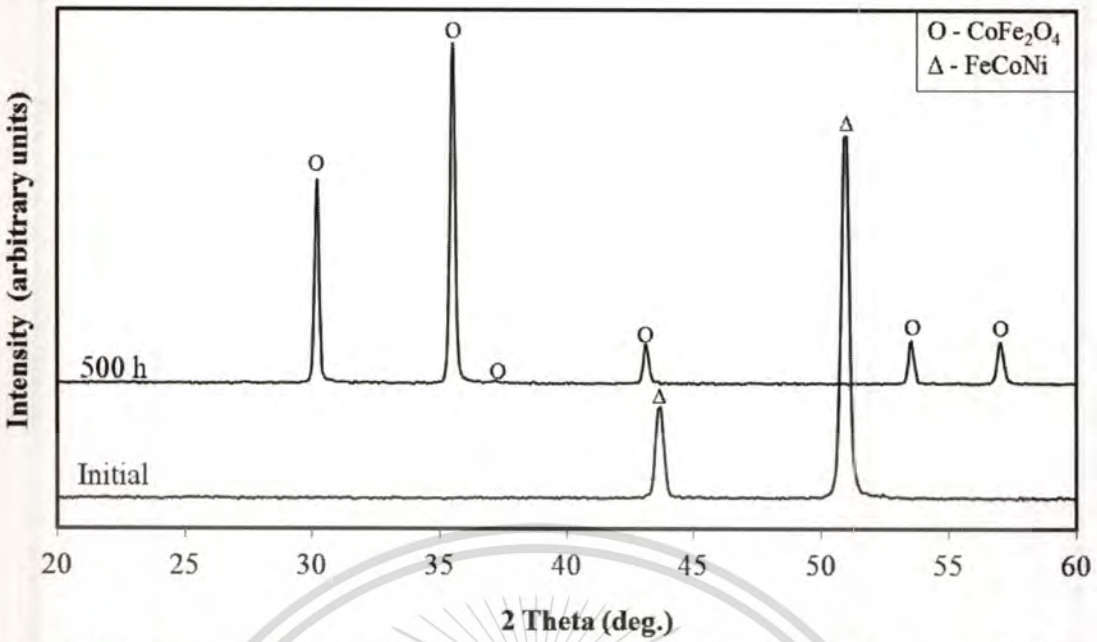

Figure 4.3: XRD results of uncoated sample before and after oxidation at 800 °C in O_2-5%H_2O at a total flow rate of 10 L/h for 500 h.

After XRD and SEM/EDS analysis on the surface, the uncoated sample was analyzed by SEM/EDS on cross section. The SEM images on cross section of the uncoated sample after oxidation at 800 °C in O_2-5%H_2O at a total flow rate of 10 L/h for 500 h are shown in Fig.4.4. It can be seen from the SEM images that the oxide scale with the thickness about 240 μm was observed on top of the alloy surface after oxidation. The thickness of scale about 97 μm was observed on the bottom of alloy surface. The difference of thickness was probably occurred because of the difference between the flowing of O_2-H_2O on the top side and bottom side. On the top side, the flow rate of O_2-H_2O was higher than the flow rate on the bottom side. Therefore the scale on the top side was more formed than on the bottom side. Moreover porous area at the interface and within oxide layer as undulation was observed. It can be clearly seen in Fig.4.4d that there are different colors existing in the scale. The different colors existing were indicated that there were different distributions of elements. In the scale, three different color layers were found. In the alloy layer, it can be seen that there were small black spots distributing in the bright background.

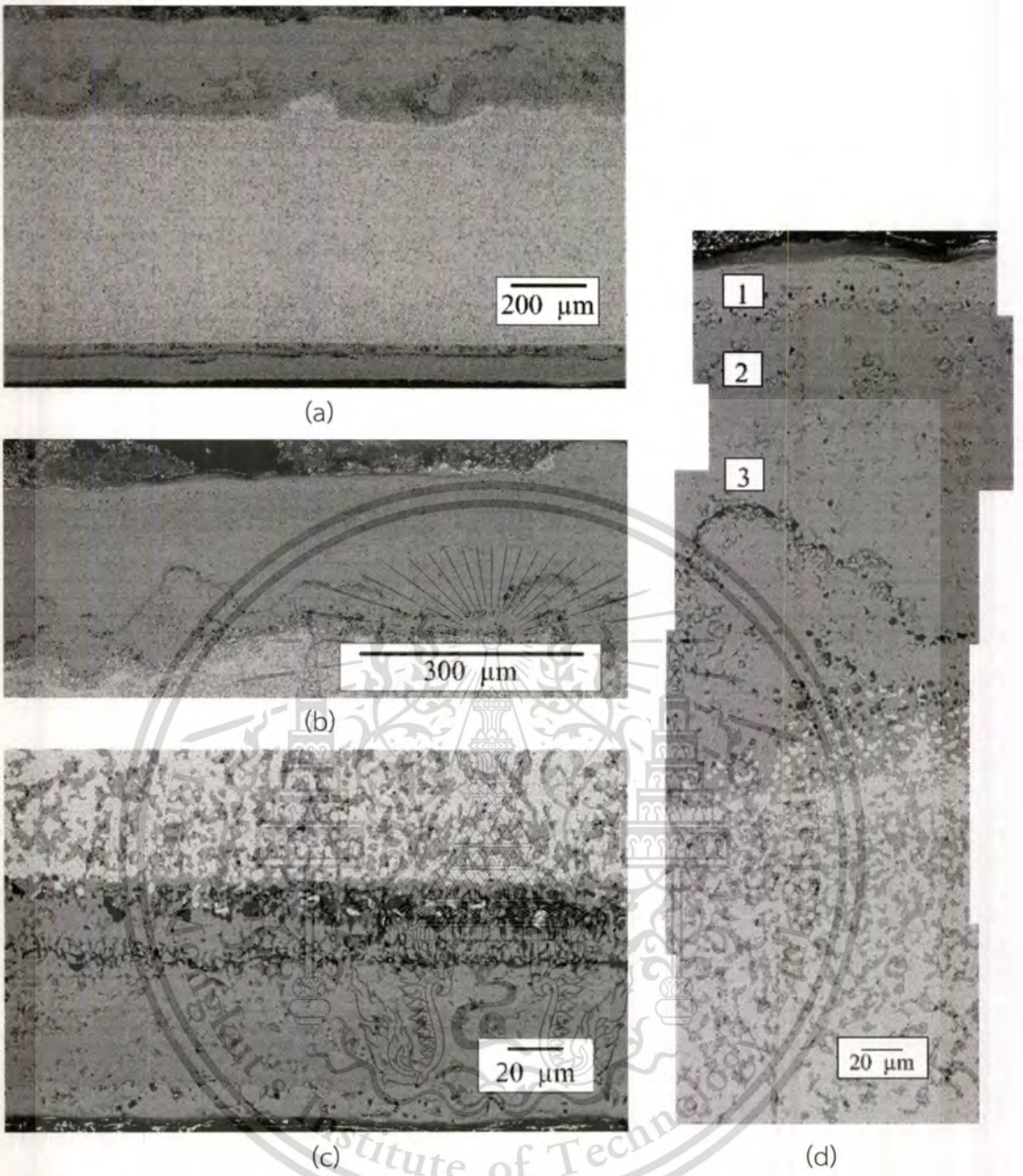

Figure 4.4: Cross sections images of the oxide scales formed on uncoated FeCoNi sample after oxidation at 800 °C in O_2-5%H_2O at a total flow rate of 10 L/h for 500 h. (a) Overall (b) scale occurring on top side (c) scale occurring on bottom side (d) enlargement of scale occurring on top side

In order to indicate the distribution of elements in the three different color layers which exist in the SEM images, chemical analysis by EDS was carried out on the top side from top of scale deeply to the metal, as in Appendix A-1. The EDS results show that the outermost layer (layer 1) which shows as the bright color layer in Fig.4.4d contained Fe, Co and O. This layer stayed at the first 25 µm from top

surface of scale. In the next layer (layer 2) of scale shown as the dark color layer in Fig.4.4d, was found at the depth about 25-60 μm from top surface. The EDS results show that a lot of Fe and O distribute in this layer. In the third layer, the bright color layer (layer 3) in Fig.4.4d which stayed at the depth about 60-240 μm from top scale contained high amount of Fe, Co, Ni and O. In the innermost layer of scale, the closer the alloy surface, the less amount of Co was detected. On the other hand, the closer the alloy surface, the more amount of Ni was detected. Moreover, at the interface there was high quantity of Ni detected while both Fe and O amounts appeared to be lower. At the bottom side, EDS analysis was used to confirm the element distribution on scale, as in Appendix A-2. The results show that the scale occurred in 3 layers as same as the top scale. At the metal layer, it is indicated that there was high amount of Ni detected at the light color while Fe and O was detected at the dark color spot. Therefore, the light color is the bulk of metal and the dark color which presented as small spots is oxide of Fe which occurred because of internal oxidation. This means that there is internal oxidation occurring in the metal layer as small precipitate oxides of Fe.

From the XRD result and EDS analysis of uncoated FeCoNi after oxidation at 800 $^{\circ}$C in O_2-5%H_2O at a total flow rate of 10 L/h for 500 h, it is able to conclude that the outermost scale layer (layer 1 in Fig.4.4d) is the layer of $CoFe_2O_4$ cubic. The second layer (layer 2 in Fig.4.4d) is possible to be the layer of rhombohedral phase of Fe_2O_3, and the innermost layer (layer 3 in Fig.4.4d) is possible to be the scale layer of $NiFe_2O_4$. Moreover, it was found that the internal oxidation occurred as small precipitated oxides of Fe all over the metal layer. This result agrees with recent report of the Chapman et al.[16] which reported the oxidation of ternary FeCoNi alloys in air at 800 $^{\circ}$C. The schematic diagrams of scale layer are shown in Fig.4.5.

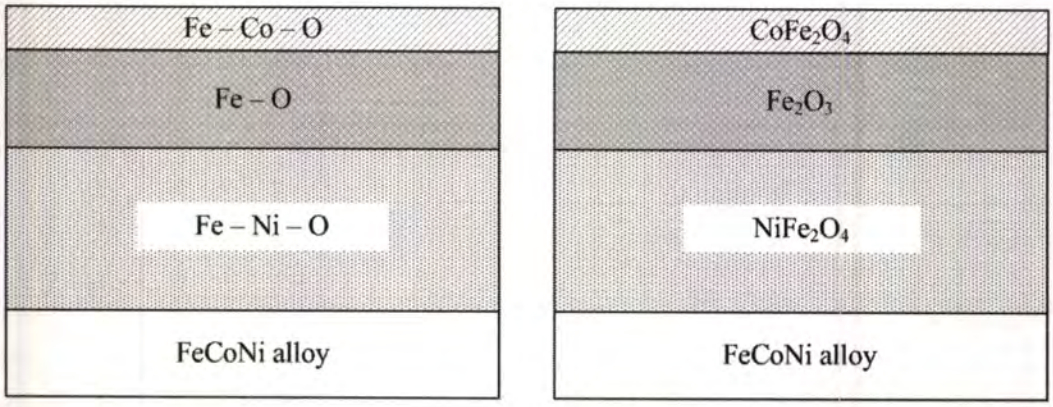

Figure 4.5: The schematic diagrams of scale layer of uncoated FeCoNi after oxidation at 800 °C in O_2-5%H_2O at a total flow rate of 10 L/h for 500 h.

In a solid oxide electrolytic cell, the thickness of interconnector of about 0.46 mm (460 μm) is desired. In this research, the scale thickness about 240 μm on uncoated FeCoNi sample after oxidation at 800 °C in O_2-5%H_2O at a total flow rate of 10 L/h for 500 h was found. The tendency of the scale thickness is increased with time. Therefore, the uncoated FeCoNi alloy is not suitable for using as an interconnector in a solid oxide electrolytic cell. Coating on alloy is one way for improving the oxidation resistance at high temperatures. In this research, five coated samples were studied. In the next topic, the morphology results of these samples after oxidation for long time are reported.

4.2.2 LSM-SA-FeCoNi

The mean weight gain of FeCoNi sample which was coated by $La_{0.8}Sr_{0.2}MnO_3$ perovskite by slurry application method (SA) after oxidation at 800 °C in O_2-5%H_2O at a total flow rate of 10 L/h for 455 h was 14.04 mg/cm^2. SEM images of oxidized LSM-SA sample are shown in Fig.4.6.

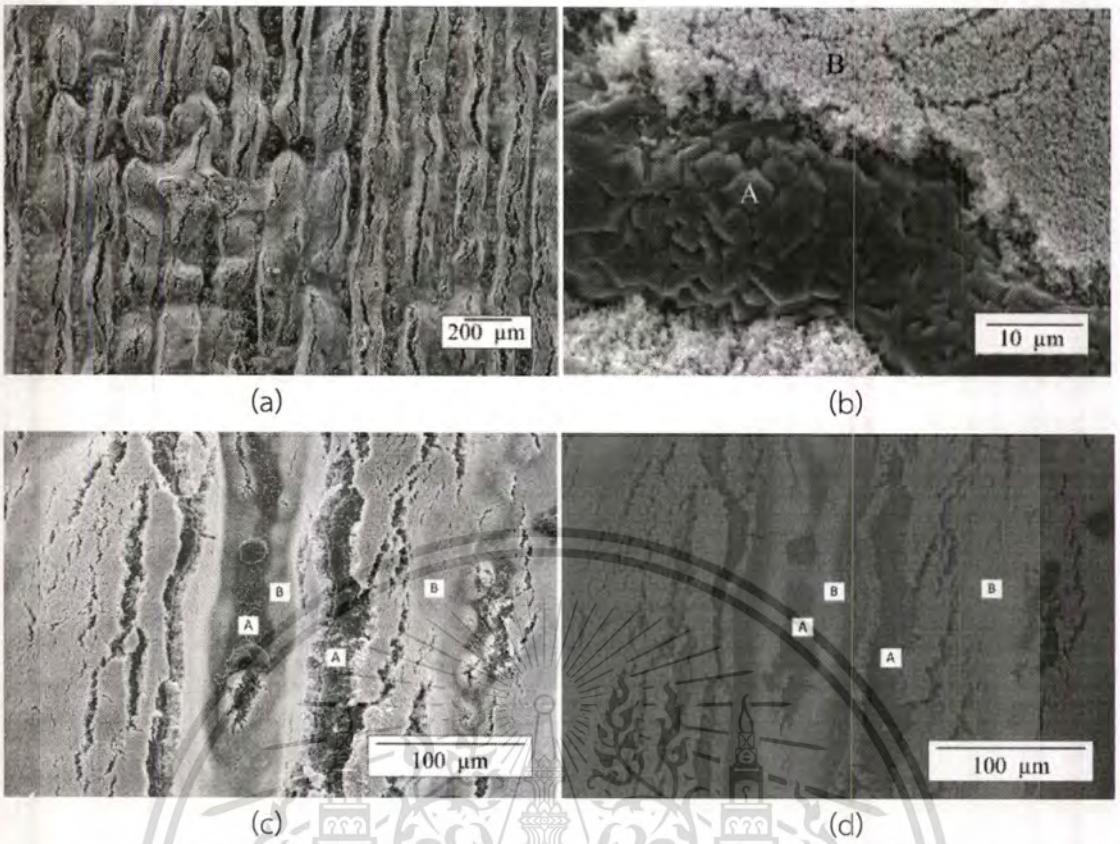

Figure 4.6: SEM images on surface of LSM-SA coated on FeCoNi alloy after oxidation at 800 °C in O_2-5%H_2O at a total flow rate of 10 L/h for 455 h.

It can be seen from Fig. 4.6a that the coating cracks all over the surface. On area A in Figs.4.6b, c and d, the morphology was found as big grains while the small grains were presented at area B. Results from EDS indicate that there are the appearance of La, Sr, Mn and O on the area B. It is possible that area B is the LSM coating. In addition Fe, Co and O were found on the area A. Therefore, the area A is possible to be the oxide.

According to the structure of the scale, before the oxidation, there was only the appearance of the peaks of $La_{0.8}Sr_{0.2}MnO_3$ which has perovskite structure on the XRD pattern. After the oxidation, initial peaks of coating still appeared on the XRD pattern and other peaks were also found. Compared with JCPD standard, new peaks which appeared on XRD pattern were possible to be the peaks of $CoFe_2O_4$ cubic. Therefore, there was two-phase appearance on the depths of within 5-10 µm from surface. Two-phase appearance is probably found because of the crack of the coating. It is possible that oxygen is able to diffuse through the coating into alloy,

and then FeCoNi alloy is oxidized. The scale was formed at the interface between coating and alloy. The formation of scale would push the LSM coating to be cracked.

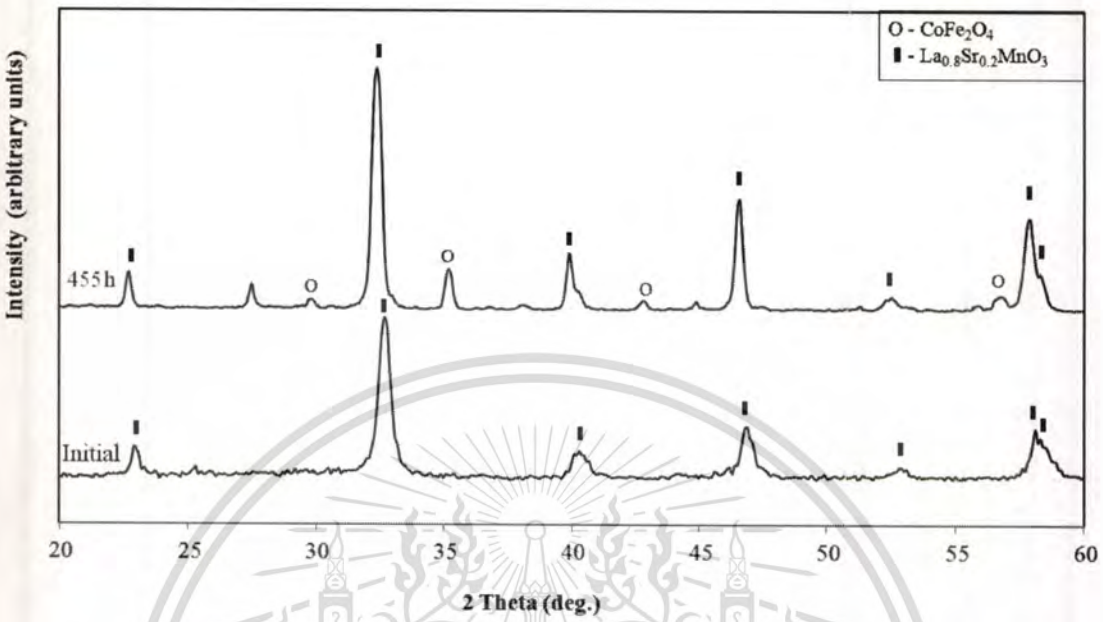

Figure 4.7: XRD results of LSM-SA coated on FeCoNi alloy after oxidation at 800 °C in O_2-5%H_2O at a total flow rate of 10 L/h for 455 h.

Cross section images of LSM-SA FeCoNi alloy after oxidation at 800 °C in O_2-5%H_2O at a total flow rate of 10 L/h for 455 h are shown in Fig.4.8. The total scale thickness is approximately 81 μm. The layer between scale and metal is not completely continuous. A big cavity is present in the scale layer, as clearly seen in Figs.4.8c and d. Moreover, there are pores distributing in the scale. It was found that there were different colors existing in the scale which referred to the distribution of elements. In the metal, two types of internal oxidation occurred. For the first one, the internal oxidation occurred as small precipitated oxides distributing in the area from the interface between scale and metal deep down to the metal for 100 μm. Under precipitated oxide area, internal oxidation occurred along grain boundaries, as clearly seen in Fig.4.8f.

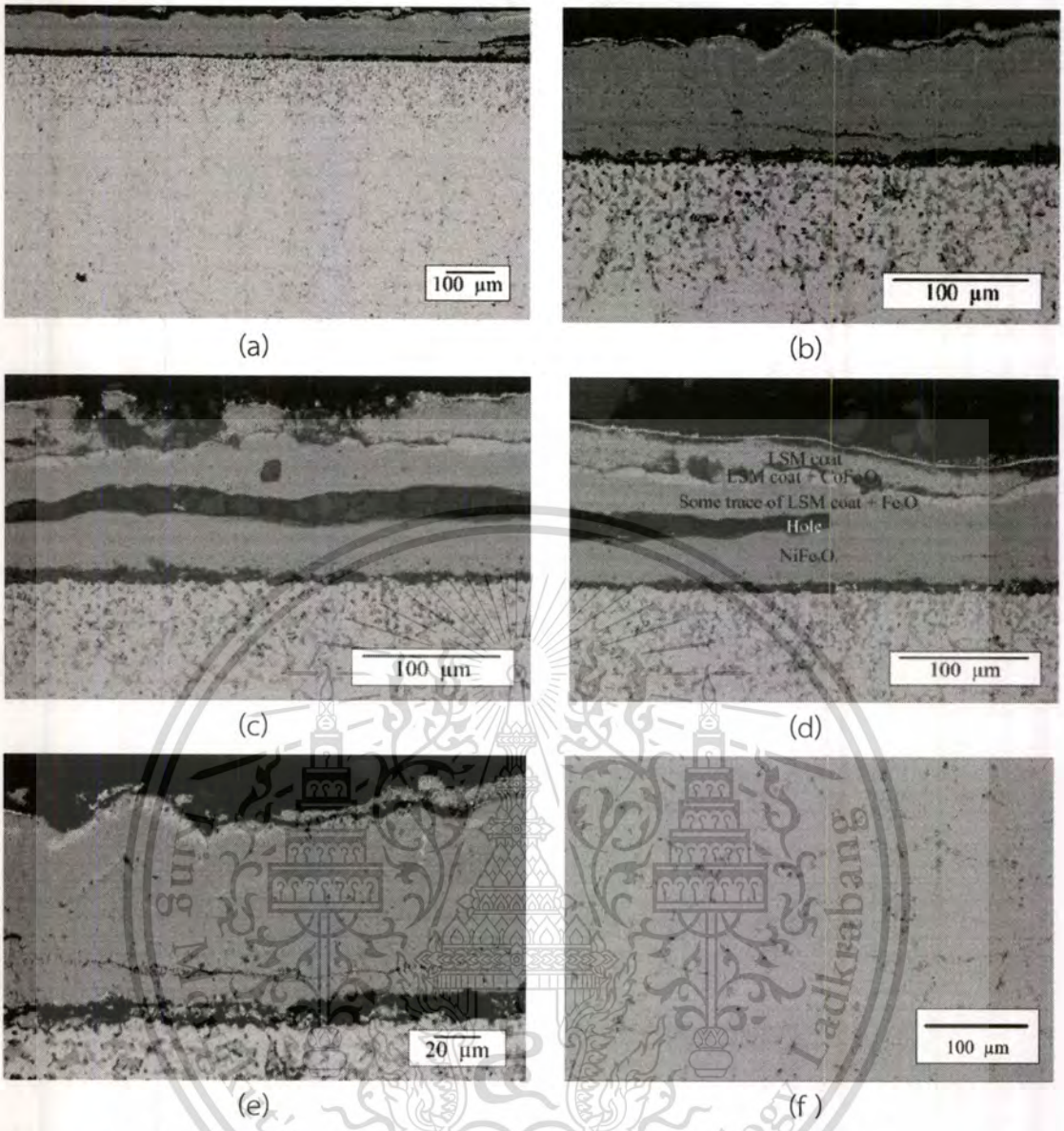

Figure 4.8: Cross sections images of LSM-SA coated on FeCoNi alloy after oxidation at 800 °C in O_2-5%H_2O at a total flow rate of 10 L/h for 455 h.

Chemical analysis by EDS was carried out from top of scale deeply to the metal for every 10 µm, as shown in Appendix A-3. The results show that at the metal layer, high amount of Ni was detected at the light color area, while Fe and O were detected at the dark color area. This means that the light color area is the bulk of alloy and the dark color area is the scale of Fe which occurred because of internal oxidation. It was found that Fe, Co, Ni and O on the scale layer were distributed to three layers. Three scale layers consist of $CoFe_2O_4$ at the outermost scale, Fe_2O_3 at the middle scale and $NiFe_2O_4$ at the innermost. Furthermore, the EDS results show that there are distribution of Si, Al, Ca and O in the cavity (in Figs.4.8c and d).

Focusing on LSM coating, most of composition of coating which consisted of La, Sr and Mn were found on the outermost of scale. The coating was not found on the entire surface, the coating was missing in some area, as clearly seen in Fig.4.8c. Moreover, La, Sr and Mn were also detected in the $CoFe_2O_4$ layer. Also traces of La, Sr and Mn were found at Fe_2O_3 layer and at the interface between Fe_2O_3 and $NiFe_2O_4$ layers in the form of white color lines observed in Fig.4.8e.

From the previous discussion, $CoFe_2O_4$, Fe_2O_3 and $NiFe_2O_4$ were still formed even the alloy was coated by LSM-SA. This means that LSM-SA coating cannot prevent the alloy from oxidation at high temperatures. The schematic diagrams of scale layers occurring in this case are shown in Fig 4.9.

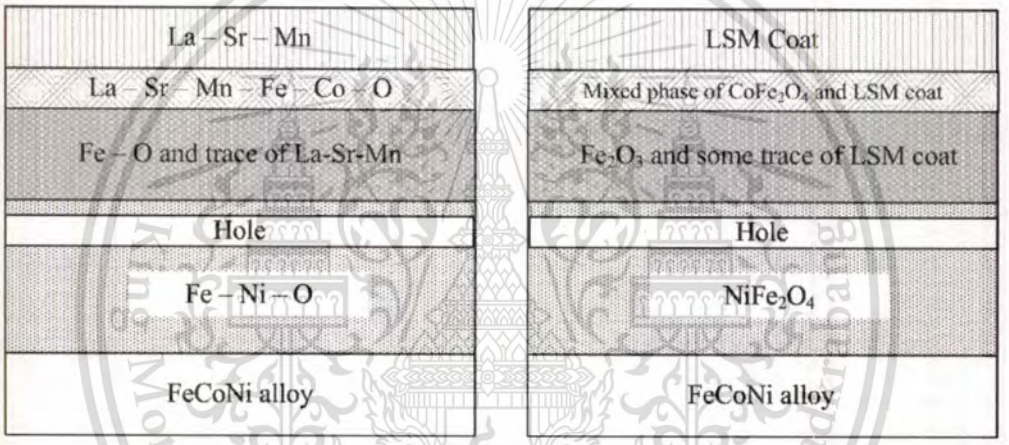

Figure 4.9: The schematic diagrams of scale layer of LSM-SA coated on FeCoNi alloy after oxidation at 800 °C in O_2-5%H_2O at a total flow rate of 10 L/h for 455 h.

4.2.3. LNF-SA-FeCoNi

After oxidation for 455 h in O_2-5%H_2O at a total flow rate of 10 L/h at 800 °C, the mean weight gain of FeCoNi alloy which was coated by $La(Ni_{0.6}Fe_{0.4})O_3$ perovskite by slurry application method (SA) was 13.94 mg/cm^2. The oxidized LNF-SA sample was analyzed by SEM/EDS and XRD. SEM images of LNF-SA sample are shown in Fig.4.10.

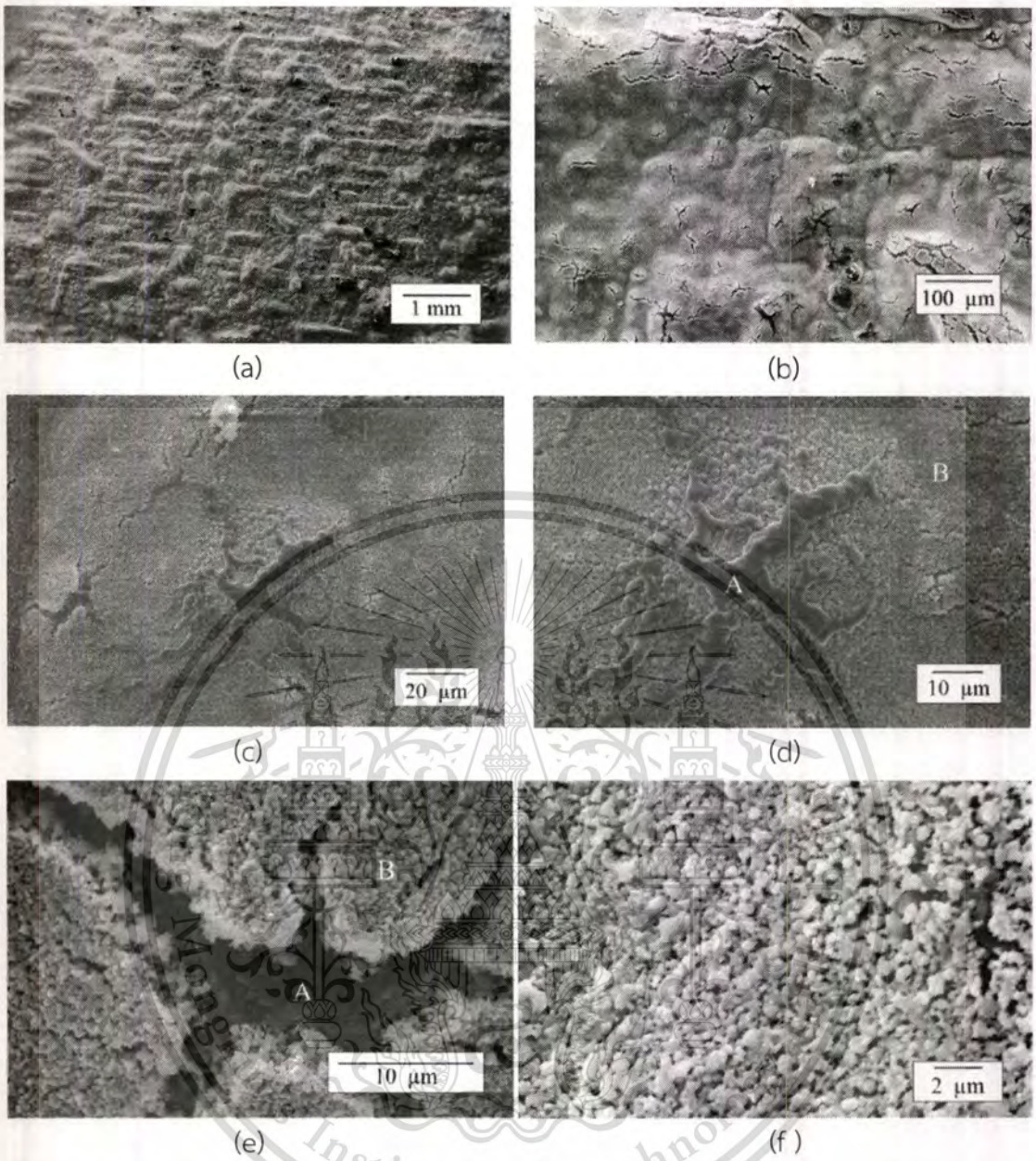

Figure 4.10: SEM images on surface of LNF-SA coated on FeCoNi alloy after oxidation at 800 °C in O_2-5%H_2O at a total flow rate of 10 L/h for 455 h.

It can be seen from the SEM images that there are a lot of crack of the coating appearing on the surface. The morphology in Figs.4.10d and e is found as big grains on area A while the small grains are found on area B. From Figs.4.10d and e, the EDS results indicate that there were Fe, Co and O distributing on the area A. In addition La, Ni, Fe and O were found on the area B. It is possible that area A could be the scale while area B could be the LNF coating

Before the oxidation, there are only peaks of substrate (LNF-FeCoNi) appearing on the XRD pattern, as shown in Fig.4.11. After the oxidation of LNF-SA

sample for 455 h in O_2-5%H_2O at 800 °C at a total flow rate of 10 L/h, there were substrate peaks appearing in the XRD pattern. Moreover, other peaks were found. It was reported from the JCPD standard that these other peaks were probably the peaks of cubic phase of $CoFe_2O_4$. Therefore, there was two-phase appearance on the depths of within 5-10 μm from surface. Two-phase appearance was probably found because of the crack of the coating. The crack of coating after oxidation probably occurred because oxygen could diffuses through the coating into alloy, and then FeCoNi alloy was oxidized. The scale was formed at the interface between coating and alloy. The formation of scale would push the coating to be cracked and hence the oxide of $CoFe_2O_4$ cubic was exposed.

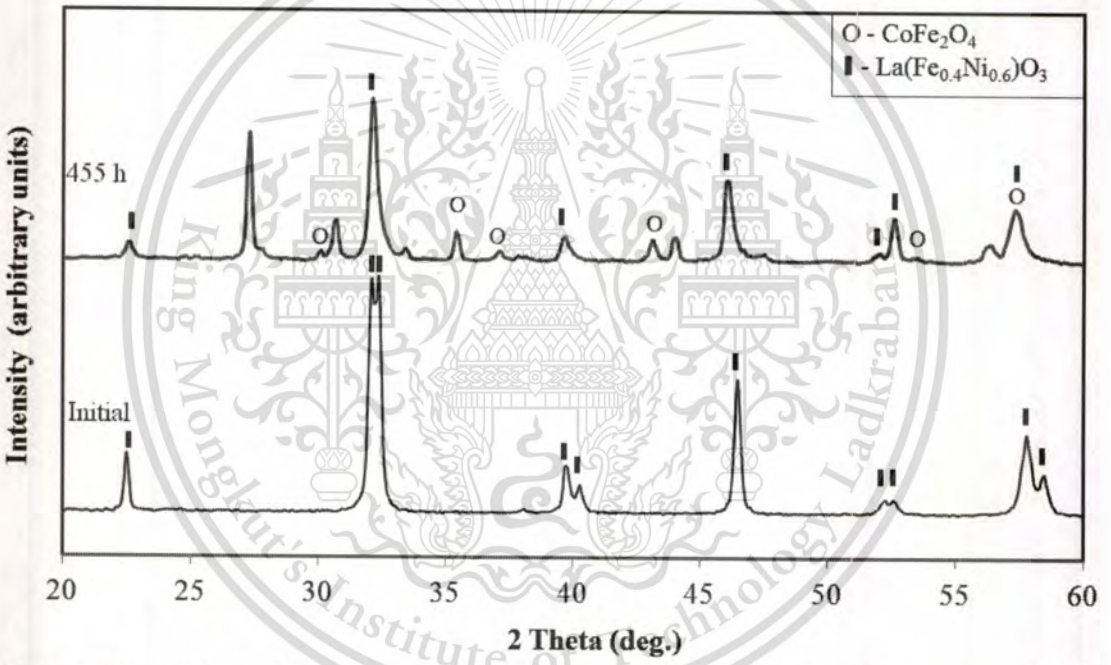

Figure 4.11: XRD results of LNF-SA coated on FeCoNi alloy after oxidation at 800 °C in O_2-5%H_2O at a total flow rate of 10 L/h for 455 h.

Cross section images from backscattered SEM of the oxide scales forming are shown in Fig.4.12.

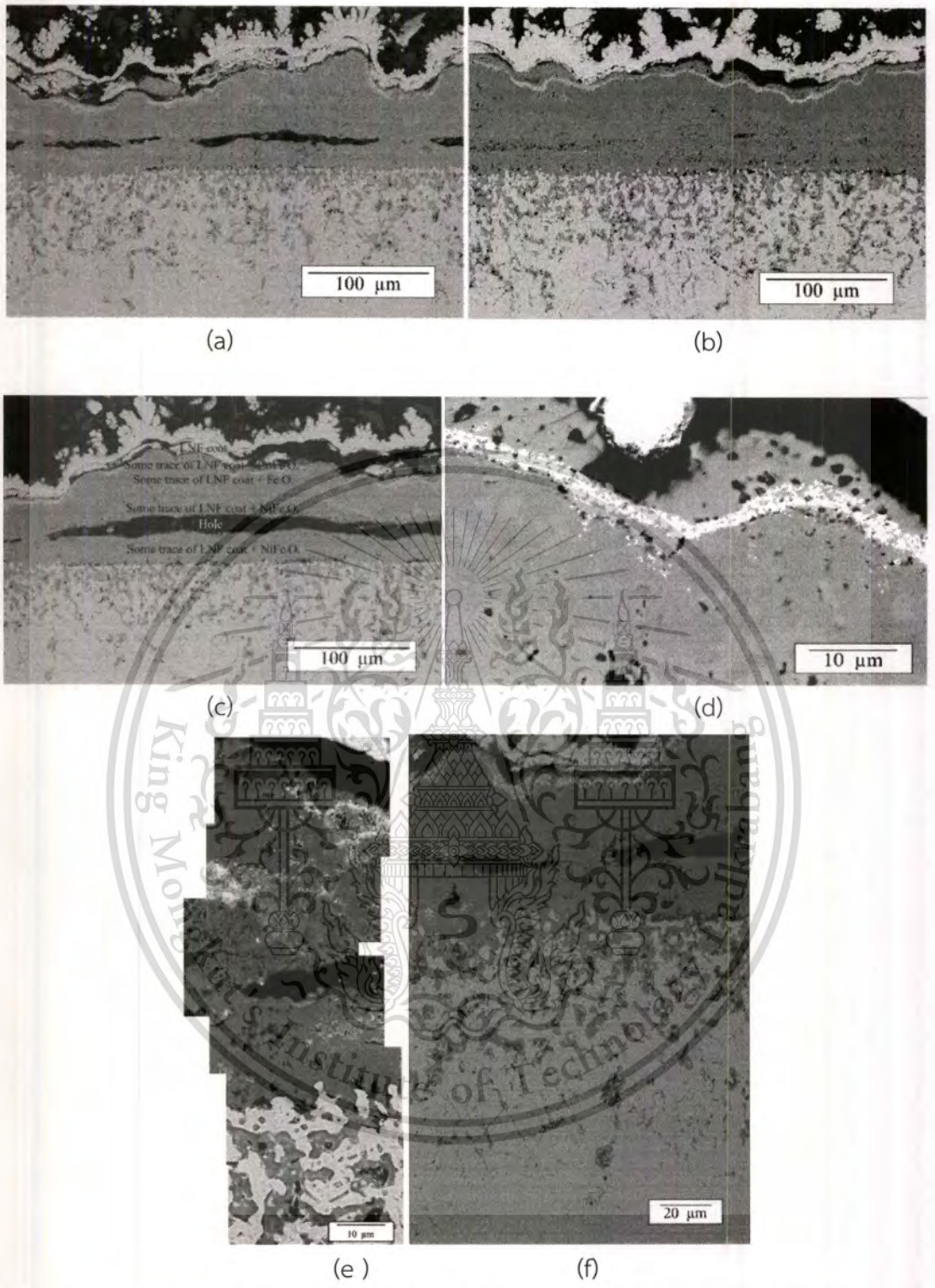

Figure 4.12: Cross sections images of LNF-SA coated on FeCoNi alloy after oxidation at 800 °C in O_2-5%H_2O at a total flow rate of 10 L/h for 455 h.

The oxide scale with the thickness about 68 µm was shown. It can be seen from the SEM images that there is undulation on the outermost of surface. The layer between scale and metal is not completely continuous. The big cavity in the scale

layer is presented as clearly seen in Figs.4.12a, c and e. Moreover, the pore distribution in the scale is observed. The different colors existing in the scale which refer to distribution of elements were found. In the alloy layer, internal oxidation as small precipitate oxides can be observed in the area from the interface between scale and metal deep down to the metal for 100 μm. In the area deeper than 100 μm, internal oxidation occurred along grain boundaries.

Chemical analysis by EDS was carried out from top of scale deeply to the metal every 10 μm, as shown in Appendix A-4. The results show that at the metal layer, high amount of Ni was detected at the light color area while Fe and O were detected at the dark color area. This is able to conclude that the light color area is the bulk of alloy and the dark color area is the scale of Fe which occurred because of internal oxidation. Furthermore, the EDS results show that Si, Al, Ca and O were detected in the cavity. The EDS results indicate that Fe, Co, Ni and O in the scale layer distributed in three layers, like the distribution in scale of uncoated sample: $CoFe_2O_4$ at the outermost scale, Fe_2O_3 at the middle scale and $NiFe_2O_4$ at the innermost. Consider the LNF coating, the coating still covers in some area on the top surface while the coating disappears in some area, as clearly seen in Fig.4.12c. In order to observe the diffusion of coating elements into the scale, EDS analysis was performed to find out whether La appeared in the scale or not. Only La was used to be representative of the coating because Ni and Fe were the compositions of scale ($CoFe_2O_4$, Fe_2O_3 and $NiFe_2O_4$). EDS results show that high amount of composition of coating which consisted of La, Ni and Fe were presented at the top of scale. Furthermore, La was detected in the scale which means there was the diffusion of coating into the scale. The coating diffused into the scale in two forms. The first one, high amount of La was found at the interface between $CoFe_2O_4$ layer and Fe_2O_3 layer, as clearly seen as a bright color line in Figs.4.12b and d. The other form, La was detected in the $CoFe_2O_4$ layer. Moreover, lots of traces of the coating were found in the Fe_2O_3 layer and in the $NiFe_2O_4$ layer, as clearly seen in Fig.4.12e.

As already mentioned, $CoFe_2O_4$, Fe_2O_3 and $NiFe_2O_4$ were still formed even the alloy was coated by LNF-SA. This means that LNF-SA coating cannot prevent the diffusion of metallic ions from FeCoNi alloy. The schematic diagrams of scale layers occurring in this case are shown in Fig 4.13.

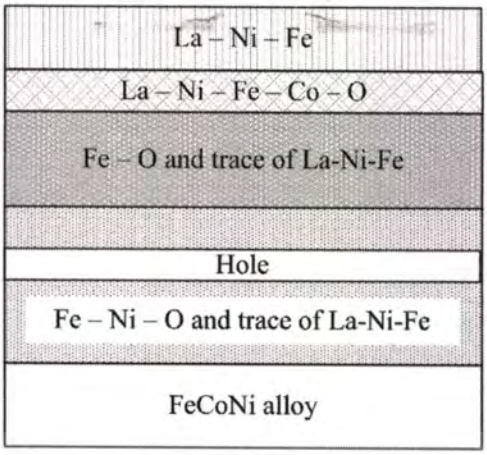

(a)

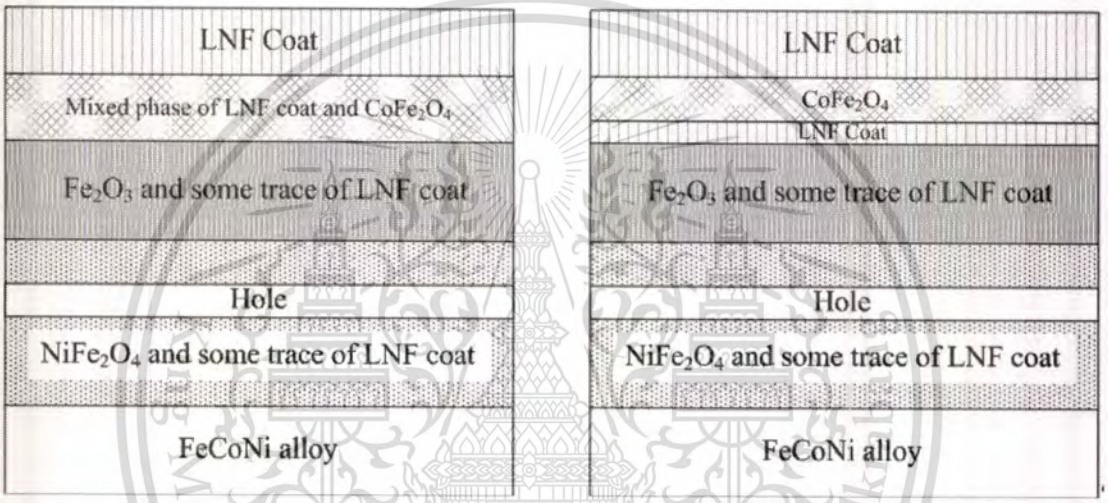

(b) (c)

Figure 4.13: The schematic diagrams of scale layer of LNF-SA coated on FeCoNi alloy after oxidation at 800 °C in O_2-5%H_2O at a total flow rate of 10 L/h for 455 h.

4.2.4. LNF-PVD-FeCoNi

After oxidation in O_2-5%H_2O at a total flow rate of 10 L/h at 800 °C for 455 h, the mean weight gain of FeCoNi which was coated by $La(Ni_{0.6}Fe_{0.4})O_3$ perovskite by physical vapor deposition (PVD) method was 13.81 mg/cm^2. SEM images of this sample are shown in Fig.4.14. It can be seen that there are only a few cracks of the coating appearing on the surface. The results from EDS show that there were Fe, Co and O appearing on area A in Fig.4.14h. In addition La, Ni, Fe and O were found on the area B. Therefore area A was possible to be the oxide while area B could be the coating.

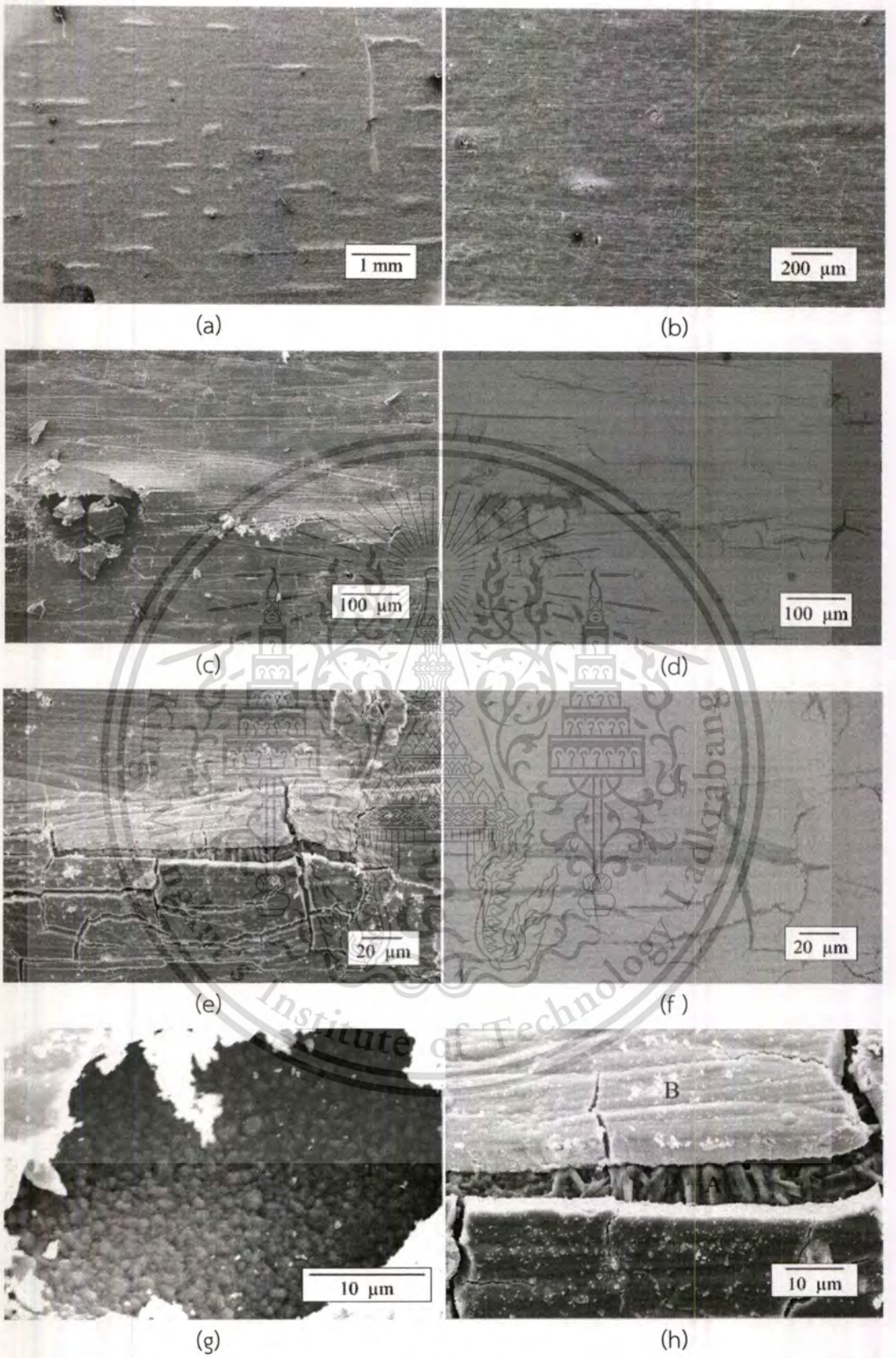

Figure 4.14: SEM images on surface of LNF-PVD coated on FeCoNi alloy after oxidation at 800 °C in O_2-5%H_2O at a total flow rate of 10 L/h for 455 h.

XRD results of this sample are shown in Fig.4.15. It can be seen that there are only peaks of substrate (LNF perovskite coating on FeCoNi) appearing on the XRD pattern before the oxidation. After the oxidation of LNF-PVD sample for 455 h in O_2-5%H_2O at 800 °C at a total flow rate of 10 L/h, the peaks of coating still appeared. It is possible that the coating almost completely covered the alloy.

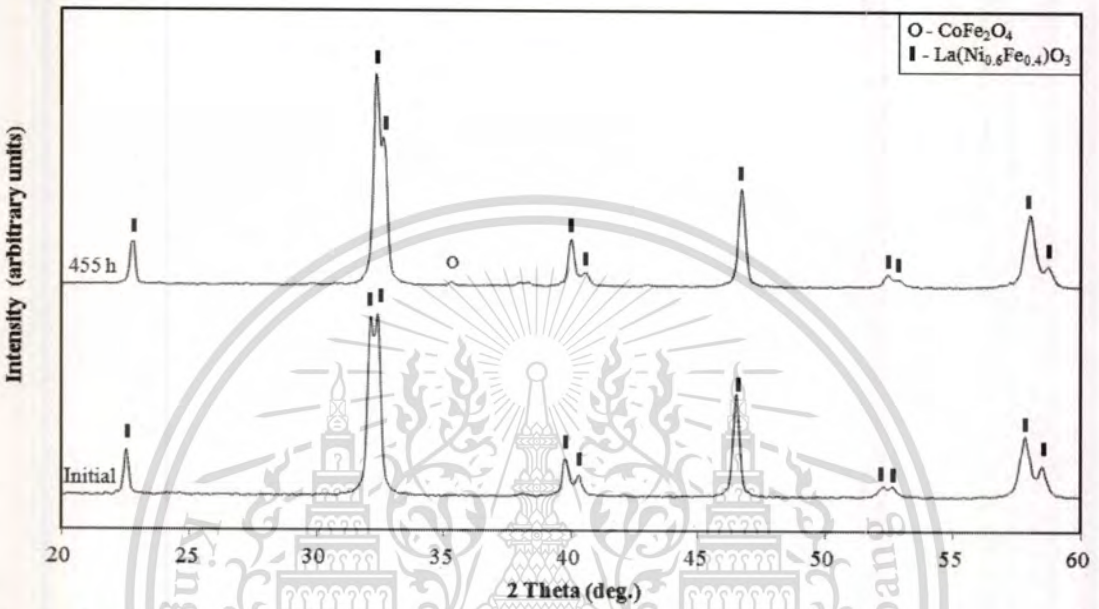

Figure 4.15: XRD results of LNF-PVD coated on FeCoNi alloy after oxidation at 800 °C in O_2-5%H_2O at a total flow rate of 10 L/h for 455 h.

Cross section images from backscattered SEM of LNF-PVD sample after oxidation for 455 h in O_2-5%H_2O at 800 °C at a total flow rate of 10 L/h are shown in Fig.4.16. It can be seen that there is the oxide scale with the thickness about 163 μm on the alloy surface. Moreover, there is the distribution of pores in the scale layer. Most of pores are found near the interface between scale and alloy. The different colors existing in the scale due to the distribution of elements were observed. In the alloy layer, internal oxidation occurred as small precipitates all over the metal.

(a)

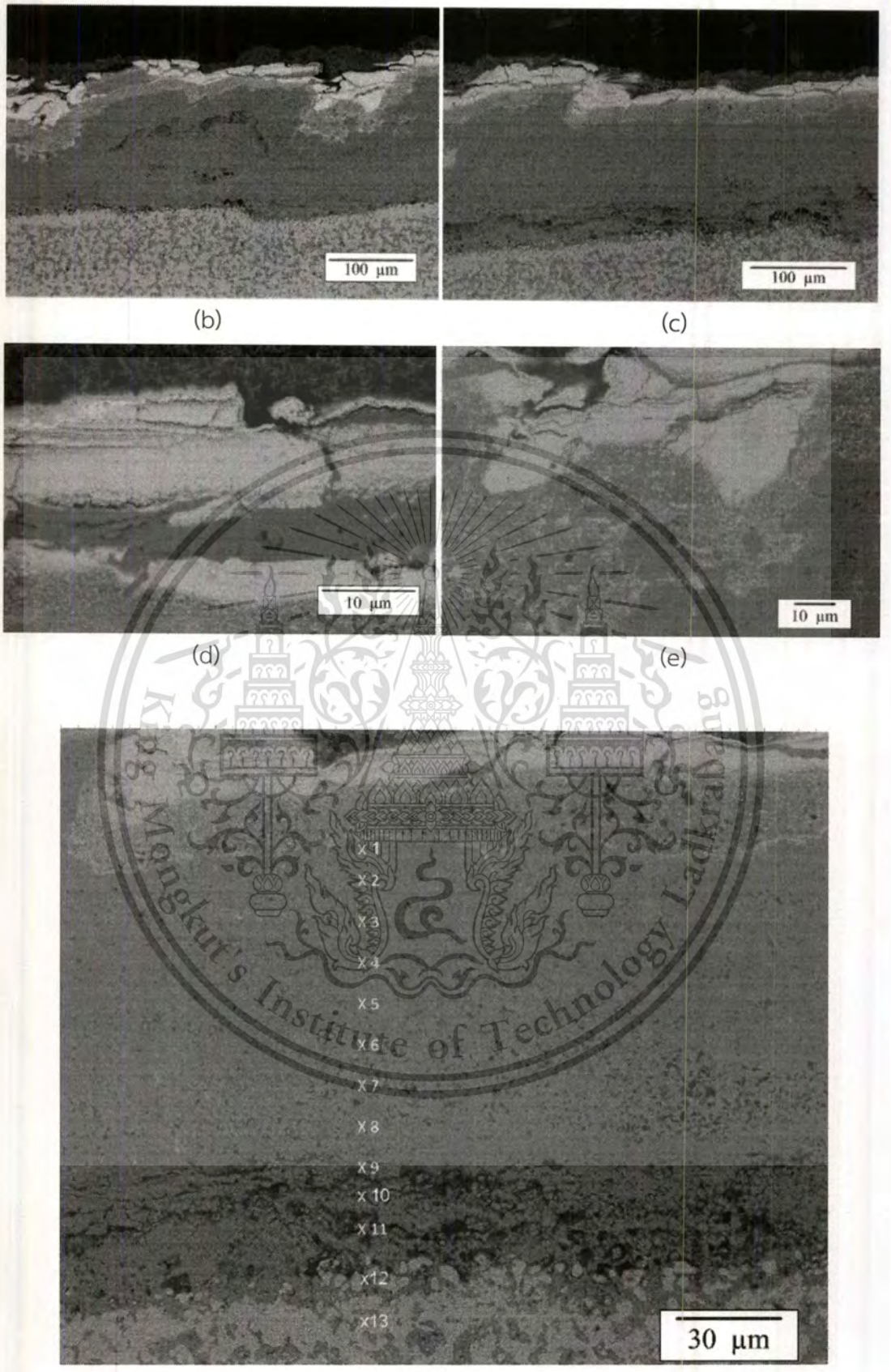

Figure 4.16: Cross sections images of LNF-PVD coated on FeCoNi alloy after oxidation at 800 °C in O_2-5%H_2O at a total flow rate of 10 L/h for 455 h.

Chemical analysis by EDS was carried out every 10 μm from top of scale into the metal layer, as shown in Appendix A-5. The results show that at the metal layer, high amount of Ni was detected in the light color area while Fe and O were detected in the dark color. This means that the light color area is the bulk of alloy and the dark color area is the scale of Fe which occurred because of internal oxidation. At the scale layer, EDS results indicated that the oxide of Fe, Co and Ni were formed as 3 layers: $CoFe_2O_4$ at the outermost scale, Fe_2O_3 at the middle scale and $NiFe_2O_4$ at the innermost. In addition, it was found by EDS analysis that there were high amounts of La, Ni and Fe above $CoFe_2O_4$ layer. This means that the coating still cover on the entire top surface of scale. EDS analysis showed that there was high amount of La presence in the $CoFe_2O_4$ layer, clearly seen as white color in Fig.4.16e. This means that the coating is able to diffuse into the scale.

From the previous discussion, the coating of LNF-PVD on FeCoNi is not able to prevent the forming of $CoFe_2O_4$, Fe_2O_3 and $NiFe_2O_4$. This means that LNF-PVD coating cannot prevent the FeCoNi alloy from oxidation at high temperatures. The schematic diagrams of scale layer are shown in Fig.4.17.

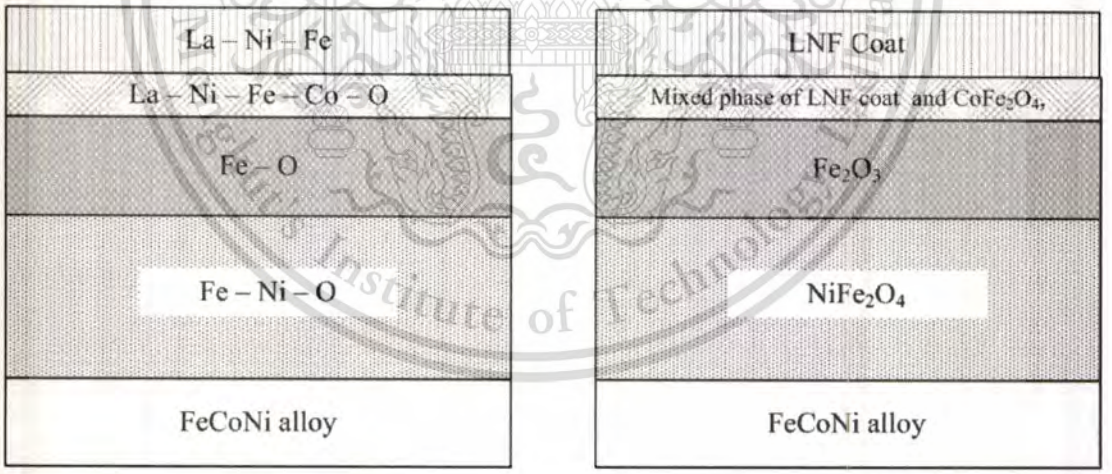

Figure 4.17: The schematic diagrams of scale layer of LNF-PVD coated on FeCoNi alloy after oxidation at 800 °C in O_2-5%H_2O at a total flow rate of 10 L/h for 455 h.

4.2.5 Co_3O_4-PVD-FeCoNi

The mean weight gain of FeCoNi alloy which was coated by Co_3O_4 spinel by cathodic sputtering (PVD coating) method after oxidation in O_2-5%H_2O at a total flow rate of 10 L/h at 800 °C for 500 h was 15.16 mg/cm^2. After oxidation, Co_3O_4-PVD sample was analyzed by XRD, SEM/EDS. SEM images on surface are shown in Fig.4.18.

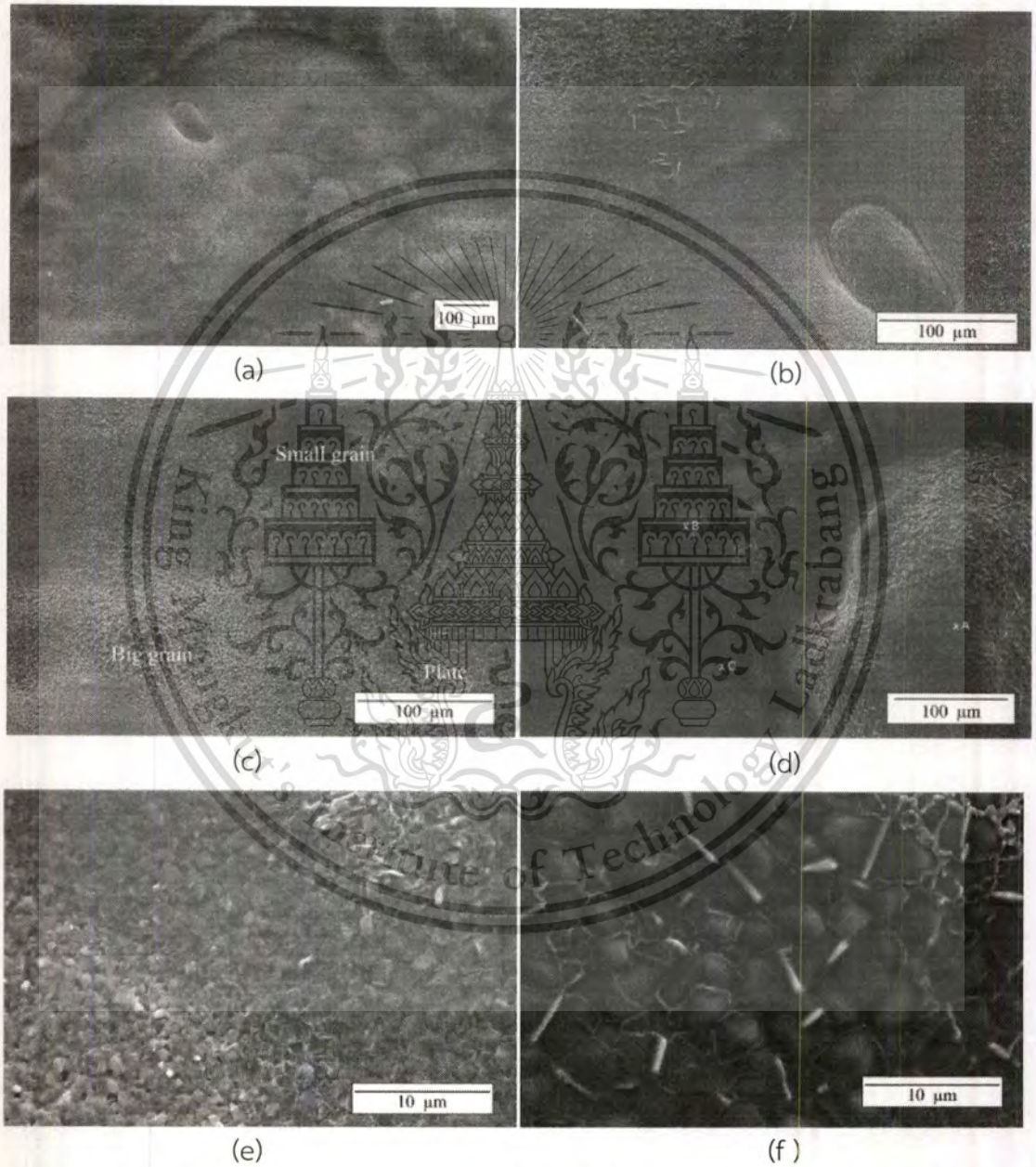

Figure 4.18: SEM images on surface of Co_3O_4-PVD coated on FeCoNi alloy after oxidation at 800 °C in O_2-5%H_2O at a total flow rate of 10 L/h for 500 h.

It can be seen from the SEM images that the coating is without the crack on entire surface. Moreover, It was found that on the surface there was the appearance of three morphologies which consisted of big grains (area A in Fig.4.18d), plates (area B in Fig.4.18d) and small grains (area C in Fig.4.18d), as seen in Figs.4.18c and d. The elemental analysis by EDS was performed on area A, B and C in Fig.4.22d. The results show that there are the same elements which consist of Fe, Co and O elements presenting on all three areas (A, B and C area). At area A, Co and O were detected in higher quantity than Fe. Whereas at the area B and area C, high amount of Fe, Co and O were detected.

XRD technique was used to identify the atomic structure of this sample, as shown in Fig.4.19. The results from XRD presented that after 500 h of oxidation, there were some small peaks which should be a part of peaks representing the XRD pattern of Co_3O_4-coating appearing. Furthermore, other peaks were presented on XRD pattern. In comparison with JCPD standard, the presented peaks match with the peaks of $CoFe_2O_4$ cubic, thus the new peaks are the peaks of $CoFe_2O_4$. As a result, there was two-phase appearance on the depths of within 5-10 μm from surface. Two-phase appearance is probably found because X-ray wave is able to penetrate through the scale layer.

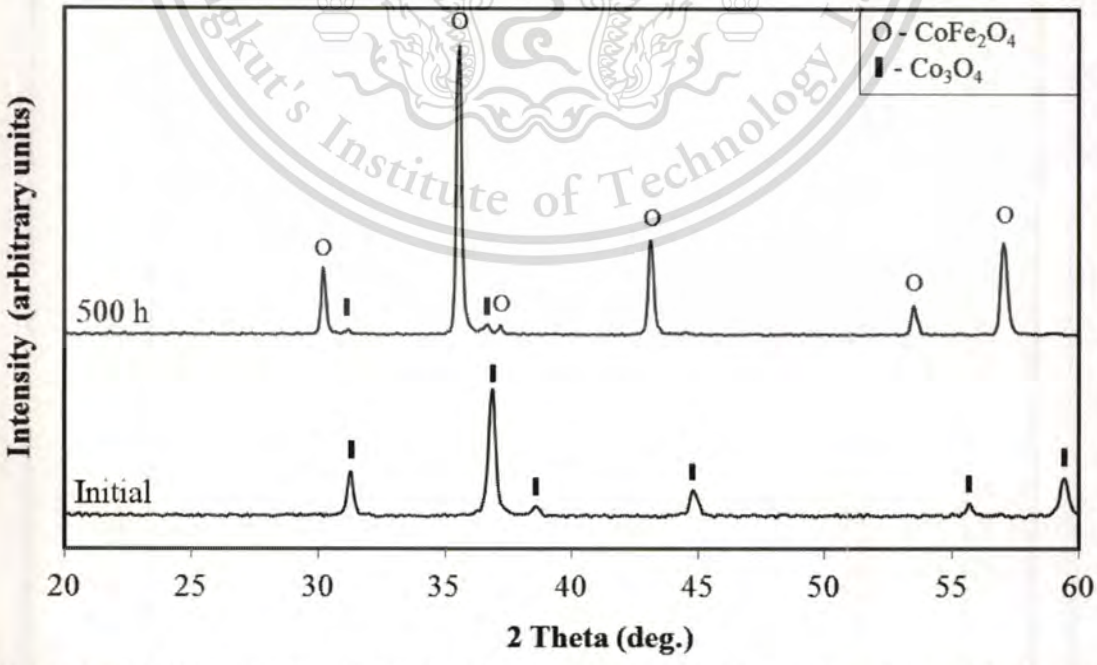

Figure 4.19: XRD results of Co_3O_4-PVD coated on FeCoNi alloy after oxidation at 800 °C in O_2-5%H_2O at a total flow rate of 10 L/h for 500 h.

After XRD and SEM/EDS analysis on the surface, the Co_3O_4-PVD alloy was analyzed by SEM/EDS on cross section. From SEM, cross section images of Co_3O_4-PVD FeCoNi after oxidation in O_2-5%H_2O at 800 °C for 500 h are shown in Fig.4.20. It can be seen that there is pore distribution within the scale. Most of pores were presented at the interface between scale and metal. Moreover, there are oxidation occurrence as internal oxidation and external oxidation. The internal oxidation was formed as small participate oxides all over the metal layer while the external oxidation was formed as scale with thickness about 117 μm. In the scale layer, the different color layers which refer to the different distribution of elements appeared.

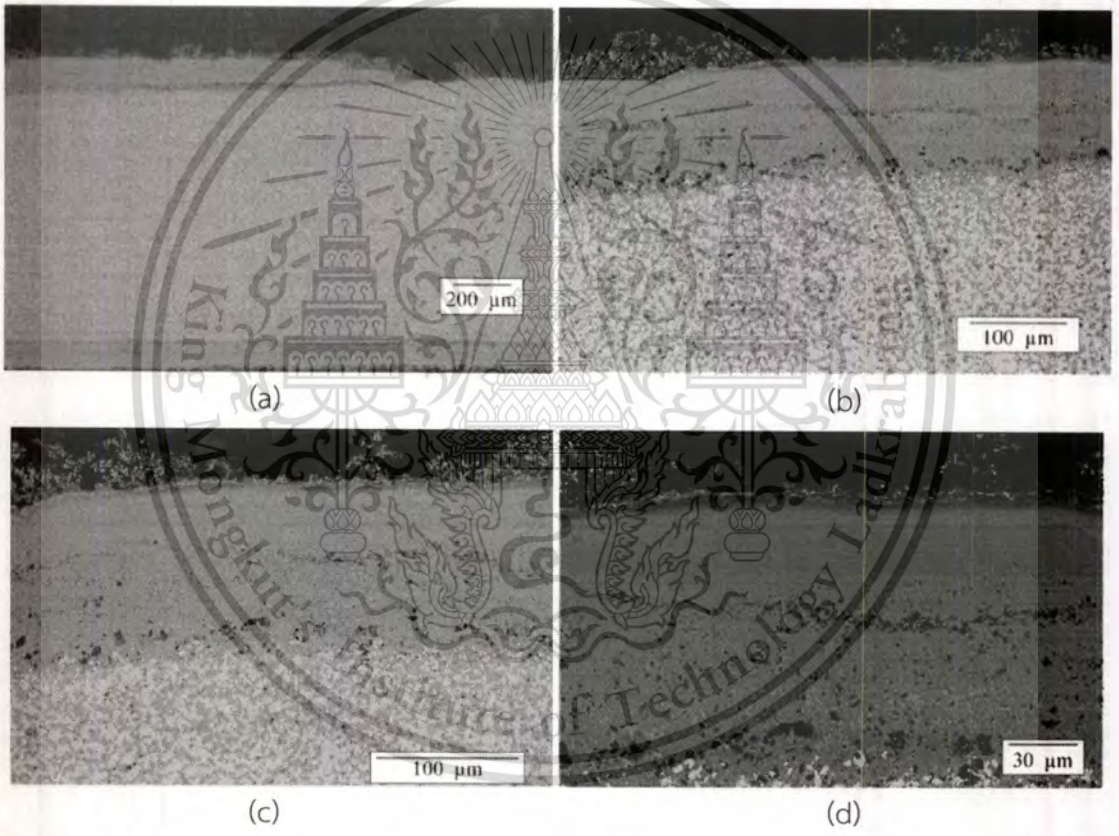

Figure 4.20: Cross sections images of Co_3O_4-PVD coated on FeCoNi alloy after oxidation at 800 °C in O_2-5%H_2O at a total flow rate of 10 L/h for 500 h.

In order to analyze the element distribution, chemical analysis by EDS was carried out at every 10 μm from top of scale into the metal layer, as shown in Appendix A-6. The EDS results at the metal layer show that high amount of Ni was detected at the light color while Fe and O were detected at the dark color. This is able to conclude that the light color area is the bulk of alloy and the dark color area

is the scale of Fe which occurred because of internal oxidation. In order to observe the diffusion of the Co_3O_4 coating into the scale, Co and O are the composition of both the Co_3O_4 coating and the scale ($CoFe_2O_4$, Fe_2O_3 and $NiFe_2O_4$), only EDS data are difficult to make clear that where are Co and O diffuse from, because Co existing in the scale is able to diffuse from either the coating or the alloy. Therefore, the different color layers existing in the SEM images were considered with EDS results. At the scale layer, the EDS analysis at the first 5 μm from surface, as seen in the dark color line in Figs.4.20b, c and d, showed that there were both of Co and O distributing in this area while Fe did not appeared. Thus it is possible that the first 5 μm layer of the surface was the coating. In the next layer, high amount of Co, O and some amount of Fe were detected shown as the bright color in Figs.4.20b, c and d. XRD result shows that there are the peaks of $CoFe_2O_4$ cubic appearing on XRD pattern. It is possible that the coating layer is thin, thus X-ray wave that penetration depths of within 5-10 μm is able to go through to the next layer. Therefore the Co_3O_4 coating still cover on the outermost of the scale, and next layer of scale shown as the bright color is $CoFe_2O_4$ layer. But because there are high amount of Co and O existing in $CoFe_2O_4$ layer, Co in this layer should not diffuse from only the alloy, Co should diffuses from the coating also. Therefore this coating can diffuse to $CoFe_2O_4$ layer.

Moreover, Co was also found in the next layer which should be the Fe_2O_3 layer, shown as the dark color layer in Figs.4.20c and d. From EDS results, it cannot be confirmed that Co presenting in this layer inward diffuses from the coating or outward diffuses from the metal. However when compared with the amount of Co and O in the Fe_2O_3 layer in other samples, it was found that the amount of Co and O presenting in this sample was more than the others. Therefore, it is possible that some Co presenting in this scale diffused from the coating. Then, in the bright color layer in the direction deep into the metal, it was found that there were Fe, O and Ni existing in the same tendency found in the bottom layer of oxidized uncoated sample. This layer should be the layer of $NiFe_2O_4$.

As already mentioned, $CoFe_2O_4$, Fe_2O_3 and $NiFe_2O_4$ were still formed even the alloy was coated by Co_3O_4-PVD. Therefore, Co_3O_4-PVD coating is not able to prevent the oxidation of FeCoNi alloy at high temperatures. The schematic diagrams of scale layer are shown in Fig.4.21.

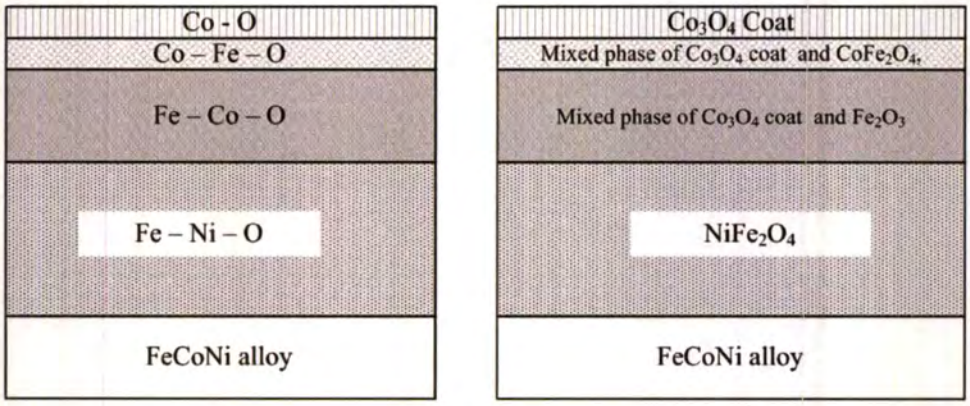

Figure 4.21: The schematic diagrams of scale layer of Co_3O_4-PVD coated on FeCoNi alloy after oxidation at 800 °C in O_2-5%H_2O at a total flow rate of 10 L/h for 500 h.

4.2.6 $MnCo_2O_4$-PVD-FeCoNi

After oxidation for 500 h in O_2-5%H_2O at a total flow rate of 10 L/h at 800 °C, the mean weight gain of FeCoNi alloy which was coated by $MnCo_2O_4$ spinel by physical vapor deposition (PVD) method was 12.20 mg/cm^2 which was the lowest value when compared with other samples. This seems that $MnCo_2O_4$-PVD sample has high performance in reducing the oxidation of FeCoNi alloy. However, in fact the $MnCo_2O_4$-PVD coating on the top side spalled from the metal after long term oxidation, as shown in Fig.4.22. This means that FeCoNi alloy which was coated by $MnCo_2O_4$-PVD coating is not suitable for using as an interconnector in a solid oxide electrolytic cell.

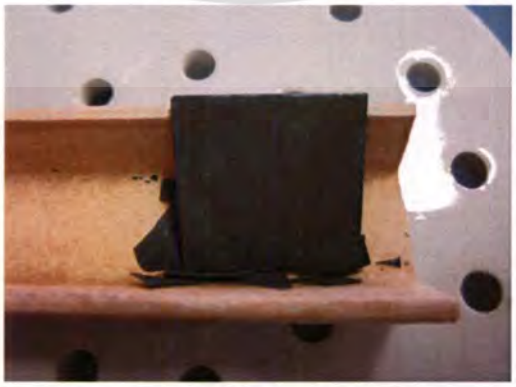

Figure 4.22: Physical characteristics of $MnCo_2O_4$-PVD coated on FeCoNi alloy after oxidation at 800 °C in O_2-5%H_2O at a total flow rate of 10 L/h for 500 h.

In this research, the oxidation of both uncoated and coated FeCoNi alloys was performed at 800 °C in O_2-5%H_2O at a total flow rate of 10 L/h for long time. It can be seen that there are scales forming in three layers: $CoFe_2O_4$, Fe_2O_3 and $NiFe_2O_4$ respectively. For coated samples, EDS analysis shows that there are the distribution of the coating in the scale layer. This means that these coatings are not able to protect the diffusion of oxygen and metallic ion. However, the coating is able to reduce the thickness of scale which means that the coating is able to reduce the oxidation of FeCoNi alloy. The mean weight gains of samples after oxidation were shown in Table 4.3.

Table 4.3 The mean weight gains per area of samples after oxidation at 800 °C in O_2-5%H_2O at a total flow rate of 10 L/h for long time.

FeCoNi alloy	weight gain/area (mg/(cm^2)	
	455 h of oxidation	500 h of oxidation
Uncoated	17.09**	17.91*
LSM-SA	14.04*	14.72**
LNF-SA	13.94*	14.62**
LNF-PVD	13.81*	14.48**
Co_3O_4-PVD	14.46**	15.16*
$MnCo_2O_4$-PVD	11.64**	12.21*

* raw data.

** expected value calculated from Equation 4.1.

4.3 Scale forming

After oxidation in O_2-5%H_2O at a total flow rate of 10 L/h at 800 °C for 1 min, 5 min, 15 min, 1 h, 16 h, 72 h, 96 h, 455 h and 500 h, uncoated samples were analyzed to find the atomic structure of scale by XRD. The results are shown in Fig.4.23.

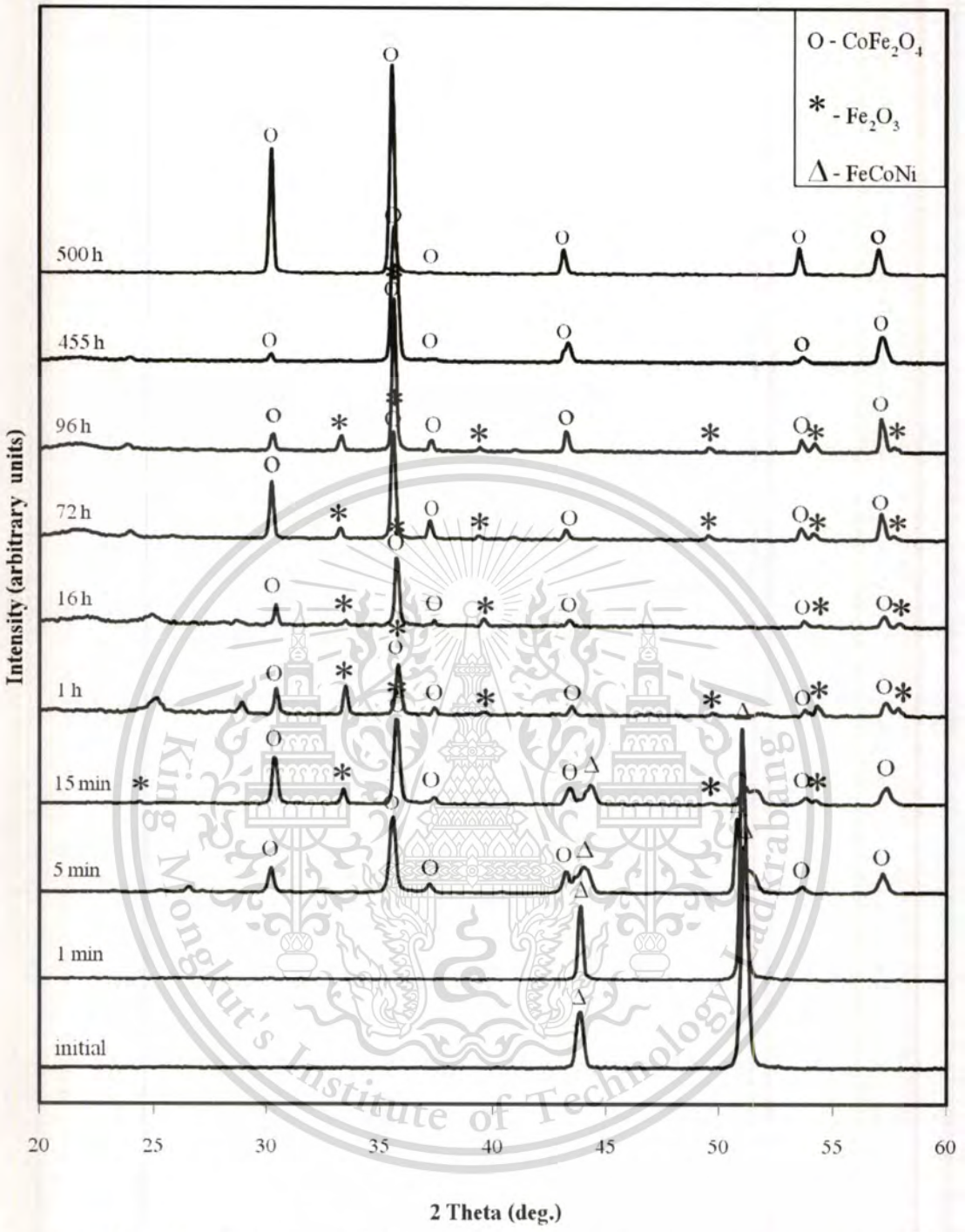

Figure 4.23: XRD results of uncoated sample before and after oxidation at 800 °C in O_2-5%H_2O at a total flow rate of 10 L/h for various time.

The results from XRD analysis which compared with JCPD standard show that at initial time there are only peaks of FeCoNi alloy substrate appearing. After oxidation for 1 min, the peaks of substrate still appear. At the oxidation time of 5 min, these peaks of substrate are still found, other peaks are observed. The other peaks appearing in XRD pattern are possible to be the peaks of $CoFe_2O_4$ cubic.

This means at the 5 min of oxidation, there is the scale of $CoFe_2O_4$ cubic forming. Because X-ray wave is able to penetrate into the depths of within 5-10 μm, and the $CoFe_2O_4$ scale occurring after the oxidation for short time should be thinner than this range, the X-ray wave is able to penetrate through the scale layer. The XRD result after oxidation for 15 min shows that the peaks of FeCoNi and the peaks of $CoFe_2O_4$ are still appeared. Moreover, other peaks which are possible to be peaks of Fe_2O_3 were found. From the oxidation time of 15 min until the oxidation time of 96h, Fe_2O_3 peaks and $CoFe_2O_4$ peaks were continuously found on the XRD pattern. At this point, it is unable to know that which oxide stays on top. However, after oxidation for 455 h, the peaks of Fe_2O_3 disappear, only the peaks of $CoFe_2O_4$ cubic were found. Therefore, it is possible that the scale of $CoFe_2O_4$ cubic was formed on the outermost scale layer while Fe_2O_3 was formed at under $CoFe_2O_4$ layer. In the case of the oxidation for 455 h and 500 h, the thickness of $CoFe_2O_4$ should be more than 5-10 μm, X-ray wave was unable to penetrate through the Fe_2O_3 layer thus only $CoFe_2O_4$ peaks appeared on XRD pattern.

From three layer scale which formed on the oxidized uncoated FeCoNi: $CoFe_2O_4$, Fe_2O_3 and $NiFe_2O_4$, it is possible that when O contacts with alloy surface, oxidation of Co and Fe should immediately form as $CoFe_2O_4$. Then unreacted O inwards diffuses into the metal, and iron was oxidized to hematite (Fe_2O_3), therefore nickel was enrichment at the metal surface. During consequent oxidation, nickel ferrite spinel ($NiFe_2O_4$) was formed as a discrete layer at the interface between scale and metal. Because of the presence of some Co in the $NiFe_2O_4$ layer, Co which was found should be in diffusion path of outwards diffusion from metal to the $CoFe_2O_4$ layer. Therefore, there should be the diffusion of oxygen from atmosphere to alloy surface and metallic ions, Fe and Co, in the opposite direction while Ni was not mobile. The schematic model of direction of ion diffusion in the scale forming is shown in Fig.4.24.

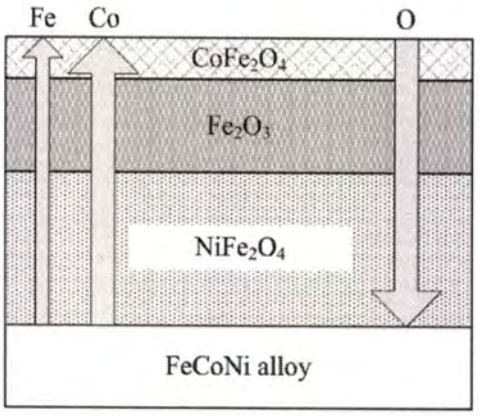

Figure 4.24: The schematic model of direction of ions diffusion in the scale forming of uncoated sample in oxidation at 800 °C in O_2-5%H_2O at a total flow rate of 10 L/h.

4.4 The hardness of coating samples

In order to study the hardness of coatings, Vickers hardness method was performed. After indented with a diamond indenter with a load of 50, 100, 150, 187.5 and 250 kgf for 10 sec, the diagonal length which left on surface of samples for each load were captured by SEM. The diagonal length was measured using ImageJ program, as present in Appendix.B. The Vickers hardness is obtained by calculation from Equation 4.2. Vickers hardness was multiplied by 9.807 to convert to MPa unit.

$$HV = \frac{2F\sin\frac{136^o}{2}}{d^2} \approx 1.854\,\frac{F}{d^2} \qquad (4.2)$$

where HV = Vickers hardness
F = Force (kgf)
d = Mean diagonal length (mm)

For example, the SEM image of LSM-SA sample which was intended by a load of 100 kgf for 10 sec shown in Fig.4.25. The mean diagonal length which left on the surface of this sample was approximately 1130 μm, thus the Vickers hardness calculated from Equation 4.2 was 141HV or 1379.24 MPa.

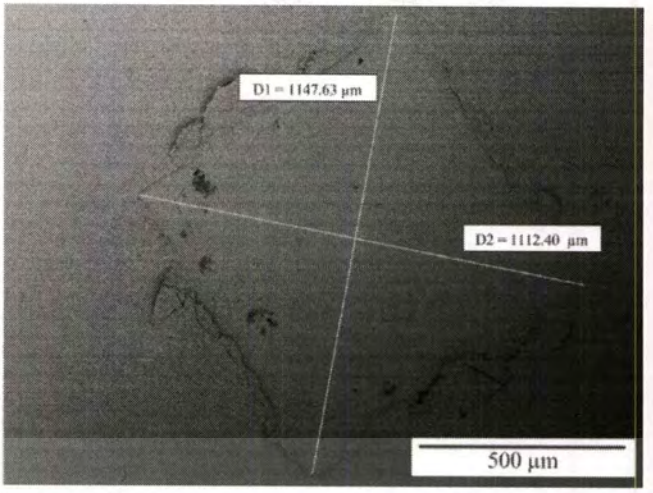

Figure 4.25: SEM image of LSM-SA coated on FeCoNi alloy which was intended by Vickers hardness test by a load of 100 kgf for 10 sec.

The hardness of coating samples in Vickers hardness number and MPa for each load is shown in Fig.4.26.

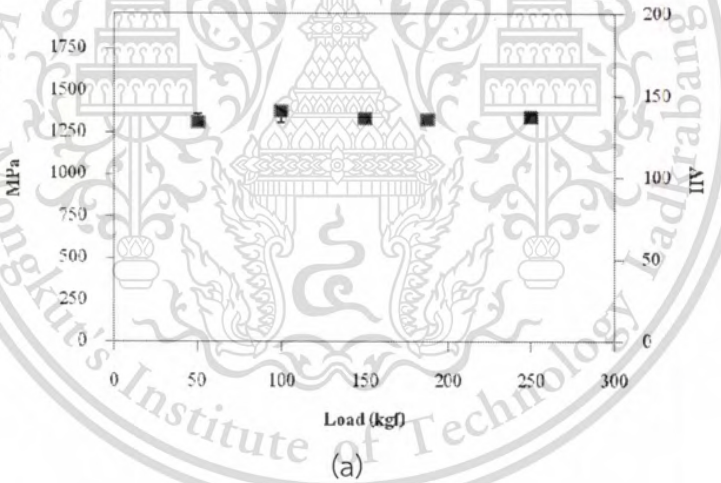

(a)

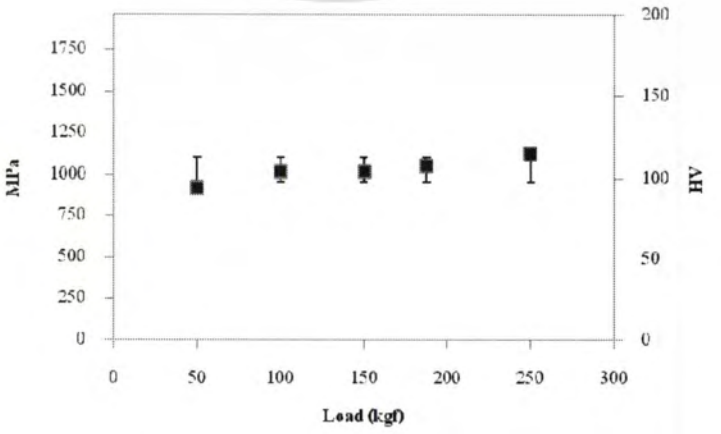

(b)

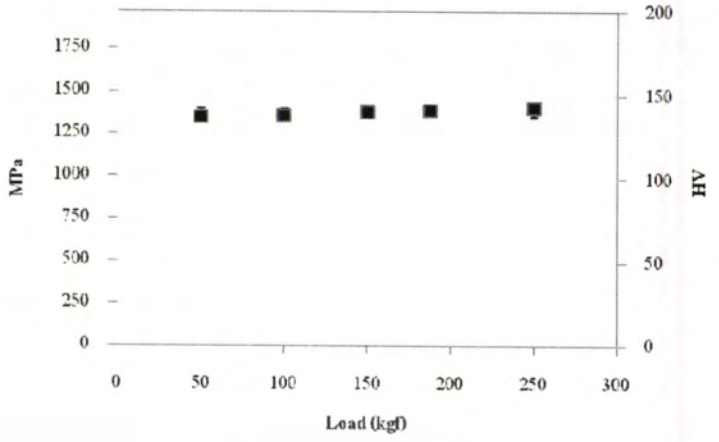

(c)

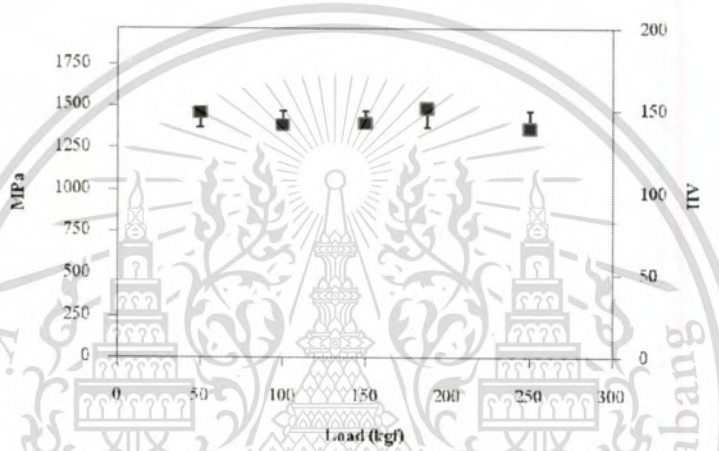

(d)

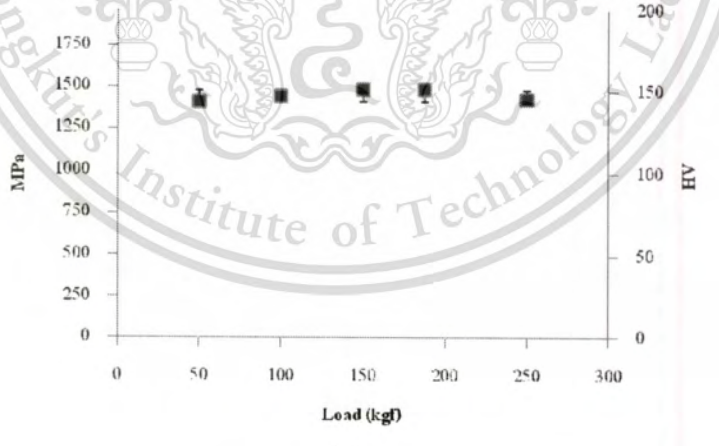

(e)

Figure 4.26: The hardness of the coated samples various intended load. (a) LSM-SA FeCoNi (b) LNF-SA FeCoNi (c) LNF-PVD FeCoNi (d) Co_3O_4-PVD FeCoNi (e) $MnCo_2O_4$-PVD FeCoNi

It was found that the coated samples in this research have the hardness value in range of 105-148 HV. The hardness of the coated samples arranged in order is:

LNF-SA FeCoNi < LSM-SA FeCoNi

< LNF-PVD FeCoNi < Co_3O_4-PVD FeCoNi < $MnCo_2O_4$-PVD FeCoNi.

The hardness of the coated samples is also shown in Table.4.4.

Table 4.4 The average hardness of the coated samples.

Coated samples	Avg. hardness (HV)	Avg. hardness (MPa)	Std.
LSM-SA	136.47	1338.33	2.57
LNF-SA	105.05	1030.25	7.63
LNF-PVD	140.09	1373.86	2.19
Co_3O_4-PVD	144.76	1419.64	5.12
$MnCo_2O_4$-PVD	147.54	1446.93	3.47

In order to consider the physical of the coating samples in each method, LNF samples which were coated by SA method and by PVD method were compared. SEM image of the LNF-SA sample which was intended by a load of 187.5 kgf for 10 sec shown in Fig.4.27a, and that of LNF-SA is shown in Fig.4.27b.

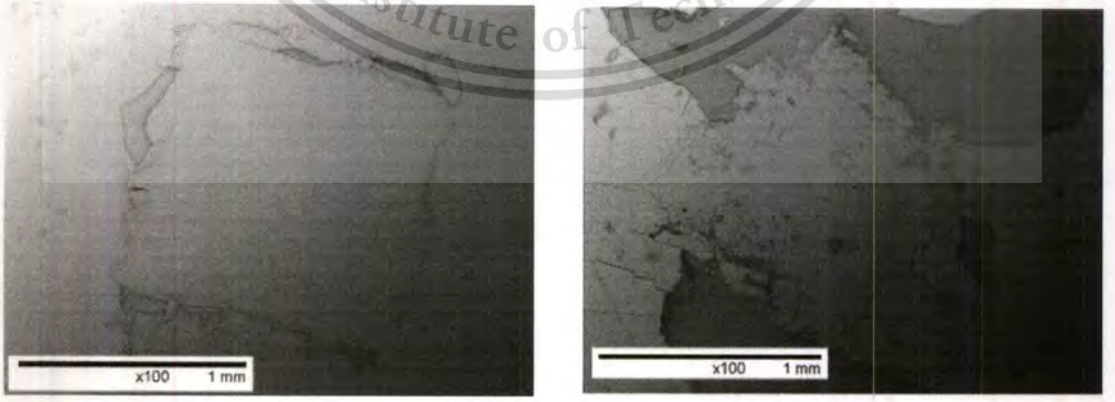

(a) (b)

Figure 4.27: SEM images on surface of LNF coated on FeCoNi alloy which were intended by Vickers hardness test by a load of 187.5 kgf for 10 sec. (a) LNF-SA FeCoNi (b) LNF-PVD FeCoNi

It was found that the Vickers hardness of coating samples which was coated by PVD method was higher than SA method. Considering the surface of samples after intended, for the LNF sample which was coated by SA method, the crack of the coating occurs only at the perimeter. On the other hand, in case of LNF sample which was coated by PVD method, after intended in the same way, a lot of crack occurs all over and around the area which was intended. A lot of the PVD coating fell out of the sample after sample was intended. This means that in physical, the coating by SA method seems to be better than the coating by PVD method.

Chapter 5

Conclusions and Suggestions

5.1 Conclusions

This research attempts to evaluate the oxidation behavior of coated FeCoNi alloys expected to use as an interconnector in solid oxide electrolytic cell. The coatings consist of

- $La_{0.8}Sr_{0.2}MnO_3$ coated by slurry application method
- $La(Ni_{0.6}Fe_{0.4})O_3$ coated by slurry application method
- $La(Ni_{0.6}Fe_{0.4})O_3$ coated by physical vapor deposition method
- Co_3O_4 coated by physical vapor deposition method
- $MnCo_2O_4$ coated by physical vapor deposition method.

The samples were oxidized at 800 $^{\circ}C$ in O_2-5%H_2O at a total flow rate of 10 L/h. After oxidation, the samples were analyzed by SEM/EDS and XRD. Moreover, the hardness of non-oxidized coated samples was also measured. As already mentioned, it is able to conclude that:

1. Considering in kinetic oxidation of samples, the weight gain per area of samples increased as parabolic function of time. The LNF coatings were able to reduce the oxidation rate of FeCoNi alloy for around four times when considering from parabolic rate constants (k_p). The LNF coating using PVD method better reduced oxidation of FeCoNi alloy than using SA method.

2. Considering the morphologies of the samples, after long term oxidation the surface of perovskite coating samples cracked while the surface of spinel coating samples did not crack.

3. The external oxidation of FeCoNi alloy formed the scale as layers of $CoFe_2O_4$, Fe_2O_3 and $NiFe_2O_4$ from outer to inner, respectively. The direction of ions diffusion in scale forming should be the diffusion of oxygen from atmosphere to alloy surface and metallic ions, Fe and Co, in the opposite direction while Ni was not mobile

4. The result of internal-oxidation morphology occurring after long term oxidation can be concluded that the coating using SA method seemed to be better in reducing internal oxidation of FeCoNi alloy than the PVD coating method.

5. The scales of FeCoNi alloy were still formed even the samples were coated. Moreover, some coating elements diffused into the scale layer. Therefore, these coatings cannot prevent the diffusion of metallic ions from FeCoNi alloy.

6. The hardnesses of the coated samples using PVD method were higher than hardnesses of the coated samples using SA method.

As these results, it can be concluded that the coating in this research are able to reduce the oxidation of FeCoNi alloy but cannot protect the FeCoNi alloy from oxidation at high temperature under humidified atmosphere.

5.2 Suggestions

This FeCoNi alloy is still interesting for applying as an interconnector due to the occurrence of protective $NiFe_2O_4$ spinel which can significantly improve the oxidation resistance of the alloy [21].

1. In order to improve the oxidation behavior of this alloy, this alloy should be modified and developed by changing the composition such as adding some element as in Zhu et al.'s research.

2. The electrical properties of this alloy should be tested in further study.

References

[1] Harrison K. and Levene J. I. **Solar Hydrogen Generation Toward a Renewable Energy Future.** New York : Springer Science+Business Media. 2008.

[2] Ardigo` M.R., Popa I., Chevalier S., Desgranges C. and Bousquet R. "Evaluation of a new Cr-free alloy as interconnect material for hydrogen production by high temperature water vapour electrolysis: Study in cathode atmosphere" **International Journal of Hydrogen Energy.,** [online]. Available : doi: 10.1016/j.ijhydene.2012.02.069. 2012.

[3] Hawkes G. L., O'Brien J. E., Stoots C. M., Herring J. S. and Shahnam M. "CFD Model Of A Planar Solid Oxide Electrolysis Cell For Hydrogen Production From Nuclear Energy" **The 11th International Topical Meeting on Nuclear Reactor Thermal-Hydraulics (NURETH-11), Popes' Palace Conference Center, Avignon, France.,** October 2005.

[4] Wang Z., Mori M. and Araki T. "Steam Electrolysis Performance of Intermediate-Temperature Solid Oxide Electrolysis Cell and Efficiency of Hydrogen Production System at 300 $Nm^3 h^{-1}$" **International Journal of Hydrogen Energy.,** vol.35, March 2010. pp. 4451-4458.

[5] Jensen S. H. **Solid Oxide Electrolyser Cell.** Ph.D. Thesis of Solid State Chemistry and Fuel Cells Department, University of Denmark. 2006.

[6] Schiller G., Ansar A., Lang M. and Patz O. "High Temperature Water Electrolysis using Metal Supported Solid Oxide Electrolyser Cells (SOEC)" **J Appl Electrochem.,** vol.39, October 2008. pp. 293–301.

[7] Shaigan N., Qu W., Ivey D. G. and Chen W. "A Review of Recent Progress in Coatings, Surface Modifications and Alloy Developments for Solid Oxide Fuel Cell Ferritic Stainless Steel Interconnects" **Journal of Power Sources.,** vol.195, October 2009. pp. 1529-1542.

[8] Geng S., Zhu J., Brady M. P., Anderson H. U., Zhou X. D. and Yang Z. "A low-Cr Metallic Interconnect for Intermediate-Temperature Solid Oxide Fuel Cells" **Journal of Power Sources.,** vol.172, May 2007. pp. 775–781.

[9] Froitzheim J., Ravash H., Larsson E., Johansson L. G., and Svensson J. E. "Investigation of Chromium Volatilization from FeCr Interconnects by a Denuder Technique" **Journal of The Electrochemical Society.**, vol.157, July 2010. pp. B1295-B1300.

[10] Pyo S. S., Lee S. B., Lim T. H., Song R. H., Shin D. R., Hyun S. H. and Yoo Y. S. "Characteristic of $(La_{0.8}Sr_{0.2})_{0.98}MnO_3$ Coating on Crofer22APU used as Metallic Interconnects for Solid Oxide Fuel Cell" **International journal of hydrogen energy.**, vol.36, February 2010. pp. 1868-1881.

[11] Ebrahimifar H. and Zandrahimi M. "Mn Coating on AISI 430 Ferritic Stainless Steel by Pack Cementation Method for SOFC Interconnect Applications" **Solid State Ionics.**, vol.183, January 2011. pp. 71-79.

[12] Singhal S.C. and Kendall K. **High Temperature Solid Oxide Fuel Cells: Fundamentals, Design and Applications.** Great Britain: Elsevier Ltd. 2003.

[13] Perssona Å. H., Mikkelsena L., Hendriksena P. V and Somers M. A. J. "Interaction Mechanisms between Slurry Coatings and Solid Oxide Fuel Cell Interconnect Alloys During High Temperature Oxidation" **Journal of Alloys and Compounds.**, [online]. Available : doi:10.1016/j.jallcom.2011.12.095. 2012.

[14] Piccardo P., Chevalier S., Molins R., Viviani M., Caboche G., Barbucci A., Sennour M. and Amendola R. "Metallic Interconnects for SOFC: Characterization of their Corrosion Resistance in Hydrogen/Water Atmosphere and at the Operating Temperatures of Differently Coated Metallic Alloys" **Surface and Coatings Technology.**, vol.201, September 2006. pp. 4471-4475.

[15] Kim B. S., Kim B. G., Lee H. W. and Chung W. S. "Kinetics of Fe-30%Ni-12.5%Co Invar Alloy during High Temperature Oxidation" **Metal and Materials International.**, vol.8, no. 4, 2002, pp. 367-373.

[16] Chapman V., Welch B. J. and Skyllas-Kazacos M. "High Temperature Oxidation Behaviour of Ni–Fe–Co Anodes for Aluminium Electrolysis" **Corrosion Science.**, [online]. Available : doi:10.1016/j.corsci.2011.05.018. 2011.

[17] Zhu J. H., Geng S. J. and Ballard D. A. "Evaluation of Several Low Thermal Expansion Fe–Co–Ni Alloys as Interconnect for Reduced-Temperature Solid Oxide Fuel Cell" **International Journal of Hydrogen Energy.**, vol.32, September 2007. pp. 3682–3688.

[18] Chu S. Y. and Hong C.S. "Effects of the MnO Additives on the Properties of $Pb(Fe_{2/3}W_{1/3})$-$PbTiO_3$ Relaxors: Comparison of Empirical Law and Experimental Results" **Journal of Applied Physics.,** vol.101, March 2007. pp. 054117.

[19] Rabe K. M. "First-Principles Calculations of Complex Metal-Oxide Materials" **Annual Review of Condensed Matter Physics.,** vol.1, August 2010. pp. 211-235.

[20] Palcut M., Mikkelsen L., Neufeld K., Chen M., Knibbe R. and Hendriksen P. V. "Improved Oxidation Resistance of Ferritic Steels with LSM Coating for High Temperature Electrochemical Applications" **International Journal of Hydrogen Energy.,** [online]. Available : doi:10.1016/j.ijhydene.2011.11.138. 2012.

[21] Chen K. and Jiang S. P. "Failure Mechanism of (La,Sr)MnO_3 Oxygen Electrodes of Solid Oxide Electrolysis Cells" **International journal of hydrogen energy.,** vol.36, June 2011. pp. 10541-10549.

[22] Chiba R., Yoshimura F. and Sakurai Y. "An Investigation of $LaNi_{1-x}Fe_xO_3$ as a Cathode Material for Solid Oxide Fuel Cells" **Solid State Ionics.,** vol.124, January 1999. pp. 281-288.

[23] Petric A. and Ling H. "Electrical Conductivity and Thermal Expansion of Spinels at Elevated Temperatures" **Journal of the American Ceramic Society.,** vol.90, April 2007. pp. 1515–1520.

[24] Burriela M., Garcia G., Santiso J., Hansson A. N., Linderoth S. and Figueras A. "Co_3O_4 Protective Coatings Prepared by Pulsed Injection Metal Organic Chemical Vapour Deposition" **Thin Solid Films.,** vol.473, October 2004. pp. 98-103.

[25] Wei W., Chen W. and Ivey D. G. "Oxidation Resistance and Electrical Properties of Anodically Electrodeposited Mn–Co Oxide Coatings for Solid Oxide Fuel Cell Interconnect Applications" **Journal of Power Sources.,** vol.186, September 2008. pp. 428-434.

Appendices

Appendices A

EDS analysis on cross section of the oxidized samples

Appendix A-1: EDS analysis on top side of the oxidized uncoated FeCoNi.

Appendix A-2: EDS analysis on bottom side of the oxidized uncoated FeCoNi.

Appendix A-3: EDS analysis of the oxidized LSM-SA FeCoNi.

Appendix A-4: EDS analysis of the oxidized LNF-SA FeCoNi.

Appendix A-5: EDS analysis of the oxidized LNF-PVD FeCoNi.

Appendix A-6: EDS analysis of the oxidized Co_3O_4-PVD FeCoNi.

Appendix A-1: EDS analysis on top side of the oxidized uncoated FeCoNi.

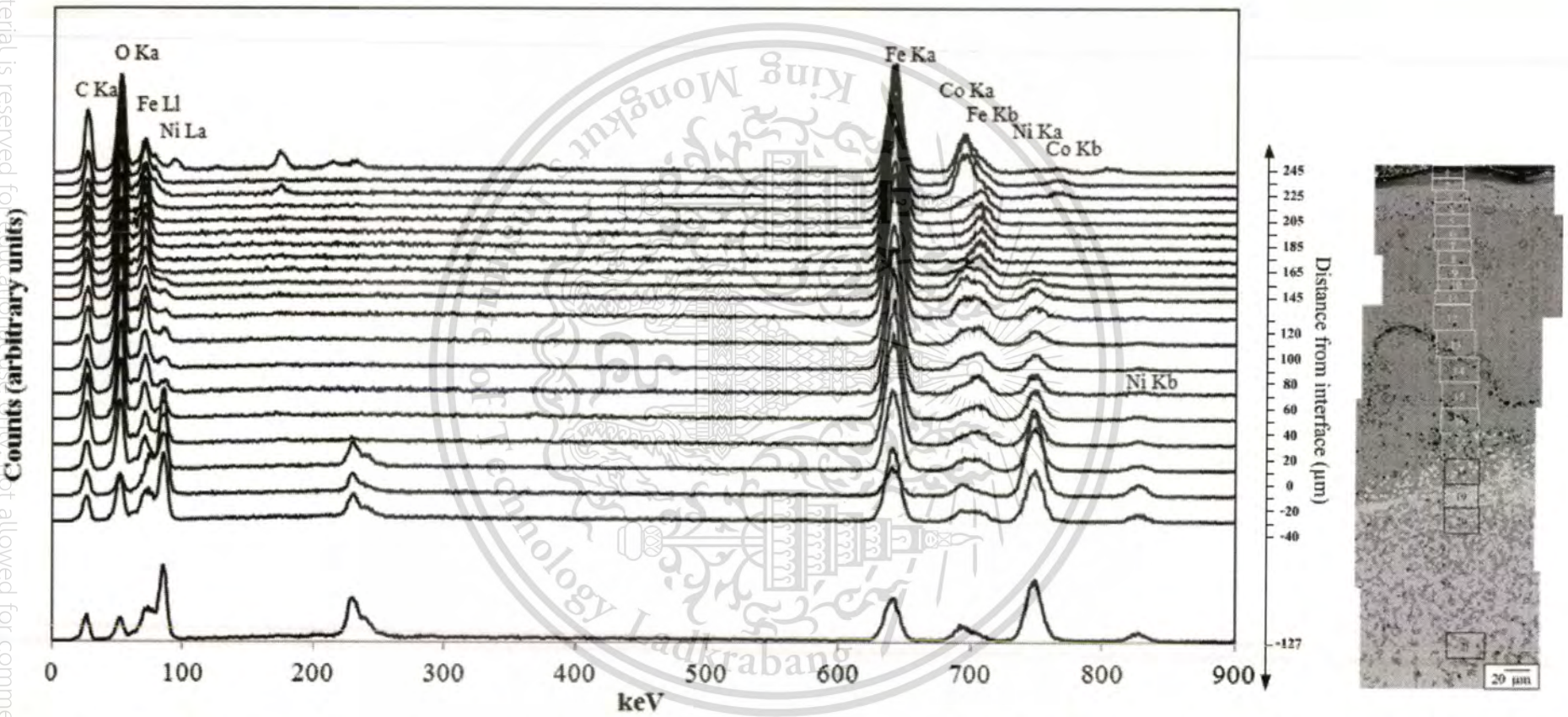

Figure A-1: EDS analysis from the outermost of scale into the metal layer on top side of uncoated FeCoNi after oxidation for 500 h in O_2-5%H_2O at 800 °C.

Appendix A-2: EDS analysis on bottom side of the oxidized uncoated FeCoNi.

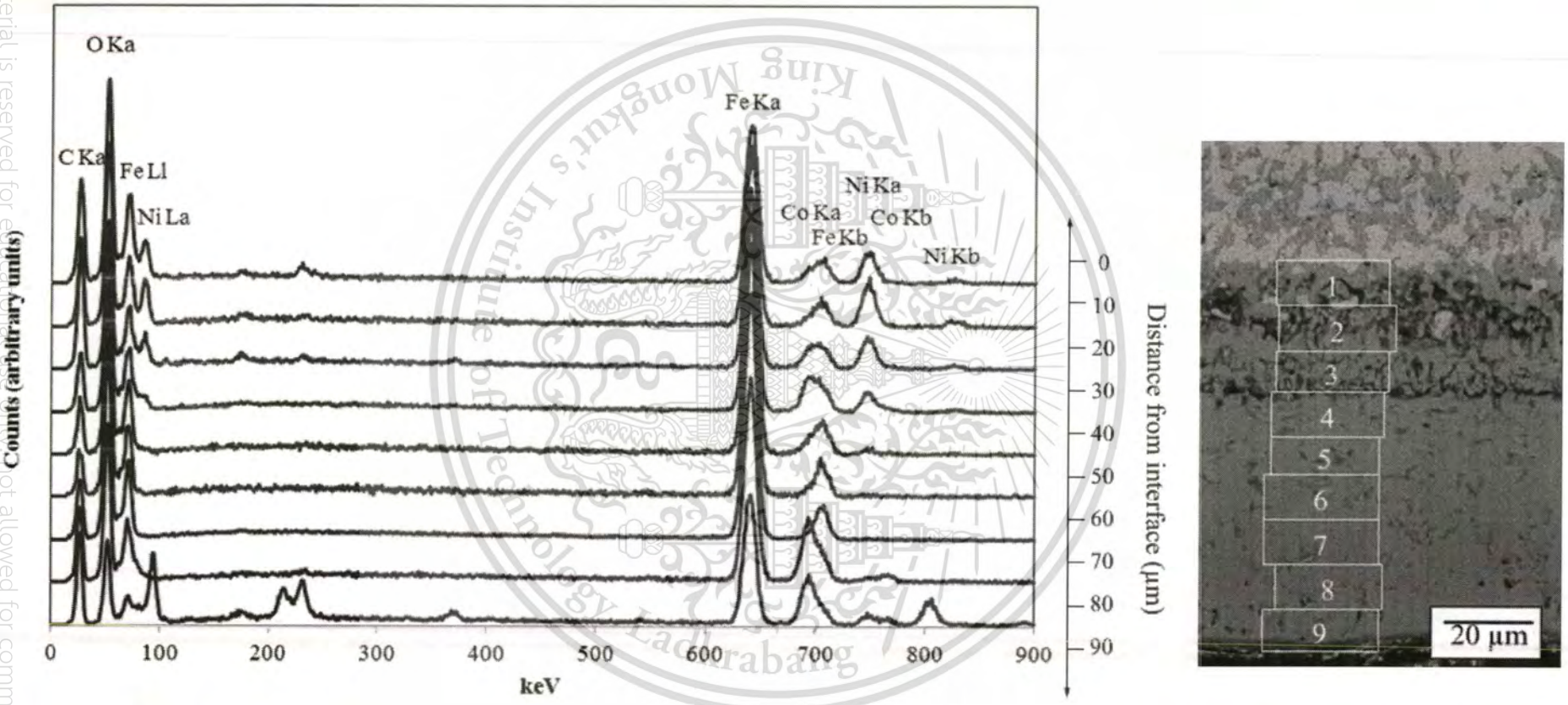

Figure A-2: EDS analysis from the outermost of scale into the metal layer on bottom side of uncoated FeCoNi after oxidation for 500 h in O_2-5%H_2O at 800 °C

Appendix A-3: EDS analysis of the oxidized LSM-SA FeCoNi.

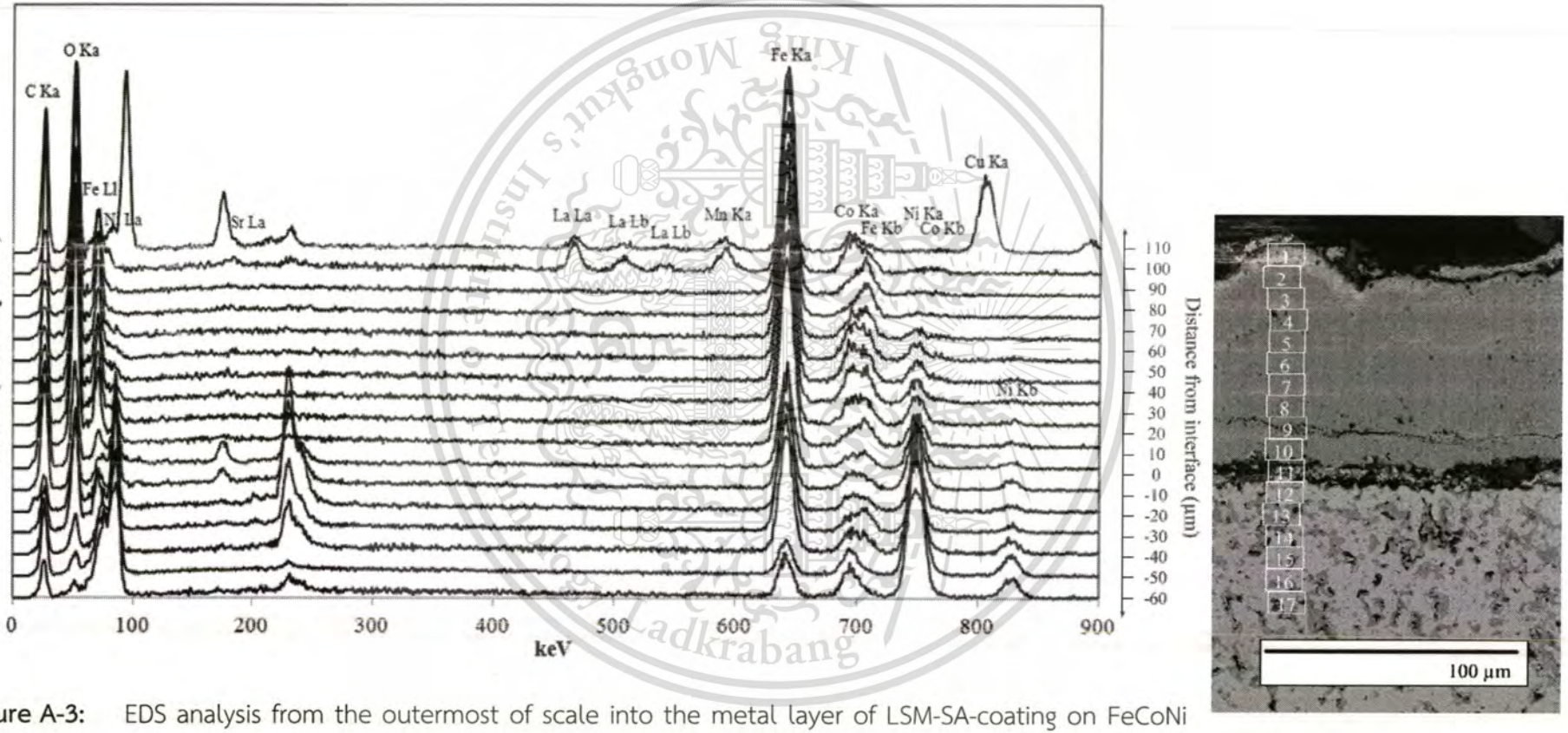

Figure A-3: EDS analysis from the outermost of scale into the metal layer of LSM-SA-coating on FeCoNi alloy after oxidation for 455 h in O_2-5%H_2O at a total flow rate of 10 L/h at 800 °C.

Appendix A-4: EDS analysis of the oxidized LNF-SA FeCoNi.

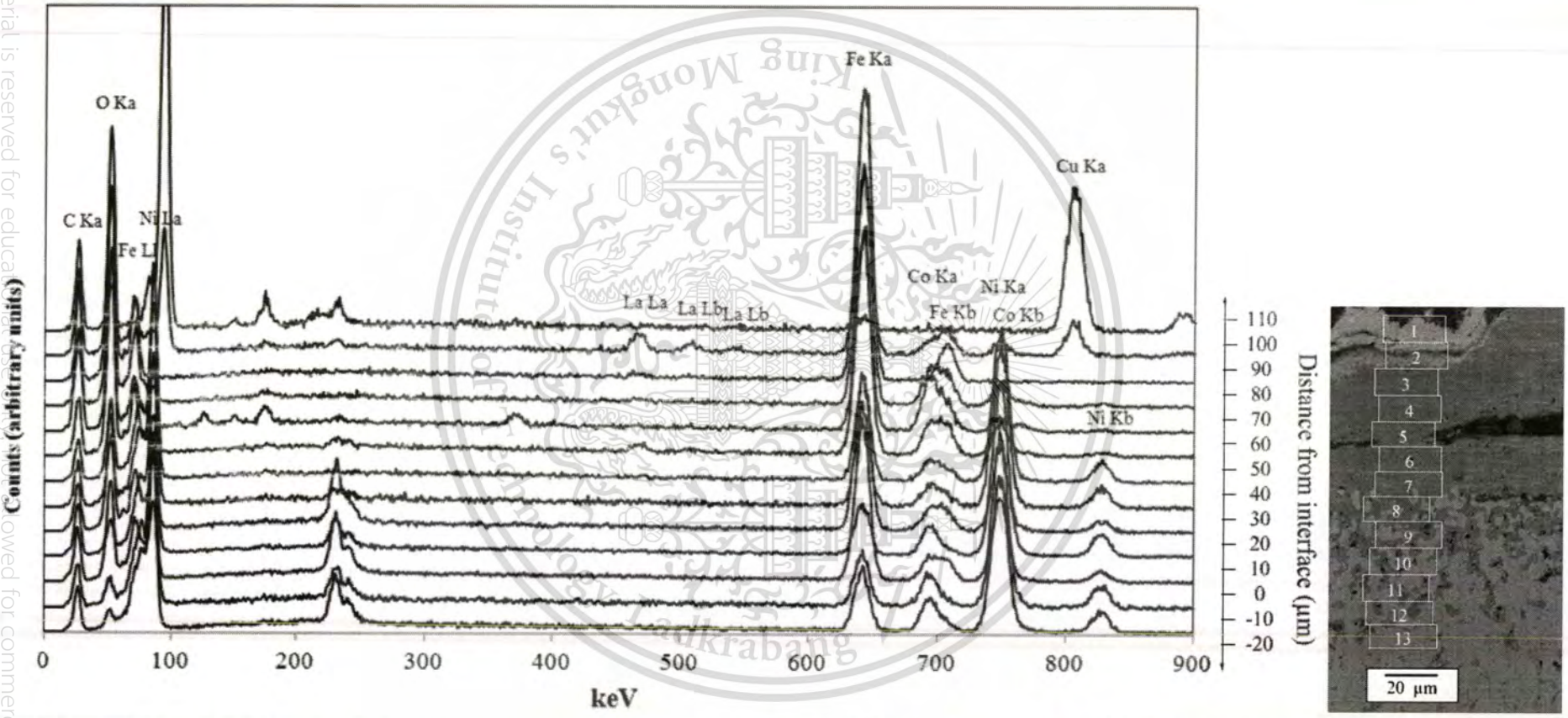

Figure A-4: EDS analysis from the outermost of scale into the metal layer of LNF-SA-coating on FeCoNi after oxidation for 455 h in O_2-5%H_2O at a total flow rate of 10 L/h at 800 °C.

Appendix A-5: EDS analysis of the oxidized LNF-PVD FeCoNi.

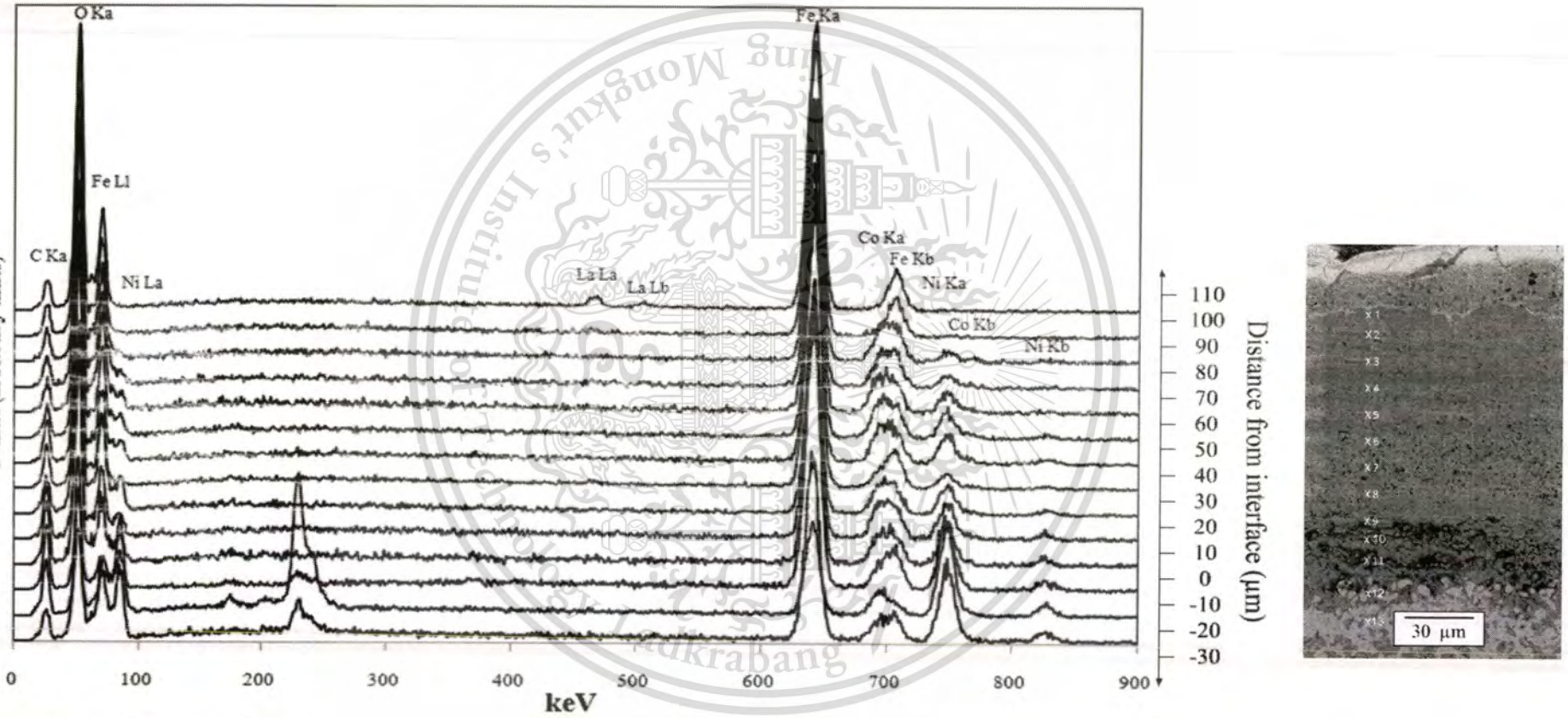

Figure A-5: EDS analysis from the outermost of scale into the metal layer of LNF-PVD-coating on FeCoNi after oxidation for 455 h in O_2-5%H_2O at a total flow rate of 10 L/h at 800 °C.

Appendix A-6: EDS analysis of the oxidized Co_3O_4-PVD FeCoNi.

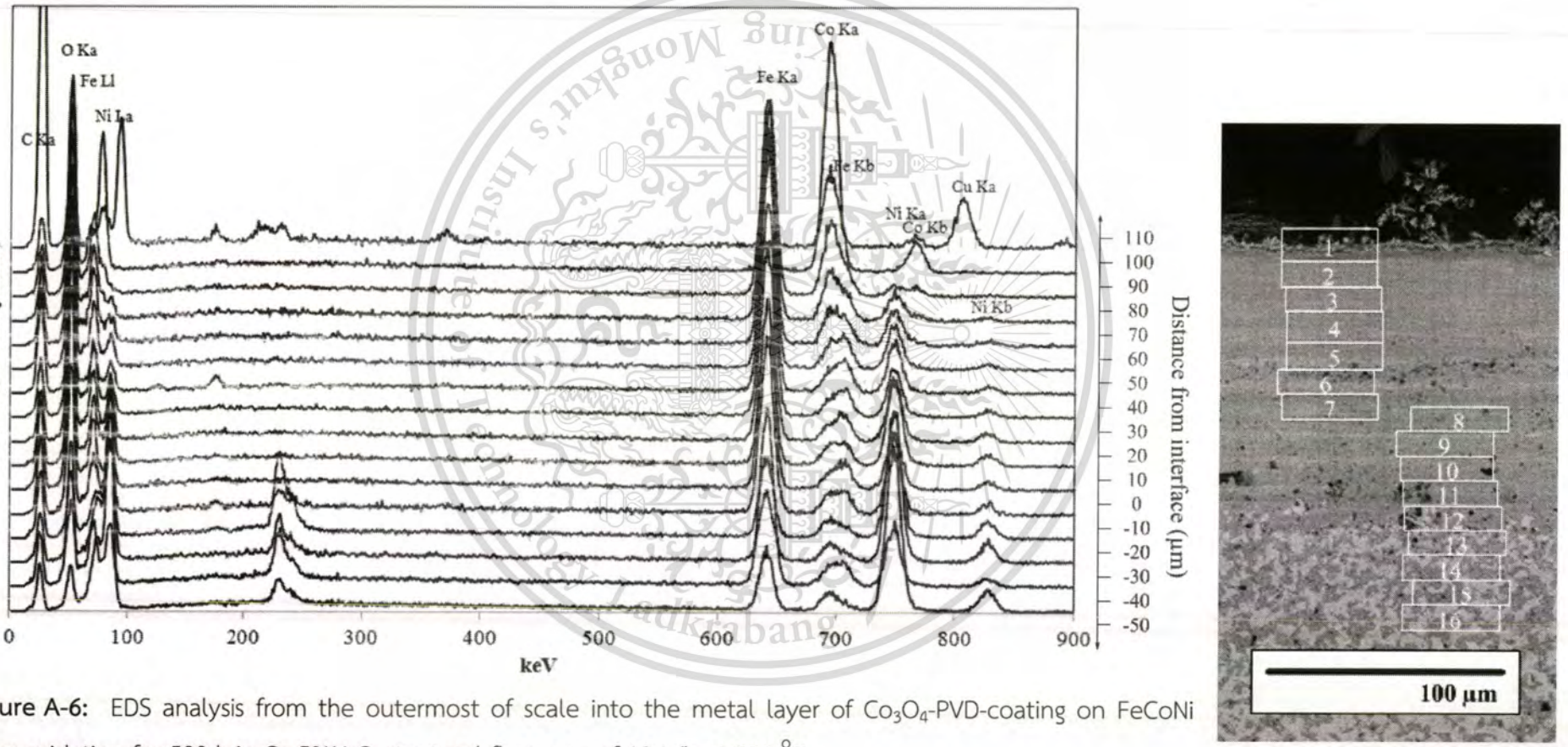

Figure A-6: EDS analysis from the outermost of scale into the metal layer of Co_3O_4-PVD-coating on FeCoNi after oxidation for 500 h in O_2-5%H_2O at a total flow rate of 10 L/h at 800 °C.

Appendices B

Vickers hardness of the coating samples

Appendix B-1: LSM-SA coating sample hardness.

Appendix B-2: LNF-SA coating sample hardness.

Appendix B-3: LNF-PVD coating sample hardness.

Appendix B-4: Co_3O_4-PVD coating sample hardness.

Appendix B-5: $MnCo_2O_4$-PVD coating sample hardness.

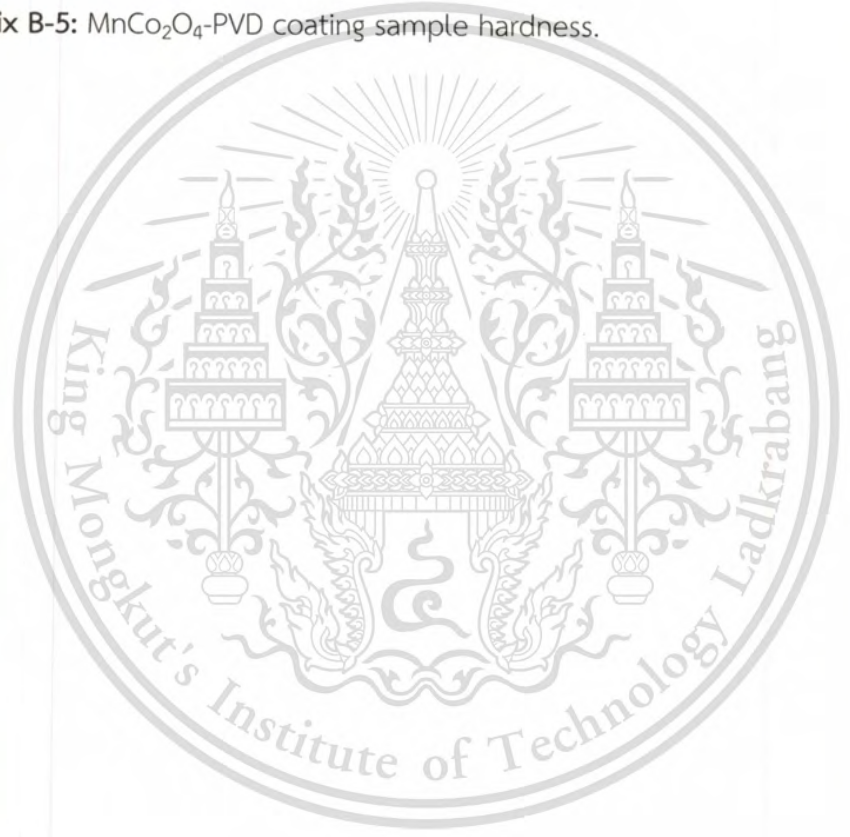

Appendix B-1

LSM-SA coating sample hardness

Table B-1 The hardness of LSM-SA coating sample.

Load (kgf)	SEM image	D1 (μm)	D2 (μm)	Avg.D (μm)	Hardness	
					HV	MPa
50	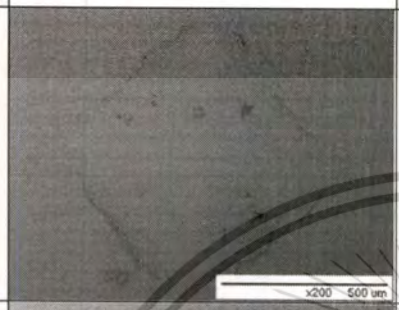	815.60	823.20	819.40	133.74	1311.55
100	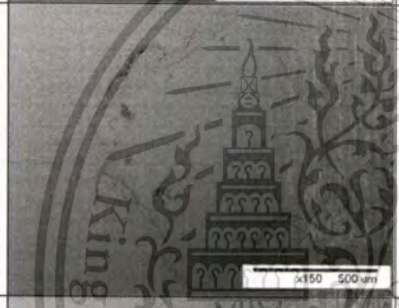	1147.63	1112.40	1130.01	140.64	1379.24
150	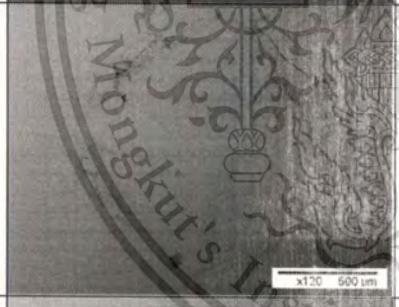	1402.56	1415.10	1408.83	135.72	1331.01
187.5	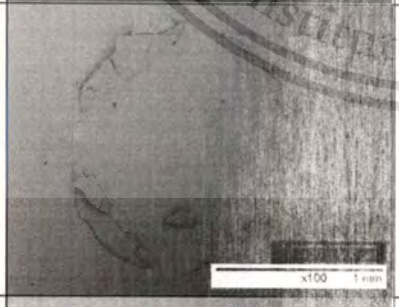	1564.13	1588.22	1576.17	135.54	1329.24
250	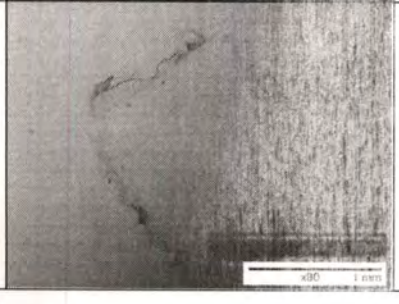	1812.69	1811.83	1812.26	136.70	1340.62

Appendix B-2

LNF-SA coating sample hardness

Table B-2 The hardness of LNF-SA coating sample.

Load (kgf)	SEM image	D1 (μm)	D2 (μm)	Avg.D (μm)	Hardness	
					HV	MPa
50	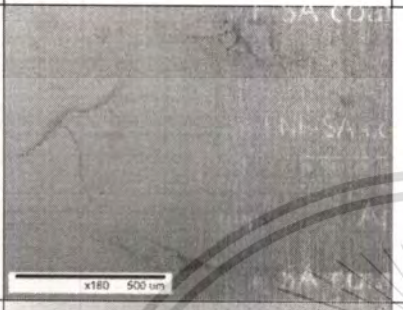	983.86	972.10	977.98	93.88	920.70
100		1321.95	1302.55	1312.25	104.29	1022.76
150	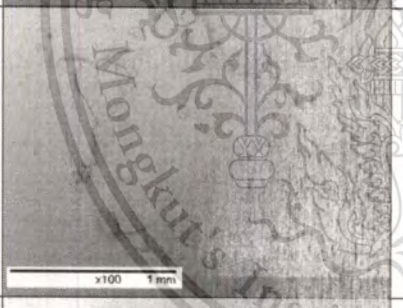	1617.42	1598.64	1608.03	104.18	1021.67
187.5	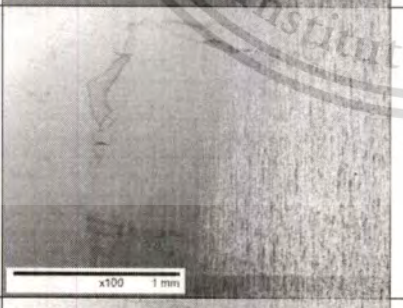	1799.16	1733.49	1766.32	107.93	1058.45
250	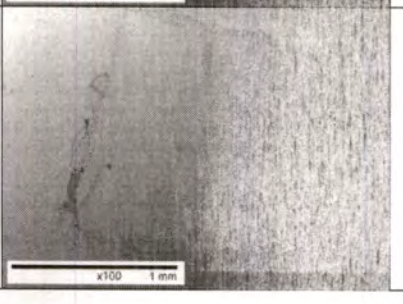	1961.28	1990.69	1975.98	114.99	1127.67

Appendix B-3

LNF-PVD coating sample hardness

Table B-3 The hardness of LNF-PVD coating sample.

Load (kgf)	SEM image	D1 (μm)	D2 (μm)	Avg.D (μm)	Hardness	
					HV	MPa
50	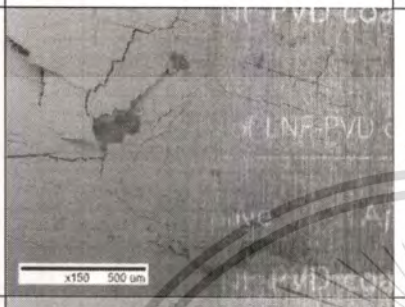	833.12	783.43	808.27	137.44	1347.91
100	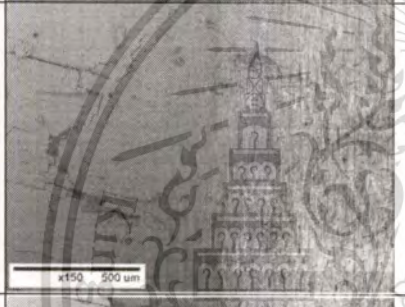	1148.01	1129.68	1138.84	138.47	1357.94
150		1397.61	1374.42	1386.01	140.23	1375.20
187.5		1531.99	1553.45	1542.72	141.48	1387.50
250	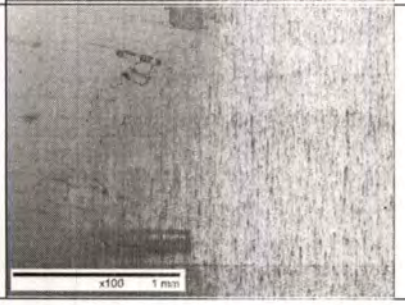	1818.45	1727.43	1772.94	142.83	1400.75

Appendix B-4

Co_3O_4-PVD coating sample hardness

Table B-4 The hardness of Co_3O_4-PVD coating sample.

Load (kgf)	SEM image	D1 (μm)	D2 (μm)	Avg.D (μm)	Hardness	
					HV	MPa
50	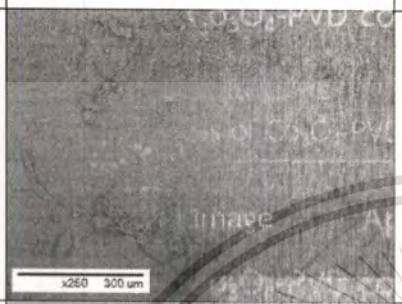	794.78	756.97	775.88	149.16	1462.83
100		1110.43	1142.25	1126.34	141.56	1388.26
150	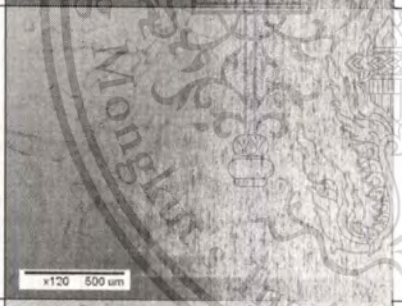	1387.57	1363.87	1375.72	142.33	1395.85
187.5	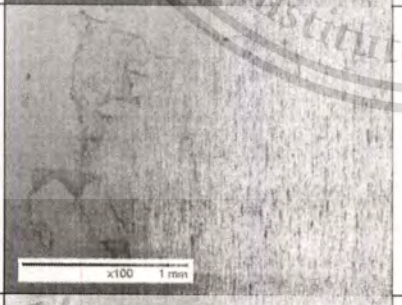	1523.96	1460.40	1492.18	151.23	1483.09
250	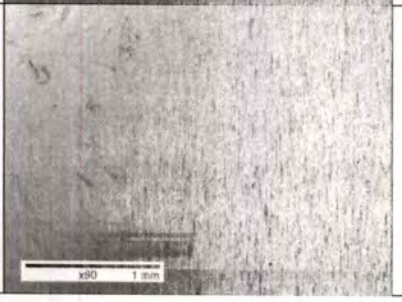	1804.62	1783.25	1793.93	139.51	1368.15

Appendix B-5

$MnCo_2O_4$-PVD coating sample hardness

Table B-5 The hardness of $MnCo_2O_4$-PVD coating sample.

Load (kgf)	SEM image	D1 (μm)	D2 (μm)	Avg.D (μm)	Hardness	
					HV	MPa
50	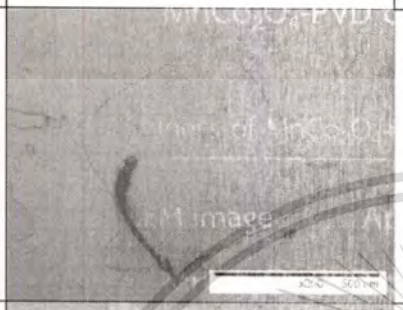	801.48	780.96	791.22	143.43	1406.64
100	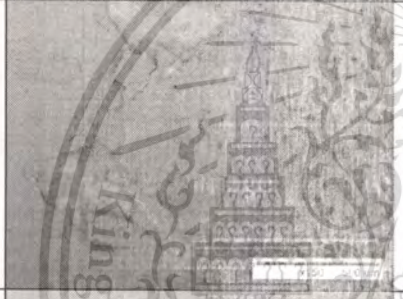	1107.71	1103.18	1105.44	146.96	1441.24
150	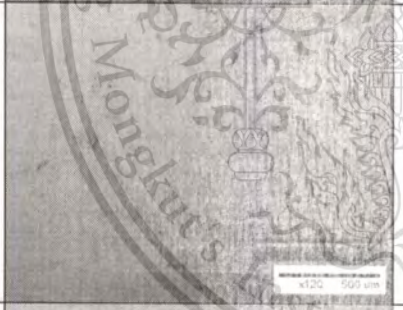	1345.47	1325.69	1335.58	151.02	1481.02
187.5	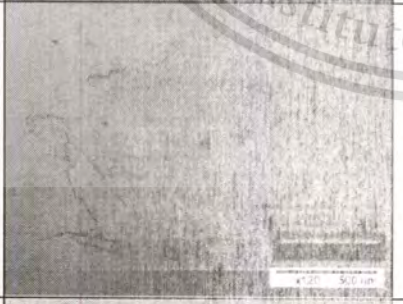	1520.17	1464.97	1492.57	151.15	1482.31
250		1772.78	1744.72	1758.75	145.15	1423.44

Appendices C

Publication

Appendix C-1: The 5th Thailand metallurgy conference proceeding.

การประเมินพฤติกรรมของโลหะ FeCoNi ที่ไม่มีการเคลือบและมีการเคลือบด้วย $La(Ni_{0.6}Fe_{0.4})O_3$ ในการประยุกต์ใช้เป็นแผ่นกั้นเซลล์ในเซลล์อิเล็กโทรไลต์ชนิดออกไซด์แข็ง

นันทิชา เยาวมาลย์*, ดร.วลัยรัตน์ จันทรอัมพร
ภาควิชาวิศวกรรมเคมี คณะวิศวกรรมศาสตร์
สถาบันเทคโนโลยีพระจอมเกล้าเจ้าคุณทหารลาดกระบัง กรุงเทพมหานคร
*(*Email address: pooy.nanticha@gmail.com)*

สมฤกษ์ จันทรอัมพร
ภาควิชาวิศวกรรมวัสดุและเทคโนโลยีการผลิต คณะวิศวกรรมศาสตร์
มหาวิทยาลัยเทคโนโลยีพระจอมเกล้าพระนครเหนือ กรุงเทพมหานคร

Valerie Parry, Yves Wouters and Alain Galerie
SIMaP Laboratory, Grenoble Institute of Technology, Grenoble, France

บทคัดย่อ

บทความนี้นำเสนอการประเมินพฤติกรรมการเกิดออกซิเดชันของโลหะ FeCoNi ที่นำมาใช้เป็นแผ่นกั้นเซลล์สำหรับเซลล์อิเล็กโทรไลต์ชนิดออกไซด์แข็งที่สภาวะอุณหภูมิสูงและมีไอน้ำร่วม โดยเปรียบเทียบในชิ้นงานที่ไม่มีการเคลือบผิวและมีการเคลือบผิวด้วย $La(Ni_{0.6}Fe_{0.4})O_3$ ด้วยวิธี slurry application และ cathodic sputtering ในสภาวะอุณหภูมิคงที่ที่ 800 °C ภายใต้บรรยากาศของแก๊สออกซิเจนที่มีไอน้ำผสมอยู่ 5% ไหลผ่านชิ้นงานที่อัตราการไหล 10 L/h พบว่ามีการเกิดออกซิเดชันขึ้นทั้งแบบภายในและภายนอก การเคลือบผิวทั้งสองวิธีสามารถลดอัตราการเกิดออกซิเดชันได้ โดยการเคลือบผิวด้วยวิธี cathodic sputtering สามารถลดอัตราการเกิดออกซิเดชันได้มากกว่าการเคลือบด้วยวิธี slurry application โดยชั้นสเกลที่เกิดขึ้นในชิ้นงานทั้ง 3 ชิ้น แบ่งได้เป็น 3 ชั้น คือชั้น $CoFe_2O_4$ ชั้น Fe_3O_4 และชั้น $(Co,Ni)_xFe_{3-x}O_4$ เรียงตามลำดับความลึกของสเกลจากด้านนอกเข้าสู่ชั้นโลหะ และสำหรับชิ้นงานเคลือบ พบว่าหลังการเกิดออกซิเดชันชั้นเคลือบสามารถเคลือบอยู่บนผิวของชิ้นงานได้โดยไม่หลุดร่อน

***คำสำคัญ**: แผ่นกั้นเซลล์, FeCoNi, slurry application, cathodic sputtering, ออกซิเดชัน*

ที่มาและความสำคัญ

การขยายตัวทางเศรษฐกิจและสังคมในปัจจุบันเป็นสาเหตุให้ความต้องการใช้พลังงานเพิ่มขึ้น ซึ่งสวนทางกับปริมาณเชื้อเพลิงที่ลดลง ดังนั้นจึงจำเป็นต้องหาพลังงานทดแทนเพื่อตอบสนองความต้องการนี้ในอนาคต ปัจจุบันมีการศึกษาและการพัฒนาเกี่ยวกับเซลล์อิเล็กโทรไลต์แบบออกไซด์แข็ง (solid oxide electrolytic cell: SOEC) อย่างกว้างขวาง เพื่อใช้เป็นอุปกรณ์ในการเปลี่ยนน้ำด้วยกระแสไฟฟ้าให้กลายเป็นไฮโดรเจนและออกซิเจน แต่เนื่องจากสภาวะการปฏิบัติงานเกิดขึ้นที่อุณหภูมิสูง (600 – 1000 °C) ปัญหาใหญ่อย่างหนึ่งที่เกิดขึ้นกับเซลล์อิเล็กโทรไลต์ชนิดนี้คือ การสึกกร่อนของแผ่นกั้นเซลล์ (interconnector) ทำให้อายุการใช้งานของเซลล์อิเล็กโทรไลต์ลดลง [1-4] ดังนั้นงานวิจัยนี้จึงมีจุดมุ่งหมายเพื่อศึกษาพฤติกรรมของโลหะเกรดใหม่ที่ถูกพัฒนาขึ้นมา เพื่อเป็นอีกหนึ่งทางเลือกในการใช้เป็นแผ่นกั้นเซลล์ในเซลล์อิเล็กโทรไลต์แบบออกไซด์แข็ง

งานวิจัยนี้ได้ศึกษาพฤติกรรมของโลหะ FeCoNi ที่ไม่มีการเคลือบผิวและมีการเคลือบผิวด้วย $La(Ni_{0.6}Fe_{0.4})O_3$ ใน 2 วิธี คือ slurry application และ cathodic sputtering ในสภาวะอุณหภูมิสูงและมีไอน้ำร่วม เพื่อการนำไปประยุกต์ใช้กับเชื้อเพลิงแบบออกไซด์แข็ง โลหะนี้มีความน่าสนใจอยู่ที่การไม่มีโครเมียมเป็นส่วนผสม จึงไม่ก่อให้เกิดปัญหาการ

ระเหยของโครเมียมดังที่เกิดขึ้นกับเหล็กกล้าไร้สนิมที่นิยมใช้เป็นแผ่นกั้นเซลล์ในปัจจุบัน [5,6]

วิธีการทดลอง

งานวิจัยนี้ศึกษาการเกิดออกซิเดชันของโลหะ FeCoNi ที่ผลิตโดยบริษัท ArcelorMittal IMPHY โดยแบ่งออกเป็นชิ้นงานที่ไม่มีการเคลือบผิว (ชิ้นงานเปลือย) และชิ้นงานที่ถูกเคลือบผิวด้วย $La(Ni_{0.6}Fe_{0.4})O_3$ (lanthanum nickelate-ferrate: LNF) ที่มีโครงสร้างผลึกแบบ perovskite ซึ่งในที่นี้จะเปรียบเทียบชิ้นงานที่เคลือบผิวด้วยวิธีที่ต่างกัน 2 วิธี คือ slurry application (SA coating) และ physical vapor deposition (PVD coating)

การทดลองแบ่งออกเป็น 2 ส่วน คือ ศึกษาจลนพลศาสตร์ของการเกิดออกซิเดชัน ด้วยเครื่อง Thermobalance (B.70-Ugine Eyraud Thermoscale) โดยนำชิ้นงานขนาด 10×10×1 mm^3 ใส่ในเครื่องแล้ววัดน้ำหนักที่เพิ่มขึ้นทุก 5 นาทีเป็นเวลา 90 ชั่วโมง และศึกษาการเกิดออกซิเดชันด้วยการเผาชิ้นงานขนาด 20×20×1 mm^3 ในเตาเผาแนวนอนเป็นเวลา 500 ชั่วโมง สำหรับชิ้นงานเปลือย และ 455 ชั่วโมง สำหรับชิ้นงานเคลือบ การทดลองทั้ง 2 ส่วนศึกษาที่อุณหภูมิคงที่ที่ 800 °C ภายใต้บรรยากาศของแก๊สออกซิเจนที่มีไอน้ำผสมอยู่ 5% ไหลผ่านชิ้นงานที่อัตราการไหล 10 L/h ทั้งนี้ ก่อนนำชิ้นงานใส่ในเตาเผาจะทำการล้างชิ้นงานเปลือยด้วยอะซิโตนและเอทานอลในเครื่องล้างอัลตร้าโซนิค ส่วนชิ้นงานเคลือบจะถูกทำความสะอาดด้วยการพ่นแก๊สไนโตรเจนผ่านพื้นผิว

หลังการทดลอง ชิ้นงานจะถูกนำไปวิเคราะห์โครงสร้างผลึกด้วยเครื่องวิเคราะห์การเลี้ยวเบนรังสีเอ็กซ์ (X-Ray diffractometer: XRD) และตรวจสอบลักษณะชิ้นงานด้วยกล้องจุลทรรศน์อิเล็กตรอนแบบส่องกราด (scanning electron microscope: SEM) ที่เชื่อมต่อกับเครื่องวิเคราะห์องค์ประกอบของธาตุ (energy dispersive spectroscopy: EDS)

ผลการทดลองและวิเคราะห์ผลการทดลอง

จลนพลศาสตร์ของการเกิดออกซิเดชัน

ผลการทดลองการศึกษาจลนพลศาสตร์ด้วยเครื่อง Thermobalance ของชิ้นงาน FeCoNi เปลือย และชิ้นงาน FeCoNi ที่มีการเคลือบผิวด้วย LNF ทั้งวิธี SA และ PVD ที่เกิดการออกซิเดชันที่อุณหภูมิคงที่ที่ 800 °C ภายใต้บรรยากาศของแก๊สออกซิเจนที่มีไอน้ำผสมอยู่ 5% ไหลผ่านชิ้นงานที่อัตราการไหล 10 L/h แสดงในรูปกราฟความสัมพันธ์ระหว่างน้ำหนักที่เพิ่มขึ้นต่อพื้นที่กับเวลา ดังรูปที่ 1

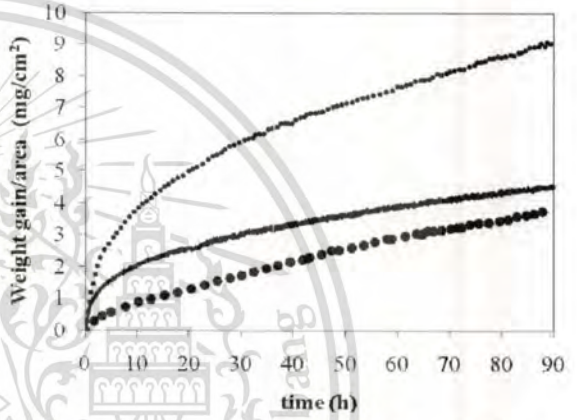

รูปที่ 1: ความสัมพันธ์ระหว่างน้ำหนักที่เพิ่มขึ้นต่อพื้นที่กับเวลา ของชิ้นงานต่างๆ ที่เกิดการออกซิเดชันที่อุณหภูมิคงที่ที่ 800 °C และมีไอน้ำ 5% ในแก๊สออกซิเจนที่อัตราการไหลรวม 10 L/h
(····· FeCoNi เปลือย
—— FeCoNi เคลือบด้วย LNF-SA
••• FeCoNi เคลือบด้วย LNF-PVD)

จากรูปจะเห็นว่าทั้ง 3 การทดลองมีแนวโน้มความสัมพันธ์ในลักษณะพาราโบลิคตามสมการ

$$w^2 = k_p \times t \qquad (1)$$

โดย w = น้ำหนักที่เพิ่มขึ้นต่อพื้นที่ (mg/cm^2),
t = เวลา (h),
k_p = ค่าคงที่พาราโบลิค ($mg/cm^2/h$)
จากนั้นคำนวณหาค่าคงที่พาราโบลิค ได้ผลลัพธ์ดังแสดงในตารางที่ 1

ตารางที่ 1: ค่าคงที่พาราโบลิค

ชิ้นงาน	ค่าคงที่พาราโบลิค ($mg^2/cm^4/h$)	R^2
Uncoated-FeCoNi	0.85	0.9933
LNF-SA-FeCoNi	0.21	0.9904
LNF-PVD-FeCoNi	0.17	0.9861

จากข้อมูลในตารางจะเห็นว่าค่าคงที่พาราโบลิคของชิ้นงานเคลือบมีค่าต่ำกว่าค่าคงที่พาราโบลิคของชิ้นงานเปลือยประมาณ 4 เท่า แสดงว่า การเคลือบผิวชิ้นงานด้วยวิธีดังกล่าวสามารถลดอัตราการเกิดออกซิเดชันของ FeCoNi ได้อย่างเห็นได้ชัด เมื่อเปรียบเทียบกับค่าคงที่พาราโบลิคของชิ้นงานที่เคลือบ LaNiFe ด้วยวิธี SA และวิธี PVD พบว่าค่าคงที่พาราโบลิคของชิ้นงานที่เคลือบด้วยวิธี PVD มีค่าต่ำกว่าค่าคงที่พาราโบลิคของชิ้นงานที่เคลือบด้วยวิธี SA เล็กน้อย แสดงว่าการเคลือบ LaNiFe บนผิวของโลหะ FeCoNi ด้วยวิธี PVD น่าจะช่วยลดอัตราการเกิดออกซิเดชันได้ดีกว่าการเคลือบด้วยวิธี SA

น้ำหนักที่เพิ่มขึ้นต่อพื้นที่ของชิ้นงานที่ได้จากการทดลองและที่ได้จากการคำนวณด้วยค่าคงที่พาราโบลิคหลังการเกิดออกซิเดชันที่อุณหภูมิคงที่ที่ 800 °C ภายใต้บรรยากาศของแก๊สออกซิเจนที่มีไอน้ำผสมอยู่ 5% ไหลผ่านชิ้นงานที่อัตราการไหล 10 L/h เป็นเวลา 500 ชั่วโมงสำหรับชิ้นงานเปลือย และ 455 ชั่วโมงสำหรับชิ้นงานเคลือบแสดงในตารางที่ 2

ตารางที่ 2: น้ำหนักที่เพิ่มขึ้นต่อหน่วยพื้นที่ของชิ้นงานหลังเกิดการออกซิเดชัน

ชิ้นงาน	น้ำหนักที่เพิ่มขึ้นต่อพื้นที่ (mg/cm^2)	
	ผลการทดลอง	การคำนวณ
Uncoated-FeCoNi (500 h)	17.91	20.62
LNF-SA-FeCoNi (455 h)	13.94	9.77
LNF-PVD-FeCoNi (455 h)	13.81	8.79

จากตารางที่ 2 พบว่า สำหรับชิ้นงานเปลือยน้ำหนักที่เพิ่มขึ้นต่อพื้นที่ที่ได้จากการทดลองมีค่าต่ำกว่าค่าที่ได้จากการคำนวณประมาณ 13% แต่สำหรับชิ้นงานเคลือบน้ำหนักที่เพิ่มขึ้นต่อพื้นที่ที่ได้จากการทดลองมีค่ามากกว่าค่าที่ได้จากการคำนวณประมาณ 50%

สัณฐานวิทยา

3.2.1 โลหะ FeCoNi เปลือย

หลังการทดลองการเกิดออกซิเดชันของโลหะ FeCoNi เปลือยที่อุณหภูมิคงที่ที่ 800 °C และมีไอน้ำ 5% ในแก๊สออกซิเจนที่อัตราการไหล 10 L/h ในเตาเผาแนวนอน 500 ชั่วโมง ชิ้นงานถูกนำไปวิเคราะห์ด้วย XRD, SEM/EDS รูปที่ 2 แสดงลักษณะพื้นผิวของชิ้นงานเปลือยหลังการทดลอง

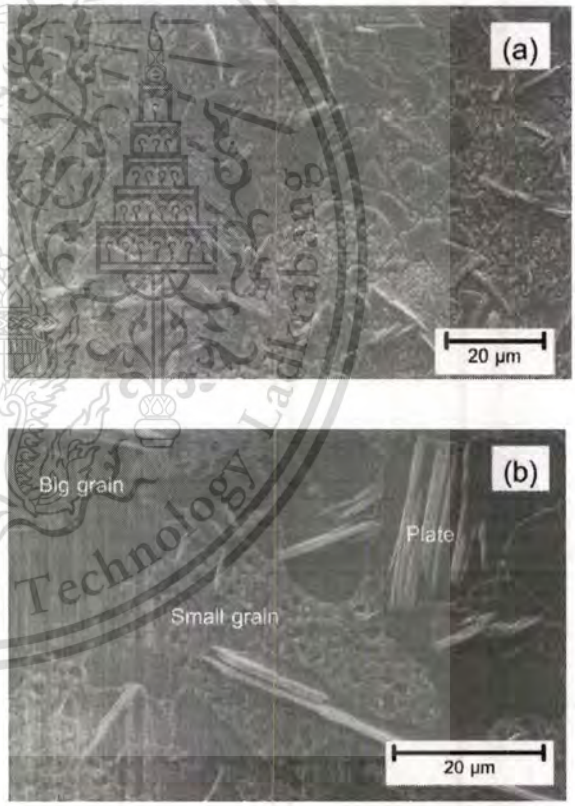

รูปที่ 2: ภาพพื้นผิวของชิ้นงาน FeCoNi เปลือย หลังการเกิดออกซิเดชันที่อุณหภูมิคงที่ที่ 800 °C และมีไอน้ำ 5% ในแก๊สออกซิเจนที่อัตราการไหลรวม 10 L/h เป็นเวลา 500 ชั่วโมง

จากรูปจะเห็นว่ามีลักษณะปรากฏ 3 ลักษณะ คือ บริเวณเกรนใหญ่ (big grain), บริเวณเกรนเล็ก (small grain) และบริเวณที่มีลักษณะคล้ายแผ่น (plate)

ผลการตรวจวิเคราะห์ด้วย XRD ของชิ้นงาน FeCoNi เปลือยก่อนการเกิดออกซิเดชัน เปรียบเทียบกับหลังการออกซิเดชัน 500 ชั่วโมง พบว่า ก่อนการทดลองมีเฉพาะ 2 พีคของ cubic เฟสของ FeCoNi แต่หลังจากการเกิดออกซิเดชัน พบพีคอื่นๆ อีก 5 พีค ปรากฏขึ้น ซึ่งพีคที่พบเป็นไปได้ว่าจะเป็น cubic เฟสของ $CoFe_2O_4$ ดังรูปที่ 3

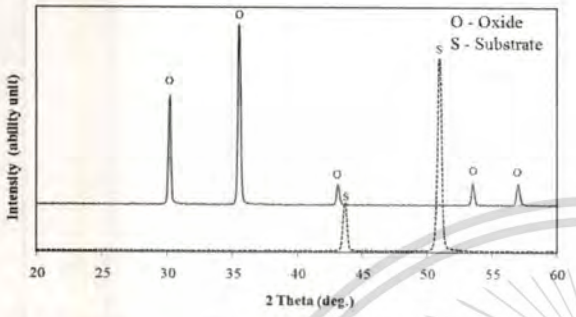

รูปที่ 3: ผลการวิเคราะห์ XRD ของโลหะ FeCoNi เปลือย
(•••• ก่อนการเกิดออกซิเดชัน,
—— หลังการเกิดออกซิเดชันที่อุณหภูมิคงที่ที่ 800 °C และมีไอน้ำ 5% ในแก๊สออกซิเจนที่อัตราการไหลรวม 10 L/h เป็นเวลา 500 ชั่วโมง)

เมื่อพิจารณาผล XRD กับภาพพื้นผิวพบความเป็นไปได้ที่ทั้ง 3 ลักษณะที่ปรากฏในรูปที่ 2 เป็น Cubic เฟสของ $CoFe_2O_4$ ทั้งหมด

ภาพตัดขวางของชิ้นงานเปลือยแสดงดังรูปที่ 4 จากรูปจะเห็นว่า สเกลออกไซด์มีความหนาเฉลี่ย 240 μm ทั้งยังพบรูพรุนกระจายอยู่ตามบริเวณรอยต่อและในชั้นออกไซด์ใกล้กับรอยต่อ ในชั้นออกไซด์พบความเข้มของสีที่แตกต่างกัน 3 ชั้น ซึ่งบ่งบอกว่ามีการกระจายตัวของธาตุแตกต่างกันไปในแต่ละชั้น ออกซิเดชันภายในเกิดขึ้นในลักษณะของตะกอนออกไซด์กระจายอยู่ทั่วทั้งชั้นโลหะดังที่สังเกตเห็นจากจุดสีดำที่กระจายตัวอยู่ในชั้นโลหะสีขาวของ FeCoNi ผลการวิเคราะห์องค์ประกอบของธาตุโดยทำการวิเคราะห์ EDS ที่ระดับความลึกลงไปจากพื้นผิวของชั้นออกไซด์ไปยังชั้นโลหะที่ระดับต่างๆ โดยทำการวัดลึกลงไปเรื่อยๆ ทุก 10 μm พบว่าในชั้นสเกลมีการกระจายของธาตุองค์ประกอบแบ่งได้เป็น 3 ชั้นตามแถบสีที่ปรากฏในรูปที่ 4 โดยชั้นนอกของสเกลพบออกไซด์ของเหล็กและโคบอลต์ ในชั้นกลางพบออกไซด์ของเหล็ก และชั้นในเป็นออกไซด์ของเหล็ก โคบอลต์และนิกเกิล ทั้งยังพบว่าที่ชั้นในของสเกลมีโคบอลต์ปริมาณสูงบริเวณใกล้กับชั้นกลาง โดยโคบอลต์จะมีปริมาณลดลงเรื่อยๆ เมื่อเข้าใกล้รอยต่อระหว่างโลหะกับสเกล ซึ่งปริมาณโคบอลต์ที่พบมีแนวโน้มสวนทางกับนิกเกิล

นอกจากนี้การวิเคราะห์ EDS ยังพบอีกว่าจุดสีดำที่กระจายตัวอยู่ในชั้นโลหะสีขาวในรูปที่ 4 นั้นเป็นตะกอนออกไซด์ของเหล็ก

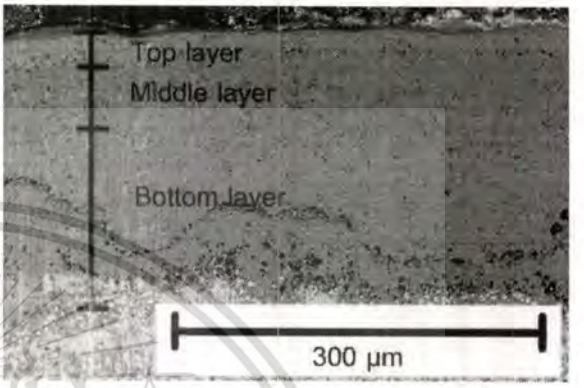

รูปที่ 4: ภาพตัดขวางของชิ้นงาน FeCoNi เปลือย หลังเกิดการออกซิเดชันที่อุณหภูมิคงที่ที่ 800 °C และมีไอน้ำ 5% ในแก๊สออกซิเจนที่อัตราการไหลรวม 10 L/h เป็นเวลา 500 ชั่วโมง

3.2.2 โลหะ FeCoNi เคลือบ LNF ด้วยวิธี SA

ภาพพื้นผิวของชิ้นงาน FeCoNi เคลือบ LNF ด้วยวิธี SA หลังเกิดออกซิเดชันที่อุณหภูมิคงที่ที่ 800 °C และมีไอน้ำ 5% ในแก๊สออกซิเจนที่อัตราการไหลรวม 10 L/h ในเตาเผาแนวนอน 455 ชั่วโมง แสดงในรูปที่ 5

จากรูปที่ 5b ปรากฏรอยแตกของชั้นเคลือบกระจายอยู่ทั่วทั้งพื้นผิว ผลจากการวิเคราะห์ EDS พบ La, Ni, Fe และ O ปริมาณมากที่บริเวณ A จึงเป็นไปได้ว่าบริเวณนี้คือผิวเคลือบ ส่วนที่บริเวณ B พบ Fe, Co และ O ปริมาณมาก จึงอาจเป็นไปได้ว่าบริเวณนี้คือออกไซด์ของเหล็กและโคบอลต์ที่ถูกออกซิไดซ์จากชั้นโลหะ รอยแตกที่เกิดขึ้นนี้ เป็นไปได้ว่าเกิดจากการที่ออกซิเจนสามารถแพร่ผ่านชั้นเคลือบไปยังโลหะทำให้เกิดการออกซิไดซ์เป็นออกไซด์ดันชั้นเคลือบให้แตกออก

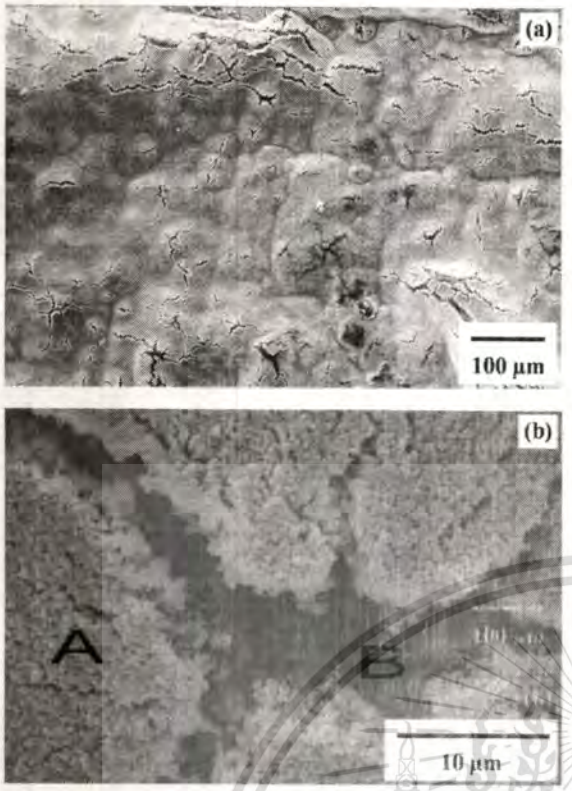

รูปที่ 5: ภาพพื้นผิวของชิ้นงาน FeCoNi เคลือบ LNF ด้วยวิธี SA หลังการเกิดออกซิเดชันที่อุณหภูมิคงที่ที่ 800 °C และมีไอน้ำ 5% ในแก๊สออกซิเจนที่อัตราการไหลรวม 10 L/h เป็นเวลา 455 ชั่วโมง

ผลการตรวจวิเคราะห์ด้วย XRD ของชิ้นงาน FeCoNi ที่เคลือบ LNF ด้วยวิธี SA ก่อนการเกิดออกซิเดชัน เปรียบเทียบกับหลังการออกซิเดชัน 455 ชั่วโมง ที่อุณหภูมิคงที่ที่ 800 °C และมีไอน้ำ 5% ในแก๊สออกซิเจนที่อัตราการไหลรวม 10 L/h แสดงในรูปที่ 6

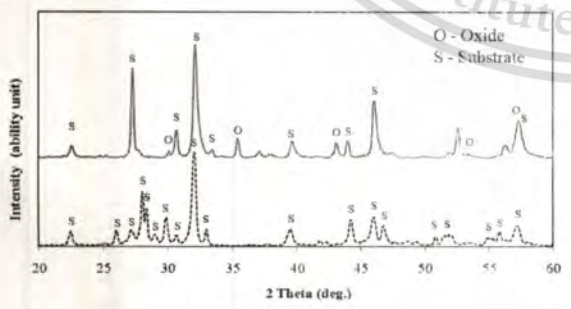

รูปที่ 6: ผลการวิเคราะห์ XRD ของโลหะ FeCoNi เคลือบ LNF ด้วยวิธี SA
(···· ก่อนการเกิดออกซิเดชัน
— หลังการเกิดออกซิเดชันที่อุณหภูมิคงที่ที่ 800 °C และมีไอน้ำ 5% ในแก๊สออกซิเจนที่อัตราการไหลรวม 10 L/h เป็นเวลา 455 ชั่วโมง)

จากรูปพบว่า พีคที่พบหลังการเกิดออกซิเดชันเป็นไปได้ว่าเป็นพีคของ 2 เฟส คือ เฟสที่พบก่อนการเกิดออกซิเดชันซึ่งเป็นของชั้นเคลือบ (บริเวณ A ในรูปที่ 5b) และเป็นไปได้ว่าอีกเฟสที่พบคือเฟส Cubic ของ $CoFe_2O_4$ ที่บริเวณรอยแตก (บริเวณ B ในรูปที่ 5b)

รูปที่ 7 แสดงภาพตัดขวางของชิ้นงานหลังเกิดออกซิเดชัน ซึ่งพบว่า สเกลมีความหนาเฉลี่ย 68 µm ทั้งยังพบรูพรุนกระจายอยู่ตามบริเวณรอยต่อและในชั้นออกไซด์ใกล้กับรอยต่อ และพบการเกิดออกซิเดชันภายในที่เกิดขึ้นในลักษณะของตะกอนออกไซด์ (จุดสีเทา) กระจายอยู่ชั้นโลหะใกล้กับรอยต่อระหว่างสเกลกับโลหะ

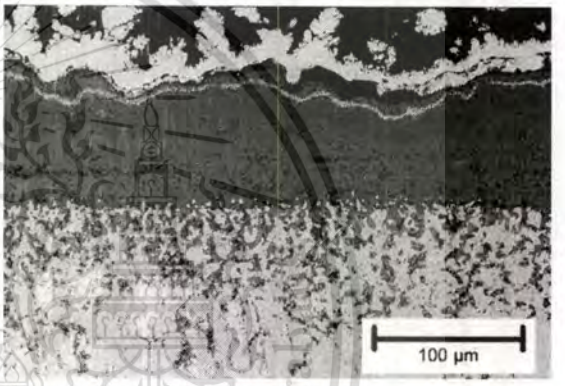

รูปที่ 7: ภาพตัดขวางของชิ้นงาน FeCoNi เคลือบ LNF ด้วยวิธี SA หลังการเกิดออกซิเดชันที่อุณหภูมิคงที่ที่ 800 °C และมีไอน้ำ 5% ในแก๊สออกซิเจนที่อัตราการไหลรวม 10 L/h เป็นเวลา 455 ชั่วโมง

ผลการวิเคราะห์องค์ประกอบของธาตุโดยทำการวิเคราะห์ EDS ที่ระดับความลึกลงไปจากพื้นผิวของชั้นออกไซด์ไปยังชั้นโลหะที่ระดับต่างๆ โดยทำการวัดลึกลงไปเรื่อยๆ ทุก 10 µm พบการกระจายของธาตุองค์ประกอบแบ่งได้เป็น 3 ชั้นเช่นเดียวกับที่พบในชิ้นงานเปลือย คือ ชั้นออกไซด์ของเหล็กและโคบอลต์ ชั้นออกไซด์ของเหล็ก และชั้นออกไซด์ของเหล็กโคบอลต์และนิกเกิล เมื่อพิจารณาธาตุที่เป็นส่วนผสมของผิวเคลือบ พบว่า La, Ni และ Fe มีปริมาณมากที่ชั้นนอกสุดของสเกล แสดงว่าชั้นเคลือบยังคงอยู่ที่ผิวนอก และยังพบโคบอลต์และออกซิเจนที่บริเวณความลึกเดียวกันด้วย

ผลการวิเคราะห์ EDS ภายในชั้นโลหะพบว่าการเกิดออกซิเดชันภายในที่เกิดในลักษณะของตะกอนเล็กๆ สีเทาในรูปที่ 7 คือออกไซด์ของเหล็กนั่นเอง

3.2.3 โลหะ *FeCoNi* เคลือบ *LNF* ด้วยวิธี *PVD*

หลังการทดลองการเกิดออกซิเดชันของโลหะ FeCoNi เคลือบ LNF ด้วยวิธี PVD ที่อุณหภูมิคงที่ที่ 800 °C และมีไอน้ำ 5% ในแก๊สออกซิเจนที่อัตราการไหลรวม 10 L/h ในเตาเผาแนวนอน 455 ชั่วโมง ชิ้นงานจะถูกนำไปวิเคราะห์ด้วย XRD, SEM/EDS รูปที่ 8 แสดงภาพพื้นผิวของชิ้นงานหลังเกิดออกซิเดชัน

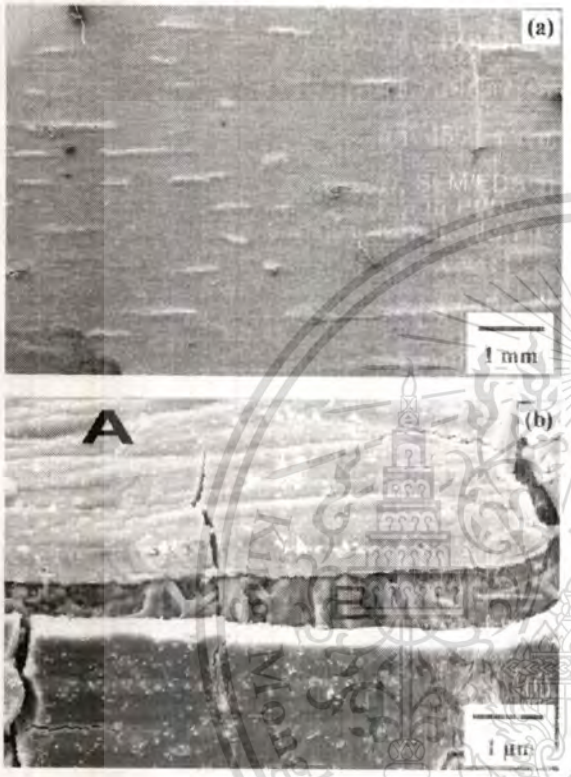

รูปที่ 8: ภาพพื้นผิวของชิ้นงาน FeCoNi เคลือบ LNF ด้วยวิธี PVD หลังการเกิดออกซิเดชันที่อุณหภูมิคงที่ที่ 800 °C และมีไอน้ำ 5% ในแก๊สออกซิเจนที่อัตราการไหลรวม 10 L/h เป็นเวลา 455 ชั่วโมง

จากรูปปรากฏรอยแตกขนาดเล็กมากกระจายอยู่บนพื้นผิวของชิ้นงาน ผลจากการวิเคราะห์ EDS พบ La, Ni, Fe และ O ปริมาณมากที่บริเวณ A ซึ่งเป็นไปได้ว่าบริเวณนี้คือผิวเคลือบ ส่วนที่บริเวณ B พบ Fe, Co และ O ปริมาณมาก จึงเป็นไปได้ว่าบริเวณนี้คือออกไซด์ของเหล็กและโคบอลต์ เช่นเดียวกับที่พบในชิ้นงานเคลือบด้วยวิธี SA

การตรวจวิเคราะห์ด้วย XRD ของชิ้นงาน FeCoNi ที่เคลือบ LNF ด้วยวิธี PVD ก่อนการเกิดออกซิเดชันเปรียบเทียบกับหลังการออกซิเดชัน 455 ชั่วโมง ที่อุณหภูมิคงที่ที่ 800 °C และมีไอน้ำ 5% ในแก๊สออกซิเจนที่อัตราการไหลรวม 10 L/h แสดงดังรูปที่ 9 จากรูปพบว่า พีคที่พบหลังการเกิดออกซิเดชันเกิดขึ้นที่ตำแหน่งเดียวกับพีคที่พบก่อนการเกิดออกซิเดชัน ซึ่งเป็นพีคของชั้นเคลือบ แสดงว่า หลังการเกิดออกซิเดชันชั้นเคลือบยังคงเคลือบอยู่บนผิวโลหะได้ดี

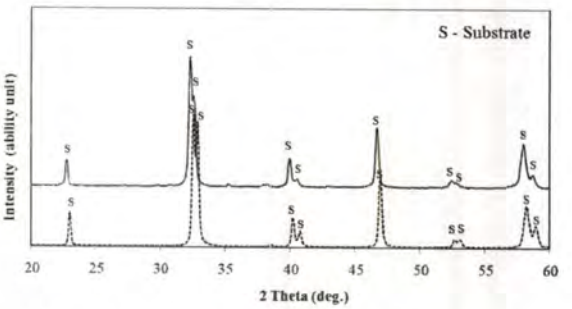

รูปที่ 9: ผลการวิเคราะห์ XRD ของโลหะ FeCoNi เคลือบ LNF ด้วยวิธี PVD
(···· ก่อนการเกิดออกซิเดชัน
— หลังการเกิดออกซิเดชันที่อุณหภูมิคงที่ที่ 800 °C และมีไอน้ำ 5% ในแก๊สออกซิเจนที่อัตราการไหลรวม 10 L/h เป็นเวลา 455 ชั่วโมง)

รูปที่ 10 แสดงภาพตัดขวางของชิ้นงานหลังเกิดออกซิเดชัน ซึ่งแสดงให้เห็นสเกลที่มีความหนาเฉลี่ย 163 μm ทั้งยังพบรูพรุนกระจายอยู่ตามบริเวณรอยต่อและในชั้นออกไซด์ใกล้กับรอยต่อ และพบการออกซิเดชันภายในเกิดขึ้นในลักษณะของตะกอนออกไซด์กระจายอยู่ทั่วไปในชั้นโลหะ

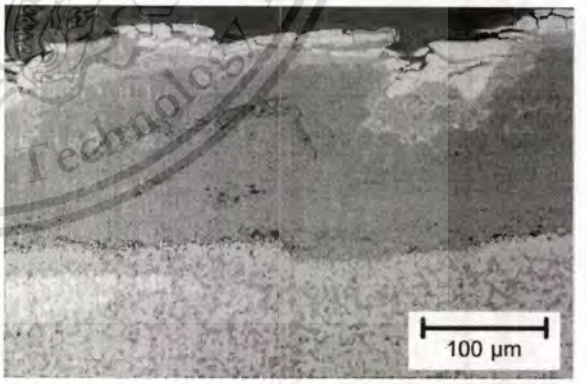

รูปที่ 10: ภาพตัดขวางของชิ้นงาน FeCoNi เคลือบ LNF ด้วยวิธี PVD หลังการเกิดออกซิเดชันที่อุณหภูมิคงที่ที่ 800 °C และมีไอน้ำ 5% ในแก๊สออกซิเจนที่อัตราการไหลรวม 10 L/h เป็นเวลา 455 ชั่วโมง

ผลการวิเคราะห์ EDS ในชั้นสเกล พบการกระจายของธาตุองค์ประกอบแบ่งได้เป็น 4 ชั้น โดยที่ชั้นนอกสุดพบ La Ni และ Fe ในปริมาณมาก เป็นไปได้ว่าชั้นนี้เป็นชั้นผิวเคลือบ แสดงว่า ชั้นเคลือบยังคงเคลือบอยู่

บนผิวนอก ส่วน 3 ชั้นถัดเข้ามาพบการกระจายตัวของธาตุในลักษณะเดียวกับที่พบในชิ้นงาน FeCoNi เปลือยและชิ้นงานเคลือบด้วยวิธี SA คือ ชั้นออกไซด์ของเหล็กและโคบอลต์ ชั้นออกไซด์ของเหล็ก และชั้นออกไซด์ของเหล็ก โคบอลต์และนิกเกิล อย่างไรก็ตามในชั้นออกไซด์ของเหล็กและโคบอลต์พบธาตุองค์ประกอบของผิวเคลือบปะปนอยู่ทั่วทั้งชั้น แสดงว่าการเคลือบด้วยวิธีนี้ยังไม่สามารถป้องกันการแพร่ของไอออนของโลหะได้

จากการวิเคราะห์ EDS ภายในชั้นโลหะ ยืนยันให้ทราบอีกครั้งว่า เกิดตะกอนขนาดเล็กของออกไซด์ของเหล็กกระจายอยู่ทั่วชั้นโลหะ

สรุปผล

การทดลองการเกิดออกซิเดชันของ FeCoNi ที่อุณหภูมิคงที่ที่ 800 °C และมีไอน้ำ 5% ในแก๊สออกซิเจนที่อัตราการไหลรวม 10 L/h สามารถอธิบายได้ว่า

1. การเคลือบผิว FeCoNi ด้วย LNF โดยวิธี SA และ PVD สามารถลดอัตราการเกิดออกซิเดชันได้ โดยการเคลือบผิวด้วยวิธี PVD สามารถลดอัตราการเกิดออกซิเดชันได้มากกว่าการเคลือบผิวด้วยวิธี SA เล็กน้อย

2. เมื่อเปรียบเทียบระหว่างชิ้นงาน FeCoNi ที่มีการเคลือบผิวด้วย LNF ด้วยวิธี SA และ PVD หลังเกิดออกซิเดชัน พบว่า การเคลือบชิ้นงานด้วยวิธี SA จะทำให้เกิดรอยแตกทั่วทั้งผิวชิ้นงาน แต่จะไม่พบการแตกในชิ้นงานที่มีการเคลือบด้วยวิธี PVD และเมื่อพิจารณาด้านการเกิดออกซิเดชันภายใน พบว่า การเคลือบด้วยวิธี SA มีความสามารถในการป้องกันการเกิดออกซิเดชันภายในได้ดีกว่าการเคลือบด้วยวิธี PVD

3. สเกลที่เกิดขึ้นแบ่งได้เป็น 3 ชั้นโดยชั้นบนสุดของสเกลพบออกไซด์ของ Fe-Co ที่คาดว่าเป็น Cubic ของ $CoFe_2O_4$ และพบออกไซด์ของ Fe ในชั้นถัดมาซึ่งคาดว่าเป็นเฟสของ Fe_3O_4 และในชั้นลึกสุดของสเกลพบออกไซด์ของ Co-Ni-Fe ซึ่งคาดว่าเป็นเฟสของ $(Co,Ni)_xFe_{3-x}O_4$

4. สำหรับชิ้นงานเคลือบพบว่า ชั้นเคลือบยังคงเคลือบอยู่บนพื้นผิว โดยที่ชั้นเคลือบของชิ้นงานเคลือบด้วยวิธี SA มีชั้น $CoFe_2O_4$ ปะปนอยู่ แต่สำหรับชิ้นงานเคลือบด้วยวิธี PVD ชั้นเคลือบยังคงเคลือบอยู่เหนือชั้น $CoFe_2O_4$

โดยภาพรวมสรุปได้ว่า ในการเคลือบผิวด้วย LNF ทั้งวิธี SA และ PVD สามารถลดอัตราการเกิดออกซิเดชันของ FeCoNi ลงได้ แต่ไม่สามารถป้องกันการเกิดออกซิเดชันได้ ดังนั้น โลหะ FeCoNi ทั้งที่ไม่มีการเคลือบผิวและที่มีการเคลือบผิวด้วย $La(Ni_{0.6}Fe_{0.4})O_3$ ทั้งวิธี slurry application และ physical vapor deposition จึงไม่เหมาะสมที่จะประยุกต์ใช้เป็นแผ่นกั้นเซลล์ในเซลล์อิเล็กโทรไลต์ชนิดออกไซด์แข็ง

กิตติกรรมประกาศ

ขอขอบคุณ ArcelorMittal IMPHY ในการอนุเคราะห์ชิ้นงาน ขอบคุณ SIMaP Laboratory, Grenoble Institute of Technology, Grenoble, ประเทศฝรั่งเศสที่ให้ความอนุเคราะห์เครื่องมือและสถานที่ทำวิจัย

เอกสารอ้างอิง

[1] Singhal, Subhash C. and Kendall, Kevin, 2003, *High Temperature Solid Oxide Fuel Cells: Fundamentals, Design and Applications*, Elsevier, Great Britain.

[2] David Young, 2008, *High Temperature Oxidation and Corrosion of Metals*, Elsevier, Great Britain.

[3] Grant L. Hawkes1, James E. O'Brien, Carl M. Stoots, J. Stephen Herring, Mehrdad Shahnam, 2005, *CFD Model Of A Planar Solid Oxide Electrolysis Cell For Hydrogen Production From Nuclear Energy*, The 11th International Topical Meeting on Nuclear Reactor Thermal-

Hydraulics (NURETH-11) Popes' Palace Conference Center, Avignon, France, October 2-6.

[4] Kongfa Chen, San Ping Jiang, 2011, *Failure mechanism of (La,Sr)MnO3 oxygen electrodes of solid oxide electrolysis cells*, international journal of hydrogen energy 36 10541-10549.

[5] S. Chandra-Ambhorn, Y. Wouters, L. Antoni, F. Toscan, A. Galerie, 2007, *Adhesion of oxide scales grown on ferritic stainless steels in solid oxide fuel cells temperature and atmosphere conditions*, J. Power Sources 171 688–695.

[6] G. Bamba, Y. Wouters, A. Galerie, G. Borchardt, S. Shimada, O. Heintzd and S. Chevalier, 2007, *Inverse growth transport in thermal chromia scales on Fe–15Cr steels in oxygen and in water vapour and its effect on scale adhesion*, scriptamat, 57 671–674.

Author Biography

Name:	Miss Nanticha Yaowaman
Date of birth:	April 17, 1988
Place of birth:	Ubonratchatani, Thailand
Address:	9/101, Village No.23, Khamyai, Mueng, Ubonratchatani, Thailand
Email:	pooy.nanticha@gmail.com

Educations:

2010-2012: M.Eng. (Chemical Engineering)
School of Chemical Engineering, Faculty of Engineering,
King Mongkut's Institute of Technology Ladkrabang (KMIT'L),
Bangkok, Thailand.

2006 – 2010: B.Eng. (Chemical Engineering)
School of Chemical Engineering, Faculty of Engineering,
King Mongkut's Institute of Technology Ladkrabang (KMIT'L),
Bangkok, Thailand.

Publication

2012: Nanticha Yaowaman, Walairat Chandra-ambhorn, Somrerk Chandra-ambhorn, "Evaluation of $La(Ni_{0.6}Fe_{0.4})O_3$ coating on FeCoNi for applying as an interconnector in solid oxide electrolytic cell", **The 5th Thailand metallurgy conference proceeding**, Bangkok, Thailand (published in Thai), 19-20 January 2012, p.52.

Honor

2012: Best paper award in surface engineering section from The 5th Thailand metallurgy conference.